



National Library
of Canada

Bibliothèque nationale
du Canada

Canadian Theses Service Service des thèses canadiennes

Ottawa, Canada
K1A 0N4

NOTICE

The quality of this microform is heavily dependent upon the quality of the original thesis submitted for microfilming. Every effort has been made to ensure the highest quality of reproduction possible.

If pages are missing, contact the university which granted the degree.

Some pages may have indistinct print especially if the original pages were typed with a poor typewriter ribbon or if the university sent us an inferior photocopy.

Reproduction in full or in part of this microform is governed by the Canadian Copyright Act, R.S.C. 1970, c. C-30, and subsequent amendments.

AVIS

La qualité de cette microforme dépend grandement de la qualité de la thèse soumise au microfilmage. Nous avons tout fait pour assurer une qualité supérieure de reproduction.

S'il manque des pages, veuillez communiquer avec l'université qui a conféré le grade.

La qualité d'impression de certaines pages peut laisser à désirer, surtout si les pages originales ont été dactylographiées à l'aide d'un ruban usé ou si l'université nous a fait parvenir une photocopie de qualité inférieure.

La reproduction, même partielle, de cette microforme est soumise à la Loi canadienne sur le droit d'auteur, SRC 1970, c. C-30, et ses amendements subséquents.

UNIVERSITY OF ALBERTA

NONLINEAR DYNAMICS OF PARTICLES IN WAVE FIELDS

BY

JEFFREY M. CANDY



A THESIS

SUBMITTED TO THE FACULTY OF GRADUATE STUDIES AND RESEARCH
IN PARTIAL FULFILMENT OF THE REQUIREMENTS FOR THE DEGREE
OF

MASTER OF SCIENCE
IN
THEORETICAL PHYSICS

DEPARTMENT OF PHYSICS

EDMONTON, ALBERTA

FALL 1990



**National Library
of Canada**

**Bibliothèque nationale
du Canada**

Canadian Theses Service Service des thèses canadiennes

**Ottawa, Canada
K1A 0N4**

The author has granted an irrevocable non-exclusive licence allowing the National Library of Canada to reproduce, loan, distribute or sell copies of his/her thesis by any means and in any form or format, making this thesis available to interested persons.

The author retains ownership of the copyright in his/her thesis. Neither the thesis nor substantial extracts from it may be printed or otherwise reproduced without his/her permission.

L'auteur a accordé une licence irrévocable et non exclusive permettant à la Bibliothèque nationale du Canada de reproduire, prêter, distribuer ou vendre des copies de sa thèse de quelque manière et sous quelque forme que ce soit pour mettre des exemplaires de cette thèse à la disposition des personnes intéressées.

L'auteur conserve la propriété du droit d'auteur qui protège sa thèse. Ni la thèse ni des extraits substantiels de celle-ci ne doivent être imprimés ou autrement reproduits sans son autorisation.

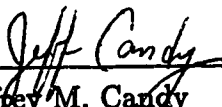
ISBN 0-315-65062-1

UNIVERSITY OF ALBERTA
RELEASE FORM

NAME OF AUTHOR Jeffrey M. Candy
TITLE OF THESIS Nonlinear Dynamics of Particles in Wave Fields
DEGREE Master of Science
YEAR THIS DEGREE GRANTED 1990

Permission is hereby granted to the UNIVERSITY OF ALBERTA LIBRARY to reproduce single copies of this thesis and to lend or sell such copies for private, scholarly or scientific research purposes only.

The author reserves other publication rights, and neither the thesis nor extensive extracts from it may be printed or otherwise reproduced without the author's written permission.



Jeffrey M. Candy
Department of Physics
University of Alberta
Edmonton, Alberta
T6G 2J1

Date: *August 13, 1990.*

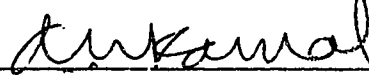
UNIVERSITY OF ALBERTA

FACULTY OF GRADUATE STUDIES AND RESEARCH

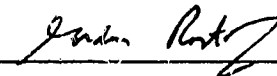
The undersigned certify that they have read, and recommended to the Faculty of Graduate Studies and Research for acceptance, a thesis entitled "Nonlinear Dynamics of Particles in Wave Fields" submitted by Jeffrey M. Candy in partial fulfilment of the requirements for the degree of Master of Science in Theoretical Physics.



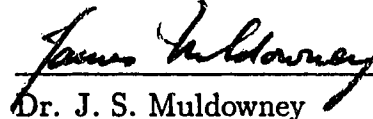
Dr. W. Rozmus, Supervisor



Dr. A. N. Kamal



Dr. G. Rostoker



Dr. J. S. Muldowney

Date: July 4, 1990

ABSTRACT

An algorithm to numerically integrate differential equations derivable from a separable Hamiltonian function is developed. This symplectic algorithm is accurate to fourth order in the time step, and preserves exactly the Poincaré-Cartan integral invariants associated with the topology of the phase flow. We use this algorithm to study the motion of an ion in a spectrum of lower hybrid waves propagating across a constant magnetic field. In particular, we examine to what extent a turbulent spectrum of these electrostatic waves may accelerate thermal ions ($T < 1\text{eV}$). Finally, Lie transform perturbation theory is applied to the Hamiltonian which describes a linear oscillator perturbed by a plane wave. For rational wave frequencies of the form $\nu = r/s$, where r and s are relatively prime integers, it is shown that s^{th} order perturbation theory predicts the occurrence of *intrinsic* resonances.

ACKNOWLEDGEMENTS

During the past two years, I have had the pleasure of studying under the supervision of Dr. Wojciech Rozmus. His guidance, encouragement and perpetual enthusiasm made my work exciting and enjoyable. For this I cannot thank him enough. To Dr. Etienne Forest I am grateful for, among other things, the kind invitation to the Lawrence Berkeley Laboratory, where most of the computational work for Chapter 3 was done.

As well, thanks go to Dr. John Samson for first inviting me to the Space Science Laboratory, where I held a summer research position in 1988. Without access to the computing facilities there, the completion of this thesis would never have been possible. I am also indebted to Martin Connors for his assistance and patience with my affairs on the MicroVAX.

In addition, I would like to acknowledge many enlightening conversations with Robert Teshima, and thank him for his expert advice on solving the horrible system of nonlinear equations which appears in Chapter 2. Finally, I am grateful to Harvey Rose for first mentioning the two important words: *Symplectic Integrator*.

This work was partly supported by the Natural Sciences and Engineering Research Council of Canada.

TABLE OF CONTENTS

1	INTRODUCTION	1
2	SYMPLECTIC INTEGRATION	4
2.1	The Symplectic Structure	4
2.2	A Class of Canonical Transformations	6
2.3	Development of Explicit Algorithms	8
2.3a	The Generating Functions	8
2.3b	Series Expansions for $n \leq 4$	10
2.3c	A 2 nd Order SIA	13
2.3d	A 3 rd Order SIA	14
2.3e	A 4 th Order SIA	14
2.4	Time Dependent Potentials	16
2.5	Numerical Examples	17
2.5a	The Nonlinear Pendulum	17
2.5b	Particle in a Standing Wave Field	18
2.5c	Linear Oscillator Perturbed by a Plane Wave	20
3	STOCHASTIC ION HEATING	22

3.1	A Model of Lower Hybrid Turbulence	24
3.1a	The Model Hamiltonian	24
3.1b	Limiting the Parameter Space	25
3.1c	Initial Conditions of Source Ions	27
3.1d	Method of Integration	28
3.2	Heating with One Mode	29
3.2a	Surfaces of Section	29
3.2b	Ensemble Averaging	30
3.3	Amplitudes of Ordered and Turbulent Wave Spectra	31
3.4	Multiple Mode Stochastic Webs	33
3.4a	Four Modes	34
3.4b	Five Modes	34
3.4c	Six Modes	34
3.5	Heating by a Turbulent Spectrum	35
3.6	The Disappearance of Landau Damping	37
4	PERTURBATIVE ANALYSIS	39
4.1	The Wave Driven Linear Oscillator	39
4.2	Deprit Perturbation Series	40
4.3	Calculation of w_1	42

4.4	Calculation of w_2	45
4.5	Higher-Order Invariants	48
4.6	Implications	50
5	CONCLUSION	52
	BIBLIOGRAPHY	54
	APPENDICES:	57
A	RKI2 AND RKI4 ALGORITHMS	57
B	ISIA4 ALGORITHM	58
C	THE FUNCTION F_v	59
D	THE FUNCTION G_v	61
E	TABLES AND FIGURES	63
F	TABLES AND FIGURES (CONT'D)	79
G	TABLES AND FIGURES (CONT'D)	89
H	TABLES AND FIGURES (CONT'D)	105
I	TABLES AND FIGURES (CONT'D)	123

LIST OF TABLES

F.1	Summary of different choices of algorithms.	85
F.2	Summary of coefficients for various algorithms.	85
F.3	General scheme for a δt time-step integration.	86
F.4	General scheme for a δt time-step integration.	87
F.5	Execution time (in sec.) for various integration methods.	88
H.1	Summary of Turbulent Spectrum Heating Simulations.	122

LIST OF FIGURES

E.1	Comparison of the relative error in energy when using SIA2 and RKI2 to integrate (2.41).	64
E.2	Comparison of the absolute error in position when using SIA2 and RKI2 to integrate (2.41).	65
E.3	Comparison of the relative error in energy when using SIA2 and RKI2 to integrate (2.41).	66
E.4	Comparison of the absolute error in position when using SIA2 and RKI2 to integrate (2.41).	67
E.5	Phase space of (2.43) for $\epsilon = 1/8$	68
E.6	Poincaré map of a single trajectory of (2.43) using SIA4.	69
E.7	Same as in Figure E.6, except using RKI4.	70
E.8	Same as in Figure E.6, except using ISIA4.	71
E.9	Poincaré map of a single trajectory of (2.43) using SIA4.	72
E.10	Same as in Figure E.9, except using RKI4.	73
E.11	Poincaré map of a single trajectory of (2.43) using SIA4.	74
E.12	Same as in Figure E.11, except using RKI4.	75
E.13	Separatrix mesh of (2.45) after averaging.	76
E.14	Poincaré map of a single trajectory of (2.45) using SIA4.	77
E.15	Same as in Figure E.14, except using RKI4.	78

F.1	Poincaré map of a single trajectory of (2.45) using SIA2.	80
F.2	Same as in Figure F.1, except using RKI4.	81
F.3	Separatrix mesh of (2.46) after averaging.	82
F.4	Poincaré map of a single trajectory of (2.46) using SIA4.	83
F.5	Same as in Figure F.4, except using RKI4.	84
G.1	Surface of section of the Hamiltonian (3.2) for $N = 1$	90
G.2	Same as Figure G.1, except $\nu_1 = 5.16$	91
G.3	Surface of section of the Hamiltonian (3.2) for $N = 1$	92
G.4	Same as Figure G.3, except $\nu_1 = 5.16$	93
G.5	Time-averaged ion distribution $N(\rho)$	94
G.6	Same as Figure G.5, except $\epsilon_1 = 1.5$ m.	95
G.7	Same as Figure G.5, except $\epsilon_1 = 2$ m.	96
G.8	Same as Figure G.5, except $\epsilon_1 = 2.5$ m.	97
G.9	Same as Figure G.5, except $\epsilon_1 = 3$ m.	98
G.10	Time-averaged ion distribution $N(\rho)$	99
G.11	Same as Figure G.10, except $\epsilon_1 = 3$ m.	100
G.12	Time-averaged ion distribution $N(\rho)$	101
G.13	Same as Figure G.12, except $\nu_1 = 5.16$ m.	102
G.14	The normalized electric field $\mathcal{E}(x(T), T)$	103

G.15	The normalized electric field $\mathcal{E}(x(T), T)$	104
H.1	Surface of section of the Hamiltonian (3.2) for $N = 4$	106
H.2	Surface of section of the Hamiltonian (3.2) for $N = 5$	107
H.3	Surface of section of the Hamiltonian (3.2) for $N = 6$	108
H.4	Time-averaged ion distribution $N(\rho)$	109
H.5	Same as Figure H.4, except $[\epsilon_{min}, \epsilon_{max}] = [0.5, 1.5]$ m.	110
H.6	Same as Figure H.4, except $[\epsilon_{min}, \epsilon_{max}] = [1, 2]$ m.	111
H.7	Same as Figure H.4, except $[\epsilon_{min}, \epsilon_{max}] = [1.5, 2.5]$ m.	112
H.8	Same as Figure H.4, except $[\epsilon_{min}, \epsilon_{max}] = [2, 2.5]$ m.	113
H.9	Same as Figure H.4, except $[\epsilon_{min}, \epsilon_{max}] = [3, 3.5]$ m.	114
H.10	Time-averaged ion distribution $N(\rho)$	115
H.11	Same as Figure H.10, except $[\epsilon_{min}, \epsilon_{max}] = [0.5, 1.5]$ m.	116
H.12	Same as Figure H.10, except $[\epsilon_{min}, \epsilon_{max}] = [1, 2]$ m.	117
H.13	Same as Figure H.10, except $[\epsilon_{min}, \epsilon_{max}] = [1.5, 2.5]$ m.	118
H.14	Same as Figure H.10, except $[\epsilon_{min}, \epsilon_{max}] = [2, 2.5]$ m.	119
H.15	Same as Figure H.10, except $[\epsilon_{min}, \epsilon_{max}] = [3, 3.5]$ m.	120
H.16	Qualitative particle trajectory in the (\dot{x}, \dot{y}) phase plane.	121
I.1	Contour map of the invariant function $S_\nu^{(1)}$ for $\nu = 3$	124
I.2	Surface of section plot of the Hamiltonian (4.1).	125

I.3	Contour map of the invariant function $S_y^{(2)}$ for $\nu = 5/2$	126
I.4	Surface of section plot of the Hamiltonian (4.1).	127
I.5	Surface of section plot of the Hamiltonian (4.1).	128
I.6	Same as Figure I.5, except $\epsilon = 1.6$	129
I.7	Surface of section plot of the Hamiltonian (4.1).	130
I.8	Surface of section plot of the Hamiltonian (4.1).	131

CHAPTER ONE

INTRODUCTION

Let us begin by considering a simple dynamical system; namely, a particle with mass m and charge e gyrating in a uniform magnetic field $B\hat{z}$ and interacting with an electrostatic wave. The magnetic field in this case may be derived from the vector potential $\mathbf{A} = Bx\hat{y}$. Then, if the wave has amplitude E and temporal frequency ω , the Hamiltonian of the particle can be written as

$$H = \frac{1}{2m} [(m\Omega x)^2 + p_x^2 + p_z^2] + \frac{eE}{k} \cos(k_x x + k_z z - \omega t), \quad (1.1)$$

where $\Omega \equiv eB/m$ is the cyclotron frequency. Note that we have chosen the wavevector $\mathbf{k} = k_x\hat{x} + k_z\hat{z}$ to lie in the x - z plane. That this results in no loss of generality should be clear.

The Hamiltonian (1.1) has been studied in some detail by Smith and Kaufman [34], [35]. By considering the overlap of adjacent resonances, these authors obtained a crude estimate of the onset of global stochasticity according to the well-known Chirikov criterion [8].

More detailed studies, however, have involved a simplified version of (1.1). If one considers the wave to propagate transversely ($k_z = 0$), then the previous Hamiltonian function reduces to

$$H = \frac{1}{2m} [(m\Omega x)^2 + p_x^2] + \frac{eE}{k} \cos(kx - \omega t). \quad (1.2)$$

This Hamiltonian has been examined in the context of particle heating by a lower hybrid wave – the propagation of which is characterized by $k_x \gg k_z$ and $\omega \gg \Omega$. Fukuyama *et al.* [14] have analysed (1.2) in the case where ω is an integer multiple

of Ω , while Karney [19] has considered the more general case of arbitrary wave frequency. Furthermore, Karney has also extended some of the interesting results obtained for (1.2) to the more general Hamiltonian (1.1). Malkov [23] and Zaslavsky *et al.* [37], finally, have studied the equations of motion which result from (1.2) in the presence of an arbitrarily weak magnetic field.

More recently, much attention has been given to the interesting dynamics which occur when the resonance condition $\omega/\Omega \in \mathbb{Z}$ is satisfied. In this case, a web-like separatrix covers the (x, p_x) surface of section in system's phase space. Because of its peculiar structure, this separatrix is referred to as a *stochastic web*. Some interesting properties of the web were shown by Chernikov *et al.* [5] for one wave, and numerically by Murakami *et al.* [26] for up to 20 waves. In addition, Karimabadi and Angelopoulos [18] – using first order perturbation theory – have studied invariant curves in phase space for the interaction of a relativistic particle with an obliquely propagating wave packet of arbitrary polarization. They point out certain limitations and weaknesses associated with the usual nonrelativistic treatment.

Finally, by considering a wave packet composed of an infinite number of modes uniformly spaced in frequency, Zaslavsky *et al.* [38] were able to construct an exact set of symplectic difference equations (i.e., an explicit symplectic map) from the continuous Hamiltonian. The iterates of this map generate a web with remarkable symmetry properties and fractal-like structure. In fact, the geometry of the separatrix mesh in phase space is reminiscent of a Penrose tiling (see [12], [22]). An interesting summary of stochastic webs in general may be found in [7]. Unfortunately, the structure of the electric fields which give rise to such interesting dynamics are often difficult to justify from a physical standpoint.

This main results of this thesis are divided into three distinct and relatively independent chapters. In Chapter 2, we derive a fourth order accurate symplectic integration algorithm for separable Hamiltonian functions. In Chapter 3 this algorithm is applied to a class of Hamiltonians similar in form to (1.2) in order to study a wave-particle interaction model of lower hybrid turbulence. Finally, in Chapter 4, canonical perturbation theory is used to construct resonant invariant functions for (1.2) in the case where ω/Ω is rational.

CHAPTER TWO

SYMPLECTIC INTEGRATION

2.1 The Symplectic Structure

The study of Hamiltonian dynamical systems leads quite often to differential equations which are not solvable analytically. Increasingly, numerical integration is being used to gain insight into the complicated behavior of such systems. Unfortunately, popular integration schemes — including the Runge-Kutta class of algorithms — do not take into account the Hamiltonian nature of the equations and, consequently, do not preserve the hierarchy of global invariants known to exist in these systems.

Consider, for example, a Hamiltonian system with N degrees of freedom and an N -dimensional configuration manifold \mathcal{M} . Let \mathbf{q} be the local coordinates on \mathcal{M} . It can be shown that the cotangent bundle of \mathcal{M} , written $T^*\mathcal{M}$, has the structure of a $2N$ -dimensional differentiable manifold with local coordinates (\mathbf{q}, \mathbf{p}) , where \mathbf{p} is the usual canonical momentum vector (see [1] for details). On the cotangent bundle $T^*\mathcal{M}$ there exists the natural symplectic structure

$$\omega^2 = d\mathbf{p} \wedge d\mathbf{q},$$

which is a closed, non-degenerate, differential two-form. We call the pair $(T^*\mathcal{M}, \omega^2)$ a symplectic manifold. The forms $\omega^2, (\omega^2)^2, \dots, (\omega^2)^N$ are preserved under both the phase flow of the system and under canonical transformations. Collectively, these forms are referred to as the integral invariants of Poincaré. In fact, when integrated over an arbitrary region of dimension $2k$ ($1 \leq k \leq N$), the $2k$ -form ω^{2k} will produce

the following invariant quantity

$$\int \cdots \int \sum_{i_1 < \cdots < i_k} dp_{i_1} \cdots dp_{i_k} dq_{i_1} \cdots dq_{i_k}$$

which is proportional to the sum of the oriented volumes of projections onto the coordinate spaces $(p_{i_1}, \dots, p_{i_k}, q_{i_1}, \dots, q_{i_k})$, where $1 \leq i_m \leq N$. When $k = N$, we recover Liouville's Theorem.

A brief summary of existing symplectic integration algorithms (SIAs) is provided by Channell and Scovel [4]. In addition to the methods discussed there, Itoh and Abe [17] have recently developed a (nonsymplectic) method of integration based on discrete mechanics which exactly preserves the Hamiltonian. Their algorithms, however, are accurate only up to second order in the time step and, like the schemes proposed by Channell and Scovel, require the solution of implicit equations. Ruth [28], however, has devised an explicit method of symplectic integration which is structurally quite similar to the classical Runge-Kutta algorithms (RKIs). In what follows, we generalize his approach, and extend the accuracy of the method to 4th order in the time step.¹

The resulting explicit SIA is superior in both computational efficiency and global stability to the most popular 4th order RKI [25], [27].

¹A manuscript containing the results of this chapter was submitted to *J. Comp. Phys.* in July 1989, and was subsequently accepted for publication. However, the 4th order symplectic algorithm – the main result of this paper – has been derived independently by Etienne Forest and Ron Ruth [13].

2.2 A Class of Canonical Transformations

Let us begin by considering a Hamiltonian $H : \mathbb{R}^N \times \mathbb{R}^N \rightarrow \mathbb{R}$ which is separable with respect to the local coordinates \mathbf{q} and momenta \mathbf{p} ,

$$H(\mathbf{q}, \mathbf{p}) = T(\mathbf{p}) + V(\mathbf{q}) \quad (2.1)$$

where $\mathbf{q} = \{q_\alpha\}$, $\mathbf{p} = \{p_\alpha\}$, $\alpha = 1, \dots, N$. It is our goal to produce a series of difference equations which preserve the symplectic two-form $\omega^2 = dp \wedge dq$, and approximate the exact phase flow generated by H :

$$(\mathbf{q}_0, \mathbf{p}_0) \text{ at time } t_0 \longrightarrow (\mathbf{q}, \mathbf{p}) \text{ at time } t. \quad (2.2)$$

The accuracy of the approximation resulting from replacing Hamilton's equations by such a series of difference equations will be measured in terms of the time step $\delta t = t - t_0$. More specifically, if a difference approximation agrees with Hamilton's equations up to $O(\delta t^n)$, then we will call that approximation an n^{th} order SIA. In what follows, let us consider $(\mathbf{q}_0, \mathbf{p}_0)$ to be initial conditions, and (\mathbf{q}, \mathbf{p}) to be the local coordinates and momenta after a time δt . Now, finding an n^{th} order SIA is equivalent to finding a canonical transformation \mathcal{C} which generates the map

$$\mathcal{C} : (\mathbf{q}, \mathbf{p}) \longrightarrow (\tilde{\mathbf{q}}_0, \tilde{\mathbf{p}}_0) = (\mathbf{q}_0, \mathbf{p}_0) + O(\delta t^{n+1}), \quad (2.3)$$

where the tildes indicate approximate initial conditions. In particular, if we can find a series of transformations which leave the Hamiltonian with the final form

$$H(\tilde{\mathbf{q}}_0, \tilde{\mathbf{p}}_0) = \sum_{i=n}^{\infty} h_i(\tilde{\mathbf{q}}_0, \tilde{\mathbf{p}}_0) \delta t^i \quad (2.4)$$

such that $\tilde{\mathbf{q}}_0 \rightarrow \mathbf{q}_0$ and $\tilde{\mathbf{p}}_0 \rightarrow \mathbf{p}_0$ as $\delta t \rightarrow 0$, then one can prove that the equality in (2.3) is satisfied. Indeed, if we expand $(\tilde{\mathbf{q}}_0, \tilde{\mathbf{p}}_0)$ and $h_i(\tilde{\mathbf{q}}_0, \tilde{\mathbf{p}}_0)$ about $t = t_0$ in the

following way,

$$\begin{aligned}(\tilde{q}_0, \tilde{p}_0) &= (q_0, p_0) + \sum_{j=1}^{\infty} (q^{(j)}, p^{(j)}) \delta t^j \\ h_i(\tilde{q}_0, \tilde{p}_0) &= h_i(q_0, p_0) + O(\delta t)\end{aligned}$$

then Hamilton's equations imply

$$\begin{aligned}\left(\frac{d}{dt} \tilde{q}_0, \frac{d}{dt} \tilde{p}_0\right) &= \sum_{i=n}^{\infty} \left(\frac{\partial}{\partial \tilde{p}_0}, -\frac{\partial}{\partial \tilde{q}_0}\right) h_i(\tilde{q}_0, \tilde{p}_0) \delta t^i \\ &= \delta t^n \left[\left(\frac{\partial}{\partial \tilde{p}_0}, -\frac{\partial}{\partial \tilde{q}_0}\right) h_n\right]_{\tilde{q}_0 = q_0, \tilde{p}_0 = p_0} + O(\delta t^{n+1}) \\ &= \mathbf{G}(q_0, p_0) \delta t^n + O(\delta t^{n+1}),\end{aligned}$$

where \mathbf{G} is some vector function of the initial conditions. Upon integration of the above results, we obtain the relationship between the exact and approximate initial conditions.

$$(\tilde{q}_0, \tilde{p}_0) = (q_0, p_0) + \frac{\mathbf{G}}{n+1} \delta t^{n+1} + O(\delta t^{n+2}) \tag{2.5}$$

$$= (q_0, p_0) + O(\delta t^{n+1}) \tag{2.6}$$

One may conclude, then, that if a canonical transformation \mathcal{C} (or a series of such transformations) transforms the Hamiltonian (2.1) into the form of (2.4), then the resulting algebraic equations of transformation constitute an n^{th} order SIA.

2.3 Development of Explicit Algorithms

We are now faced with the question: How does one transform a Hamiltonian (2.1) into the form (2.4)? Fortunately, this question has been answered by Ruth [28], who has obtained explicit algorithms accurate to 3rd order. This is in contrast to the recently developed implicit methods of Channell and Scovel [4], and of Itoh and Abe [17], which are somewhat less convenient for practical use in most cases.

2.3a The Generating Functions

To obtain an integration algorithm accurate to order n , we make the following series of l canonical transformations,

$$(\mathbf{q}_l, \mathbf{p}_l) \xrightarrow{K_l} (\mathbf{q}_{l-1}, \mathbf{p}_{l-1}) \xrightarrow{K_{l-1}} \dots \xrightarrow{K_1} (\mathbf{q}_0, \mathbf{p}_0). \quad (2.7)$$

When $n \leq 4$, one can always set $l = n$. However, it may be necessary to use $l > n$ transformations when $n > 4$. This necessity is a result of the rapid accumulation with increasing n of independent conditions which must be satisfied to put H into the form (2.4). The reader familiar with classical Runge-Kutta formulae will recall a similar rise in the number of coefficients required to derive an algorithm of order greater than four. In any case, the above variables have the interpretation

$$\begin{aligned} (\mathbf{q}_0, \mathbf{p}_0) &\longrightarrow \text{initial conditions at time } t = 0 \\ (\mathbf{q}_1, \mathbf{p}_1) &\longrightarrow \text{intermediate point} \\ &\vdots \\ (\mathbf{q}_{l-1}, \mathbf{p}_{l-1}) &\longrightarrow \text{intermediate point} \\ (\mathbf{q}_l, \mathbf{p}_l) &\longrightarrow \text{integrated variables at time } t = t_0 + \delta t. \end{aligned}$$

and

$$K_i(\mathbf{q}_{i-1}, \mathbf{p}_i, t) = -\mathbf{q}_{i-1} \cdot \mathbf{p}_i - [a_i T(\mathbf{p}_i) + b_i V(\mathbf{q}_{i-1})] \delta t \quad (2.8)$$

are type 3 generating functions for $i = 1, \dots, l$. This choice of K_i yields the following equations of transformation

$$\mathbf{q}_i = -\nabla_{\mathbf{p}_i} K_i = \mathbf{q}_{i-1} + \delta t a_i \nabla_{\mathbf{p}_i} T(\mathbf{p}_i) \quad (2.9)$$

$$\mathbf{p}_{i-1} = -\nabla_{\mathbf{q}_{i-1}} K_i = \mathbf{p}_i + \delta t b_i \nabla_{\mathbf{q}_{i-1}} V(\mathbf{q}_{i-1}) \quad (2.10)$$

and,

$$H_{i-1}(\mathbf{q}_{i-1}, \mathbf{p}_{i-1}) = H_i + \partial_i K_i = H_i - [a_i T(\mathbf{p}_i) + b_i V(\mathbf{q}_{i-1})], \quad (2.11)$$

again, for $i = 1, \dots, l$. The gradient operators we use here are defined according to

$$\nabla_{\mathbf{q}} \equiv \left(\frac{\partial}{\partial q_1}, \dots, \frac{\partial}{\partial q_N} \right)$$

$$\nabla_{\mathbf{p}} \equiv \left(\frac{\partial}{\partial p_1}, \dots, \frac{\partial}{\partial p_N} \right).$$

Upon applying all l transformations, it is clear that the Hamiltonian for the initial conditions, H_0 , will have the form

$$\begin{aligned} H_0(\mathbf{q}_0, \mathbf{p}_0) &= H_l(\mathbf{q}_l, \mathbf{p}_l) + \sum_{i=1}^l \partial_i K_i \\ &= T(\mathbf{p}_l) + V(\mathbf{q}_l) - \sum_{i=1}^l [a_i T(\mathbf{p}_i) + b_i V(\mathbf{q}_{i-1})]. \end{aligned} \quad (2.12)$$

Where in the above we must consider $\mathbf{q}_i = \mathbf{q}_i(\mathbf{q}_0, \mathbf{p}_0)$ and $\mathbf{p}_i = \mathbf{p}_i(\mathbf{q}_0, \mathbf{p}_0)$. At the moment, however, the relationships between variables are implicit, the exact form of which follows at once from the equations of transformation (2.9) and (2.10):

$$\mathbf{q}_i = \mathbf{q}_0 + \delta t \sum_{m=1}^i a_m \mathbf{P}(\mathbf{p}_m) \quad (2.13)$$

$$\mathbf{p}_i = \mathbf{p}_0 + \delta t \sum_{m=1}^i b_m \mathbf{F}(\mathbf{q}_{m-1}), \quad (2.14)$$

true for $i = 1, \dots, l$. Note that we have introduced the generalized force $\mathbf{F}(\mathbf{q}) = -\nabla_{\mathbf{q}}V(\mathbf{q})$, as well as the gradient of kinetic energy $\mathbf{P}(\mathbf{p}) = \nabla_{\mathbf{p}}T(\mathbf{p})$. Now, if one can determine the coefficients $\{a_i, b_i\}$ such that the Hamiltonian has the form $H_0 = O(\delta t^n)$, then (2.9) and (2.10) describe an l -step process for the integration $(\mathbf{q}_0, \mathbf{p}_0) \rightarrow (\mathbf{q}_l, \mathbf{p}_l)$ which is exactly symplectic (since it is always a canonical transformation). In practice, to determine the coefficients $\{a_i, b_i\}$, one must expand \mathbf{q}_i and \mathbf{p}_i , and all associated functions in powers of δt so that H_0 may take the form

$$H_0(\mathbf{q}_0, \mathbf{p}_0) = \sum_{m=0}^{n-1} h_m(\{a_i, b_i\}, \mathbf{q}_0, \mathbf{p}_0) \delta t^m + O(\delta t^n), \quad (2.15)$$

in which case $\{a_i, b_i\}$ are found, not necessarily uniquely, by setting $h_m = 0$ for $m = 0, \dots, n-1$.

2.3b Series Expansions for $n \leq 4$

Let us now perform the required algebra to find a 4th order algorithm. Since methods of order 1, 2 and 3 are simpler cases of the order 4 method, we shall not yet specify the number $l = n \leq 4$ of transformations. First, we expand \mathbf{q}_i and \mathbf{p}_i in powers of δt ,

$$\mathbf{q}_i = \mathbf{q}_0 + \delta t \Gamma_i + \delta t^2 \Lambda_i + \delta t^3 \Psi_i + O(\delta t^4) \quad (2.16)$$

$$\mathbf{p}_i = \mathbf{p}_0 + \delta t \Theta_i + \delta t^2 \Phi_i + \delta t^3 \Pi_i + O(\delta t^4) \quad (2.17)$$

with the coefficients given by

$$\begin{aligned} \Gamma_i &= \mathbf{P} \sum_{m=1}^i a_m \\ \Lambda_i &= (\mathbf{F} \cdot \nabla_{\mathbf{p}}) \mathbf{P} \sum_{m=1}^i a_m \sum_{r=1}^m b_r \\ \Psi_i &= \frac{(\mathbf{F} \cdot \nabla_{\mathbf{p}})^2}{2} \mathbf{P} \sum_{m=1}^i a_m \left[\sum_{r=1}^m b_r \right]^2 + [((\mathbf{P} \cdot \nabla_{\mathbf{q}}) \mathbf{F}) \cdot \nabla_{\mathbf{p}}] \mathbf{P} \sum_{m=2}^i a_m \sum_{r=2}^m b_r \sum_{s=1}^{r-1} a_s \end{aligned}$$

$$\begin{aligned}\Theta_i &= \mathbf{F} \sum_{m=1}^i b_m \\ \Phi_i &= (\mathbf{P} \cdot \nabla_{\mathbf{q}}) \mathbf{F} \sum_{m=2}^i b_m \sum_{r=1}^{m-1} a_r \\ \Pi_i &= \frac{(\mathbf{P} \cdot \nabla_{\mathbf{q}})^2}{2} \mathbf{F} \sum_{m=2}^i b_m \left[\sum_{r=1}^{m-1} a_r \right]^2 + [((\mathbf{F} \cdot \nabla_{\mathbf{p}}) \mathbf{P}) \cdot \nabla_{\mathbf{q}}] \mathbf{F} \sum_{m=2}^i b_m \sum_{r=1}^{m-1} a_r \sum_{s=1}^r b_s.\end{aligned}$$

The coefficients above are evaluated, after application of the gradient operators, at $\mathbf{q} = \mathbf{q}_0$ and $\mathbf{p} = \mathbf{p}_0$. That is, they are explicit functions of the *initial conditions only*. Further, they are valid for $i = 1, \dots, n$. In a similar manner, we can expand $V(\mathbf{q}_i)$ and $T(\mathbf{p}_i)$:

$$\begin{aligned}V(\mathbf{q}_i) &= V(\mathbf{q}_0) + \delta t [\Gamma_i \cdot \nabla_{\mathbf{q}}] V(\mathbf{q}) + \delta t^2 \left[\Lambda_i \cdot \nabla_{\mathbf{q}} + \frac{(\Gamma_i \cdot \nabla_{\mathbf{q}})^2}{2} \right] V(\mathbf{q}) \\ &\quad + \delta t^3 \left[\Psi_i \cdot \nabla_{\mathbf{q}} + \frac{(\Gamma_i \cdot \nabla_{\mathbf{q}})^3}{6} + (\Gamma_i \cdot \nabla_{\mathbf{q}})(\Lambda_i \cdot \nabla_{\mathbf{q}}) \right] V(\mathbf{q}) \\ &\quad + O(\delta t^4)\end{aligned}\tag{2.18}$$

and

$$\begin{aligned}T(\mathbf{p}_i) &= T(\mathbf{p}_0) + \delta t [\Theta_i \cdot \nabla_{\mathbf{p}}] T(\mathbf{p}) + \delta t^2 \left[\Phi_i \cdot \nabla_{\mathbf{p}} + \frac{(\Theta_i \cdot \nabla_{\mathbf{p}})^2}{2} \right] T(\mathbf{p}) \\ &\quad + \delta t^3 \left[\Pi_i \cdot \nabla_{\mathbf{p}} + \frac{(\Theta_i \cdot \nabla_{\mathbf{p}})^3}{6} + (\Theta_i \cdot \nabla_{\mathbf{p}})(\Phi_i \cdot \nabla_{\mathbf{p}}) \right] T(\mathbf{p}) \\ &\quad + O(\delta t^4).\end{aligned}\tag{2.19}$$

Again, after the derivatives are taken, these expressions are evaluated at the initial conditions $(\mathbf{q}_0, \mathbf{p}_0)$. Upon substitution of the above expressions into (2.12), we arrive at a Hamiltonian with the form (2.15)

$$H_0(\mathbf{q}_0, \mathbf{p}_0) = h_0 + h_1 \delta t + h_2 \delta t^2 + h_3 \delta t^3 + O(\delta t^4),\tag{2.20}$$

where the zero-order term is

$$h_0 = T(\mathbf{p}_0) \left[1 - \sum_{i=1}^n a_i \right] + V(\mathbf{q}_0) \left[1 - \sum_{i=1}^n b_i \right].$$

To avoid possible confusion, we will abbreviate $\mathbf{F}_0 = \mathbf{F}(\mathbf{q}_0)$ and $\mathbf{P}_0 = \mathbf{P}(\mathbf{p}_0)$. This allows us to write

$$h_1 = (\mathbf{F}_0 \cdot \mathbf{P}_0) \left[\sum_{m=1}^n b_m - \sum_{i=1}^n a_i \sum_{m=1}^i b_m - \sum_{m=1}^n a_m + \sum_{i=2}^n b_i \sum_{m=1}^{i-1} a_m \right],$$

and

$$\begin{aligned} h_2 = & (\mathbf{P}_0 \cdot \nabla_{\mathbf{q}})(\mathbf{F} \cdot \mathbf{P}_0) \left[\sum_{m=2}^n b_m \sum_{r=1}^{m-1} a_r - \sum_{i=2}^n a_i \sum_{m=2}^i b_m \sum_{r=1}^{m-1} a_r \right. \\ & \left. - \frac{1}{2} \left(\sum_{m=1}^n a_m \right)^2 + \frac{1}{2} \sum_{i=2}^n b_i \left(\sum_{m=1}^{i-1} a_m \right)^2 \right] \\ & - (\mathbf{F}_0 \cdot \nabla_{\mathbf{p}})(\mathbf{P} \cdot \mathbf{F}_0) \left[\sum_{m=1}^n a_m \sum_{r=1}^m b_r - \sum_{i=2}^n b_i \sum_{m=1}^{i-1} a_m \sum_{r=1}^m b_r \right. \\ & \left. - \frac{1}{2} \left(\sum_{m=1}^n b_m \right)^2 + \frac{1}{2} \sum_{i=1}^n a_i \left(\sum_{m=1}^i b_m \right)^2 \right]. \end{aligned}$$

It can be shown, finally, that h_3 has the following lengthy expansion,

$$\begin{aligned} h_3 = & (\mathbf{P}_0 \cdot \nabla_{\mathbf{q}})^2(\mathbf{F} \cdot \mathbf{P}_0) \left[\frac{1}{2} \sum_{m=2}^n b_m \left(\sum_{r=1}^{m-1} a_r \right)^2 \right. \\ & \left. - \frac{1}{2} \sum_{i=2}^n a_i \sum_{m=2}^i b_m \left(\sum_{r=1}^{m-1} a_r \right)^2 - \frac{1}{6} \left(\sum_{m=1}^n a_m \right)^3 + \frac{1}{6} \sum_{i=2}^n b_i \left(\sum_{m=1}^{i-1} a_m \right)^3 \right] \\ & - (\mathbf{F}_0 \cdot \nabla_{\mathbf{p}})^2(\mathbf{P} \cdot \mathbf{F}_0) \left[\frac{1}{2} \sum_{m=1}^n a_m \left(\sum_{r=1}^m b_r \right)^2 \right. \\ & \left. - \frac{1}{2} \sum_{i=2}^n b_i \sum_{m=1}^{i-1} a_m \left(\sum_{r=1}^m b_r \right)^2 - \frac{1}{6} \left(\sum_{m=1}^n b_m \right)^3 + \frac{1}{6} \sum_{i=1}^n a_i \left(\sum_{m=1}^i b_m \right)^3 \right] \\ & + (\mathbf{P}_0 \cdot \nabla_{\mathbf{q}})(\mathbf{F}_0 \cdot \nabla_{\mathbf{p}})(\mathbf{P} \cdot \mathbf{F}) \left[\sum_{m=2}^n b_m \sum_{r=1}^{m-1} a_r \sum_{s=1}^r b_s - \sum_{m=2}^n a_m \sum_{r=2}^m b_r \sum_{s=1}^{r-1} a_s \right. \\ & \left. - \sum_{i=2}^n a_i \sum_{m=2}^i b_m \sum_{r=1}^{m-1} a_r \sum_{s=1}^r b_s + \sum_{i=3}^n b_i \sum_{m=2}^{i-1} a_m \sum_{r=2}^{m-1} b_r \sum_{s=1}^{r-1} a_s \right. \\ & \left. + \sum_{m=2}^n b_m \sum_{m=2}^n b_m \sum_{r=1}^{m-1} a_r - \sum_{i=2}^n a_i \sum_{m=1}^i b_m \sum_{m=2}^i b_m \sum_{r=1}^{m-1} a_r \right. \\ & \left. - \sum_{m=1}^n a_m \sum_{m=1}^n a_m \sum_{r=1}^m b_r + \sum_{i=2}^n b_i \sum_{m=1}^{i-1} a_m \sum_{m=1}^{i-1} a_m \sum_{r=1}^m b_r \right]. \end{aligned}$$

As before, each of the expressions h_0, \dots, h_3 is to be evaluated at the initial conditions $(\mathbf{q}_0, \mathbf{p}_0)$. Using the results we have derived so far, it is possible to construct algorithms of orders 1,2,3 and 4 by making the choices shown in Table F.1. The coefficients which result from these choices are listed in Table F.2. Once the coefficients $\{a_i, b_i\}$ are known, we have the prescription shown in Table F.3 for an n^{th} order integrator. Of course, algorithms of order ≤ 3 have been derived by Ruth [28], but we will include a general treatment of them for completeness. The case $n = 1$ is trivial, but for $n = 2$, one obtains the so-called *leapfrog* method which we will derive in the next section.

2.3c A 2nd Order SIA

According to Table 1, if we set h_0 and h_1 equal to zero, and choose $n = 2, 3$ equations in 4 variables result.

$$a_1 + a_2 = 1 \quad (2.21)$$

$$b_1 + b_2 = 1 \quad (2.22)$$

$$a_1 b_1 + a_2 = b_2 a_1 \quad (2.23)$$

Two particularly interesting solutions are the *leapfrog* method

$$(a_1, a_2, b_1, b_2) = \left(\frac{1}{2}, \frac{1}{2}, 0, 1\right),$$

and the *pseudo-leapfrog* method

$$(a_1, a_2, b_1, b_2) = \left(1, 0, \frac{1}{2}, \frac{1}{2}\right).$$

These coefficients are implemented into a numerical integration scheme according to Table F.3.

2.3d A 3rd Order SIA

In this case $n = 3$ and h_0, h_1, h_2 must be set equal to zero. One is then left with 5 equations in 6 variables.

$$a_1 + a_2 + a_3 = 1 \quad (2.24)$$

$$b_1 + b_2 + b_3 = 1 \quad (2.25)$$

$$b_2 a_1 + b_3(a_1 + a_2) = \frac{1}{2} \quad (2.26)$$

$$a_1 b_1^2 + a_2(b_1 + b_2)^2 + a_3 = \frac{1}{3} \quad (2.27)$$

$$b_2 a_1^2 + b_3(a_1 + a_2)^2 = \frac{1}{3} \quad (2.28)$$

A solution found originally by Ruth [28] is

$$(a_1, a_2, a_3, b_1, b_2, b_3) = \left(\frac{2}{3}, -\frac{2}{3}, 1, \frac{7}{24}, \frac{3}{4}, -\frac{1}{24}\right).$$

Again, these coefficients are implemented according to the procedure in Table F.3.

2.3e A 4th Order SIA

One of the most popular methods used for numerical integration of differential equations is the 4th order RKI shown in Appendix A. However, this RKI is not symplectic, and requires 4 evaluations of the force \mathbf{F} per time step. The SIA that we will now present requires only 3 evaluations of the force per time step, and, because of its canonical nature, preserves more accurately global phase space structures. Setting h_0, h_1, h_2 and h_3 equal to zero yields 8 equations in 8 variables.

$$a_1 + a_2 + a_3 + a_4 = 1 \quad (2.29)$$

$$b_1 + b_2 + b_3 + b_4 = 1 \quad (2.30)$$

$$b_2 a_1 + b_3(a_1 + a_2) + b_4(1 - a_4) = \frac{1}{2} \quad (2.31)$$

$$a_1 b_1^2 + a_2(b_1 + b_2)^2 + a_3(1 - b_4)^2 + a_4 = \frac{1}{3} \quad (2.32)$$

$$b_2 a_1^2 + b_3(a_1 + a_2)^2 + b_4(1 - a_4)^2 = \frac{1}{3} \quad (2.33)$$

$$a_1 b_1^3 + a_2(b_1 + b_2)^3 + a_3(1 - b_4)^3 + a_4 = \frac{1}{4} \quad (2.34)$$

$$b_2 a_1^3 + b_3(a_1 + a_2)^3 + b_4(1 - a_4)^3 = \frac{1}{4} \quad (2.35)$$

$$\begin{aligned} & b_2 a_1 + b_3(a_1 + a_2)[a_1 b_1 + a_2(b_1 + b_2)] + b_4(1 - a_4)\left[\frac{1}{2} - a_4\right] \\ &= a_2(b_1 + b_2)[b_2 a_1] + a_3(1 - b_4)\left[\frac{1}{2} - b_4(1 - a_4)\right] + \frac{1}{2} a_4 \end{aligned} \quad (2.36)$$

It can be shown that the following is an analytic solution of the equations

$$a_1 = a_4 = \frac{1}{6}(2 + 2^{1/3} + 2^{-1/3})$$

$$a_2 = a_3 = \frac{1}{6}(1 - 2^{1/3} - 2^{-1/3})$$

$$b_1 = 0$$

$$b_2 = b_4 = \frac{1}{2 - 2^{1/3}}$$

$$b_3 = \frac{1}{1 - 2^{2/3}}$$

A similar solution exists for which only 3 evaluations of \mathbf{P} are necessary.

2.4 Time Dependent Potentials

The case where the potential V is an explicit function of time is easily accounted for. Let us begin by assuming we have a Hamiltonian $H : \mathbb{R}^N \times \mathbb{R}^N \times \mathbb{R} \rightarrow \mathbb{R}$,

$$H(\mathbf{q}, \mathbf{p}, t) = T(\mathbf{p}) + V(\mathbf{q}, t). \quad (2.37)$$

If we define the type 1 generating function $\mathcal{F} = p_\varphi t$, then time can be eliminated by introducing the canonically conjugate pair (φ, p_φ) . The equations of transformation are

$$\varphi = \frac{\partial \mathcal{F}}{\partial p_\varphi} = t \quad (2.38)$$

$$H_{new} = H + \partial_t \mathcal{F} = H + p_\varphi \quad (2.39)$$

Note that φ is numerically equal to t , and that $p_\varphi = -H(\mathbf{q}, \mathbf{p}, t) + \text{constant}$. Upon substitution, we find

$$H_{new}(\mathbf{q}, \varphi, \mathbf{p}, p_\varphi) = [T(\mathbf{p}) + p_\varphi] + V(\mathbf{q}, \varphi), \quad (2.40)$$

which is equivalent to (2.1), but extended to $N + 1$ degrees of freedom. Table F.4 shows the prescription for integrating the equations of motion corresponding to the Hamiltonian (2.37), with the generalized force defined by $\mathbf{F}(\mathbf{q}, t) = -\nabla_{\mathbf{q}} V(\mathbf{q}, t)$.

2.5 Numerical Examples

All numerical calculations quoted in this paper were done using a version of VAX FORTRAN which was compiled and run on a DEC MicroVAX II computer. The double-precision (REAL*8) format was used for all floating point numbers since the accuracy of single-precision (REAL*4) variables is insufficient for long-time numerical integration.

2.5a The Nonlinear Pendulum

Our first example is the nonlinear pendulum, which is described by the following Hamiltonian

$$H(q, p) = \frac{p^2}{2} - \cos q. \quad (2.41)$$

The solutions for $q(t)$ and $p(t)$ are well-known, and can be expressed in terms of Jacobian elliptic functions [30]. If we impose the initial conditions $q(0) = 0$ and $p(0) = p_0$, then

$$\begin{aligned} q(t) &= 2 \operatorname{am}\left(\frac{t}{k}, k\right) \\ p(t) &= \pm \frac{2}{k} \operatorname{dn}\left(\frac{t}{k}, k\right) \end{aligned}$$

where $k^2 = 4/p_0^2$. Using these analytical results, we were able to monitor exactly the errors in p and q , as well as the error in energy. The RKIs which we shall use for comparative purposes are listed in Appendix A. For the sake of brevity, the 2nd order Runge-Kutta method shall be called RKI2, and the 4th order method RKI4. Similarly, the leapfrog method of Section 2.3c will hereby be referred to as SIA2, and the method of Section 2.3e will be called SIA4. Figures E.1 and Figures E.2 compare the accuracy of SIA2 and RKI2, while Figures E.3 and E.4 compare the

accuracy of SIA4 and RKI4. In both cases, we see that the energy error for the SIAs is very small, and tends to oscillate about some small central value, while the energy error for the RKIs increases monotonically. This characteristic has been noted by previous authors, most notably in [4].

The SIAs also reproduce the coordinate q more accurately than the RKIs. However, the symplectic methods show a higher rate of growth of coordinate error than of energy error. This phenomena is appropriately described as the propagation of a phase error [17] in the SIA.

2.5b Particle in a Standing Wave Field

The equation of motion

$$m\ddot{q} = -eE [\sin(kq - \omega t) + \sin(kq + \omega t)] \quad (2.42)$$

describes the motion of a particle of mass m , charge $-e$, in the field of a standing wave. Choosing units such that $\omega = k = m = 1$, we find that the above reduces to

$$\ddot{q} + \epsilon \sin q \cos t = 0$$

where $\epsilon = 2eE/m$. This equation is derivable from the time-dependent Hamiltonian function

$$H(q, p, t) = \frac{p^2}{2} - \epsilon \cos q \cos t \quad (2.43)$$

A crude estimate of the stochasticity threshold can be obtained by the resonance overlap criteria of Chirikov [8]. When $\epsilon \geq 1/2$, separatrices corresponding to each wave in (2.42) overlap, indicating that stochastic regions must be present in the phase space. Further, Schmidt [31] has shown that the ponderomotive potential well (see Figure E.5) destabilizes at $\epsilon \sim 0.454$. While we are not interested in

numerically testing these estimates of the onset of stochasticity, our examples show that chaotic regions do indeed exist locally for values of ϵ much smaller than these estimates.

We begin the comparison by integrating the Hamiltonian (2.43) inside the ponderomotive potential well, and displaying the results at the times $t_m = 2\pi m$, $m = 0, 1, 2, \dots, n$; where n is the total number of plotted points. This procedure defines our Poincaré return map. Comparing Figure E.6 and Figure E.7, we notice that SIA4 yields trajectories which lie on a well-defined submanifold while RKI4 seems to exhibit chaos. Actually, the unstable behavior of RKI4 in Figure E.7 is a result of its inability to accurately preserve the local constant of motion which defines the one-dimensional trajectory seen in Figure E.6. This numerical dissipation, which is also evident in Figure E.3, causes RKI4 to be weakly attracted to the elliptic fixed point at $(q, p) = (\pi, 0)$. In addition, we have included in Figure E.8 the trajectories calculated using a 4th order algorithm generated by the prescription in [4] (see Appendix B), which we shall call ISIA4. As in the case of SIA4, ISIA4 shows a stable, regular trajectory.

An added consideration in the comparison of various methods is computational efficiency. Using the initial conditions $(q_0, p_0, t_0) = (\pi, 0.5, 0)$, and perturbation strength $\epsilon = 1/4\pi \simeq 0.080$, we integrated the system corresponding to the Hamiltonian (2.43) forward in time $n = 10000$ time-steps. The results, using three different values of the time-step δt , are shown in Table F.5. The FORTRAN source code for ISIA4 solved the implicit equation for the integrated coordinate according to a simple fixed point iteration scheme with numerical accuracy $O(10^{-16})$. Other than this crude method of solution, the computer code was carefully optimized. As can be seen, ISIA4 benefits from having a small time-step. In the next section, we will encounter a situation where the iteration scheme used in ISIA4 fails to converge.

A further example of the stability of SIA4 can be seen in Figure E.9, where the Poincaré map reveals the existence of a local constant of motion. In Figure E.10, however, we see that the equivalent trajectory calculated by RKI4 experiences numerical dissipation which eventually overwhelms the calculation. Interestingly, the difference between integrators is most easily noticed for regular trajectories of this sort. In the case when the motion is chaotic, the violation of topological invariants in phase space by Runge-Kutta methods is not so easily identified. Figures E.11 and E.12, which show the development of a stochastic layer in the vicinity of the ponderomotive potential well separatrix, illustrate this difficulty.

2.5c Linear Oscillator Perturbed by a Plane Wave

The motion of a charged particle in a constant magnetic field (directed along the z -axis) perturbed by a plane electrostatic wave (propogating along the x -axis) is described by the equation

$$\ddot{x} + \Omega^2 x = \epsilon \sin(kx - \omega t). \quad (2.44)$$

In this equation, Ω is the cyclotron frequency, and ω is the temporal frequency of the electrostatic wave. In the case of exact resonance $\omega = n\Omega$, equation (2.44) generates a stochastic web in phase space. Choosing units where $\Omega = k = 1$, and calling $q = x$, $p = \dot{x}$, equation (2.44) is easily seen to be derivable from the Hamiltonian

$$H(q, p, t) = \frac{p^2}{2} + \frac{q^2}{2} + \epsilon \cos(q - \omega t). \quad (2.45)$$

where we shall assume ω is an integer, so that the resonance condition holds. This system has been studied by Chernikov, *et. al.* [5]. A slightly more general Hamiltonian

$$H(q, p, t) = \frac{p^2}{2} + \frac{q^2}{2} + \epsilon \sum_{i=1}^s \cos(q - \omega_i t), \quad (2.46)$$

describes the situation when there exist s perturbing electrostatic waves, each with the same wavenumber and amplitude, but with differing temporal frequencies ω_i . This more general system has been examined numerically by Murakami, *et. al.* [26].

First, we integrated the system corresponding to (2.45) for relatively small values of the parameter ϵ , and $\omega = 7$. The Poincaré mappings were generated by plotting points at discrete times $t_m = 2\pi m/7$. Initial conditions were chosen with the particle on the separatrix net, with the results for SIA4 and RKI4 shown in Figures E.14 and E.15 respectively. These can be compared with the shape of the separatrix mesh (accurate to $O(\epsilon)$) in Figure E.13, which can be obtained through averaging or perturbation methods (see Chapter 4). This net is formed as a result of the intersection of resonant tori, and can be shown to decrease in thickness rapidly with increasing particle velocity. Figure E.14 shows the separatrix mesh traced by SIA4 to indeed be quite thin, even though the dynamics within the mesh is chaotic. Figure E.15, on the other hand, shows RKI4 slowly spiralling into stable fixed points. Of physical interest for the Hamiltonian (2.45) is to what extent the particle can absorb energy from the electrostatic wave and be accelerated to high velocities. Determination of the possibility of such particle diffusion requires very-long-time, high accuracy integrations. Any tendency of the integrator to become attracted to or repelled from stable equilibrium points will eventually manifest itself in the production of completely unphysical behavior. In this sense, the global stability properties of the SIAs make them well-suited to such numerical experiments.

The lower order Runge-Kutta algorithm (RKI2) often tended to become wildly unstable even after a relatively small number of integration steps. To illustrate this tendency, we have included a comparison of SIA2 (Figure F.1) and RKI2 (Figure F.2). Much of the of unstable behavior which we have noticed in the RKIs can be remedied by decreasing the size of δt . However, this only increases the length

of the time-scale of valid behavior, and ultimately comes at the expense of increased computational cost.

As a final example of the web equation, we solve numerically the system described by (2.46), with $s = 3$. The separatrix net of the averaged Hamiltonian is shown in Figure F.3, while the results obtained by SIA4 and RKI4 are shown in Figures F.4 and F.5 respectively. Once again, the structure of the intersection of resonant tori is defined more sharply by SIA4 than by RKI4. An attempt to apply the implicit method of Channell and Scovel [4], in a manner similar to that of Section 2.5b, resulted in divergence of the fixed-point iteration method used to solve for the integrated coordinate. However, in cases where this iteration did converge, the implicit method (ISIA4) showed the same stability properties as SIA4.

It has been mentioned by previous authors [4], [28]; that an SIA gives the exact evolution of a Hamiltonian system which is geometrically very similar to the true system. The degree of similarity is, of course, determined by the order and time step of the algorithm. Methods which are non-symplectic, however, replace the Hamiltonian system by one which is no longer Hamiltonian in nature. Consequently, after sufficiently long integration times, the numerical excitation or damping induced by such non-symplectic methods produces results which are completely uncharacteristic of the exact Hamiltonian system.

CHAPTER THREE
STOCHASTIC ION HEATING

3.1 A Model of Lower Hybrid Turbulence

Particle heating in the earth's ionosphere is believed to result from the interaction of ions with lower hybrid waves. (see [9] and [3]). In particular, precipitating electron beams in this region of the ionosphere might constitute a natural free energy source for the generation of lower hybrid waves. Unfortunately, the general problem of particle heating is enormously complicated, and it is no surprise that many aspects of these processes are still poorly understood. In what follows, we will investigate a single particle model of heating which is similar in form to, but slightly more general than the system (1.2). Further, we will examine the behavior of our model using physical parameters which are believed to be characteristic of a plasma containing such lower hybrid waves.

3.1a The Model Hamiltonian

To begin with, we consider a spectrum of N transversely propagating electrostatic waves. This case is a simple generalization of (1.2), with the electric field now described by the wave packet

$$E(x, t) = \sum_{i=1}^N E_i \sin(k_i x - \omega_i t + \varphi_i). \quad (3.1)$$

The Hamiltonian for a particle subject to this more general electric field can be written

$$\mathcal{H} = \frac{1}{2}(x^2 + p^2) + \sum_{i=1}^N \frac{\epsilon_i}{k_i} \cos(k_i x - \nu_i T + \varphi_i). \quad (3.2)$$

Note that we have introduced the dimensionless time $T \equiv \Omega t$ and the canonical momentum $p \equiv dx/dT = p_x/m\Omega$, so that \mathcal{H} has dimensions of (length)². The parameter ν_i is related to the temporal frequency ω_i of the i^{th} wave by the relationship

$$\nu_i \equiv \frac{\omega_i}{\Omega}.$$

Furthermore, for a plasma composed of singly ionized hydrogen, the nonlinearity parameter ϵ_i is defined in terms of the mode amplitude E_i according to

$$\epsilon_i \equiv \frac{eE_i}{m_p\Omega^2}. \quad (3.3)$$

Also, in each ν_i we have included an arbitrary phase factor φ_i which can be set to any value in the range $0 \leq \varphi_i < 2\pi$. In principle, all that remains is to choose reasonable values for the parameters ϵ_i , k_i , ν_i and Ω so that the equations of motion corresponding to (3.2) may be solved numerically.

3.1b Limiting the Parameter Space

At altitudes between 500 km and 2500 km the background magnetic field varies from about 4×10^{-5} Tesla to 2×10^{-5} Tesla. In general, we will assume that B assumes a constant value of 4×10^{-5} Tesla, so that

$$\Omega = 3.8318 \times 10^3 \text{ s}^{-1},$$

corresponding to a lower altitude field strength. Typical measured electric field amplitudes are on the order of 0.01 V/m [20]. Significantly higher amplitudes are indeed possible, and we consider (arguably high) maximum values on the order of 1 V/m for $E(x, t)$. This implies that the normalized maximum value of the field (see (3.3)) is

$$\frac{eE(x, t)}{m_p\Omega^2} \sim 10 \text{ m}.$$

(Actually, we will consider this to be an upper bound on the RMS value of the normalized field. This is discussed at length in Section 3.3). Such a restriction provides a rough guideline for choosing the set of nonlinearity parameters ϵ_i .

Next, to decide upon a reasonable value for each ν_i we must make use of the

dispersion relation for LH waves:

$$\omega = \omega_{pi} \left(1 + \frac{\omega_{pe}^2}{\omega_{ge}^2} \right)^{-1/2} \left(1 + \frac{m_p}{m_e} \sin^2 \theta \right)^{1/2}, \quad (3.4)$$

where

$$\omega_{pi}^2 = \frac{n_0 e^2}{\epsilon_0 m_p}, \quad \omega_{pe}^2 = \frac{n_0 e^2}{\epsilon_0 m_e}, \quad \omega_{ge}^2 = \frac{B^2 e^2}{m_e^2},$$

and $\tan \theta = k_z/k_x$. These expressions show the explicit dependence of ω on the local density n_0 .

The dispersion relation (3.4) is valid for small θ (i.e., $k_z \ll k_x$). Also, it is true that the Hamiltonian (3.2) – to a good approximation – describes the ion motion in the x - y plane even for small but nonzero k_x . Of course, the price of this simplification is to forego any detailed knowledge of the parallel motion. Fortunately, our concern here is with perpendicular acceleration only, so that this loss of information is of little concern. As a result, (3.2) affords us a valid picture of the perpendicular motion even beyond the $k_z = 0$ approximation.

Upon dividing (3.4) by Ω and squaring the result, one obtains

$$\left(\frac{\omega}{\Omega} \right)^2 = m_p \left(\frac{\epsilon_0 B^2}{n_0} + m_e \right)^{-1} \left(1 + \frac{m_p}{m_e} \sin^2 \theta \right). \quad (3.5)$$

In the region of the ionosphere we are interested in, realistic densities range from 10^8 m^{-3} to 10^{10} m^{-3} . Then, according to (3.5), the interval $0 \leq \theta \leq \pi/60$ corresponds to the following ranges in ω/Ω :

$$\begin{aligned} 3.4 \leq \frac{\omega}{\Omega} \leq 8.4 & \quad \text{for } n_0 = 10^8 \text{ m}^{-3}, \\ 26.8 \leq \frac{\omega}{\Omega} \leq 65.8 & \quad \text{for } n_0 = 10^{10} \text{ m}^{-3}. \end{aligned}$$

Using these limits as rough guidelines, we assume that ν_i may lie anywhere in the range

$$4 \leq \nu_i \leq 30.$$

It remains to find a physically reasonable value for each wavenumber k_i . Unfortunately, no physical measurements of the wavevectors of ionospheric lower hybrid waves have been obtained. It seems the best we can do is to consider possible driving sources of the waves, and derive a theoretical estimate. According to Koskinen [20], values of k_i on the order of 1 m^{-1} may be obtained by assuming that the LH waves are excited by a parallel beam of 4-keV electrons. Hence, we assume each k_i is restricted to the interval

$$0.1 \text{ m}^{-1} \leq k_i \leq 1.0 \text{ m}^{-1}.$$

3.1c Initial Conditions of Source Ions

Using the canonical variables we defined earlier, the ion gyroradius ρ , defined by

$$\rho^2 \equiv \frac{1}{\Omega^2} \left[\left(\frac{dx}{dt} \right)^2 + \left(\frac{dy}{dt} \right)^2 \right],$$

takes on the simple form

$$\rho = \sqrt{p^2 + x^2}. \quad (3.6)$$

To see this, one must realize that in the derivation of (1.1), p_y was chosen to have a constant initial value of zero, thus implying

$$p_y = m \frac{dy}{dt} + m\Omega x = 0.$$

The perpendicular kinetic energy (or temperature) \mathcal{T} of a test ion is, of course, related to the square of the gyroradius by

$$\mathcal{T} = \frac{m_p}{2e} (\Omega\rho)^2 \quad [\text{in eV}].$$

Typical ionospheric source ions have kinetic energies on the order of a fraction of an eV [9]. Let us assume that the ions we are considering have, in their

perpendicular degrees of freedom, kinetic energies between 0.25 eV and 1 eV. This range in energy corresponds corresponds to gyroradii in the interval

$$1.8 \text{ m} \leq \rho \leq 3.6 \text{ m} .$$

3.1d Method of Integration

To study the time evolution of p and x , we can generate a symplectic integration algorithm using the Hamiltonian function (3.2). Specifically, we will use the SIA4 algorithm derived in Chapter 2. With (3.2) written in the form $\mathcal{H} = \mathcal{H}_1(p) + \mathcal{H}_2(x, T)$, the SIA uses the functions

$$F(x, T) \equiv -\partial_x \mathcal{H}_2(x, T) = \sum_{i=1}^N \epsilon_i \sin(k_i x - \nu_i T + \varphi_i) - x$$

and

$$P(p) \equiv \partial_p \mathcal{H}_1(p) = p$$

to construct an explicit, analytic symplectic map. This symplectic map approximates the exact phase flow induced by \mathcal{H} , accurate to fourth order in the time step.

Using the SIA4 algorithm, we studied the time development of our model system for a variety of parameter values. A discussion of the results of this study appears below, with a separate section devoted to each particular simulation. Furthermore, a collection of figures which summarize the respective simulations appears in Appendices G and H, supplemented by captions which describe in full the associated parameter spaces.

The time steps δT used in SIA4 had the form

$$\delta T = \frac{\Delta T}{j}, \quad \text{where } \Delta T \equiv \frac{2\pi}{\bar{\nu}}. \quad (3.7)$$

In the above,

$$\bar{\nu} \equiv \{\text{the integer nearest to } \max(\nu_1, \dots, \nu_N)\},$$

and j is an arbitrary integer characterizing the smallness of the time step – and hence the accuracy of the symplectic integrator. Generally, j was chosen to lie between about 20 and 25; a size at which, loosely speaking, it is probably valid to forget about the original Hamiltonian and consider the system as described exactly by the symplectic map SIA4.

3.2 Heating with One Mode

3.2a Surfaces of Section

We begin by studying the time evolution of a system corresponding to the Hamiltonian (3.2) for the simplest case of $N = 1$. Figures G.1 and G.2 illustrate the structure of phase space for this case, with all parameters equal except for ν_1 . In particular, the first figure has $\nu_1 = 5$, while the second has $\nu_1 = 5.16$. In both cases, the wave amplitudes are relatively small, leaving much of the phase space covered by invariant tori. However, the two cases have clearly distinct topologies. In the first case, there exists a narrow channel of interconnected separatrices which form a web that spans the entire phase plane. This is in contrast to the picture in Figure G.2, which displays a series of nested tori as predicted by the KAM theorem. Interestingly, the violation of the KAM theorem in the first case, as a consequence of ν_1 being an integer, allows a theoretical diffusion along the stochastic network to arbitrarily large energies. However, the thickness of the web decreases rapidly with increasing velocity, so that diffusion is quite limited in practice.

Next, Figures G.3 and G.4 illustrate the effect of increasing the strength of

the electrostatic wave. By comparing Figure G.3 to Figure G.1, it becomes clear that the increase in wave amplitude produces a widening of the stochastic network, while in Figure G.4, one can see that it leads to a breakup of invariant tori. Finally, a characteristic common to all of these first four figures is the existence of a sequence of little tori enclosing the origin which effectively trap low energy particles. We will comment on the significance of such barriers in inhibiting particle acceleration later.

3.2b Ensemble Averaging

Next, we wish to examine the average phase space population $N(\rho)$ which results from accelerating an ensemble of low energy particles using the Hamiltonian (3.2). The steps taken to determine this quantity are described below:

- Assign 10 ions random positions in the phase space annulus $1.8 m \leq \rho \leq 3.6 m$ at $T = 0$.
- Integrate each particle in this ensemble forward in time to $T = 200\pi$.
- From $T = 200\pi$ to $T = 2000\pi$, record the position of each particle at successive time intervals $\Delta T = 2\pi/\bar{v}$ (see (3.7)).

Figures G.4 through G.9 illustrate this averaging procedure for fixed values of ν_1 , k_1 and φ_1 , but with successively increasing wave amplitude ϵ_1 . In the figures, $N(\rho)$ is expressed in arbitrary units. The local depletion of particles in each case corresponds to the presence of large first-order islands such as those in Figure G.1. In the limit of small wave amplitude, the elliptic fixed points exist at gyroradii ρ which satisfy

$$J'_{\nu_1}(k_1\rho) = 0.$$

As the wave amplitude grows to its maximum value, successive elliptic points are encircled, while the distributions around previous fixed points become smeared as invariant curves are destroyed.

The same simulation, with $\nu_1 = 5.16$, exhibits essentially no growth in energy. This can be seen in Figures G.10 and G.11, and results from the entire ensemble remaining trapped by invariant tori.

However, the situation changes if we double the wavevector k_1 to unity. Figure G.12 ($\nu_1 = 5$) and Figure G.13 ($\nu_1 = 5.16$) illustrate the results of a simulation which considered only one ion averaged over the period $T = 200\pi$ to $T = 6000\pi$, with ΔT defined as before. These results show comparable heating profiles for both values of ν_1 . The increased magnitude of k_1 effectively reduces the phase velocity of each wave and, in the case of noninteger ν_1 , destroys tori closer to the origin and allows stochastic diffusion of the test ion.

3.3 Amplitudes of Ordered and Turbulent Wave Spectra

We claimed in Section 3.1b that the normalized maximum value of the electric field should not exceed roughly 10 m. We did not, however, put particular restrictions on the normalized mode amplitudes ϵ_i . Clearly, the maximum possible amplitude of a wave packet composed of N sinusoidal modes, each with amplitude ϵ_i , is simply

$$\sum_{i=1}^N |\epsilon_i|. \quad (3.8)$$

However, in reality, one would expect that such an amplitude would rarely be attained – especially in the case where N is large.

Consider, first, the normalized electric field seen by the particle at time T :

$$\mathcal{E}(x(T), T) \equiv \frac{eE(x(T), T)}{m_p \Omega^2} = \sum_{i=1}^N \epsilon_i \sin(k_i x(T) - \nu_i T + \varphi_i). \quad (3.9)$$

The RMS value of this field, taken over time interval $[0, \tau]$, is defined as

$$\mathcal{E}_{rms}(\tau) \equiv \left[\frac{1}{\tau} \int_0^\tau \mathcal{E}^2(x(T), T) dT \right]^{1/2}. \quad (3.10)$$

In the limit $k_i \rightarrow 0$, and $\tau \rightarrow \infty$, it is simple to calculate \mathcal{E}_{rms} analytically. Calling this limiting value of the RMS field $\tilde{\mathcal{E}}_{rms}$, it is easy to show that

$$\tilde{\mathcal{E}}_{rms} = \left[\frac{1}{2} \sum_{i=1}^N \epsilon_i^2 \right]^{1/2}. \quad (3.11)$$

The validity of this result also requires that all ν_i are distinct.

We numerically computed $\mathcal{E}_{rms}(10\pi/\nu_{min})$ for two different wave packets, each with $N = 10$, and compared the results with the approximate value $\tilde{\mathcal{E}}_{rms}$. The first case, shown in Figure G.14, consists of waves evenly spaced in frequency with constant wavenumber and amplitude. The reader should recognize this spectrum as one which will give rise to a stochastic web. It happens that \mathcal{E}_{rms} for this ordered packet is 2.2 m – in close agreement with $\tilde{\mathcal{E}}_{rms} = \sqrt{5}$ m $\simeq 2.236$ m. It is interesting to note that as $N \rightarrow \infty$ in such a packet, the electric field seen by the particle approaches a periodic comb of delta functions, and is then described by the mapping of Zaslavsky, *et al.* [38]. In fact, such periodic impulses, or “kicks”, seem to be a generic aspect of chaos in Hamiltonian systems. Potential fields of this type give rise to many popular 2-D symplectic maps of the plane which are known to be chaotic – the *Standard* and *Fermi Maps*, for example. Furthermore, various approximate analyses of (1.2) ([23], for example) have concentrated on constructing a perturbed twist map of the plane which replaces the exact motion by: (i) a kick at $\dot{x} = \omega/k$, and (ii) unperturbed linear oscillation everywhere else, as shown in Figure H.16. In

a qualitative sense, it can be claimed that if the kick is strong enough, the particle will undergo a substantial phase change which will lead to stochastic motion. For this reason, it seems that the study of finite and infinite mode stochastic webs may be useful from the point of view of understanding the generic aspects of particle heating in the ionosphere.

In any case, we also calculated $\mathcal{E}_{rms}(10\pi/\nu_{min})$ for the turbulent spectrum shown in Figure G.15. While the structure of the field is much more erratic in this case than in the last, the value $\mathcal{E}_{rms} = 2.3$ m is quite comparable.

These calculations provides us with a rough estimate of the relationship between (3.8) and \mathcal{E}_{rms} , and serve to justify the values of ϵ_i used in the multiple mode simulations which follow.

3.4 Multiple Mode Stochastic Webs

As we mentioned in the last section, the study of finite mode stochastic webs may contribute to a better understanding of certain general properties of ionospheric particle heating. With this in mind, we choose to examine three particular cases, each for realistic values of the various wave parameters. Before doing so, we remind the reader of some fundamental ideas in nonlinear dynamics.

First, it has been shown that when the number of degrees of freedom satisfies $n \geq 3$, a separatrix net may arise which extends throughout phase space. This net, which was predicted by Arnold, forms a stochastic web along which particles may wander chaotically. The name given to this motion is *Arnold diffusion*, and results from the intersection of invariant tori which do not divide phase space (since $n \geq 3$). However, the Hamiltonian (3.2) represents only $n = 3/2$ degrees of freedom, thus

showing (see Figures H.1 to H.3) that an Arnold-type diffusion may occur even in the case of minimal dimension for nonintegrability.

3.4a Four Modes

Shown in Figure H.1 is the stochastic web which results from a wave packet composed of four modes. The frequencies are spaced according to $\nu_i = 5i$ for $i = 1, \dots, 4$; while the amplitudes and wavevectors are constant. Interestingly, the particle spent most of its time *sticking* nearby the tori centered at $\rho \sim 38$ m, and consequently the iterates were distributed very nonuniformly in phase space.

3.4b Five Modes

Next, we consider five modes with equal amplitude, and frequencies which are multiples of 5 – but not spaced as in the last example. In this case, we vary the wavenumber so that waves with equal values of ν_i will have different phase velocities. The effect of this modification is shown in Figure H.2. We see quite dramatic heating effects, with gyroradii approaching 110 m (or energies approaching 0.93 keV). This is achieved, however, with relatively low amplitude RMS fields (less than 0.5 V/m), and in the *absence* of what is normally considered to be global stochasticity (i.e., destruction of nearly all invariant tori).

3.4c Six Modes

As a final example of stochastic web heating, we add a sixth mode to the previous system. This has the effect, surprisingly, of limiting the maximum energy gain to only about 0.62 keV (see Figure 18). Unfortunately, the tendency of the iterates on

the surface of section to explore some areas of the separatrix mesh and not others is marked by a sensitive dependence on both initial conditions and the maximum integration time T_{max} . In instances of very large T_{max} , the areas of the web which are explored also depend on the time step used in SIA4 and on the precision of all floating point operations.

3.5 Heating by a Turbulent Spectrum

This final series of simulations is aimed at modeling particle heating in a “realistic” spectrum of waves. We consider $N = 10$ waves, each with normalized frequency ν_i , wavenumber k_i and phase φ_i chosen at random inside the intervals described in Section 3.1b. Then, we calculate the average population $N(\rho)$ according to the prescription in Section 3.2b for various cases characterized by different values of the ϵ_i . We performed 12 separate runs, which had the collective structure shown in Table H.1. For the 6 runs labeled by “A”, we chose the wave parameters

$$\left\{ \nu_i^{(A)}, k_i^{(A)}, \varphi_i^{(A)} \right\}_{i=1}^{10},$$

which remained constant for all values of the mode amplitudes. Then, for each A run, we chose a set of mode amplitudes (composed of 10 ϵ_i) at random in the interval $[\epsilon_{min}, \epsilon_{max}]$. For the runs labeled “B”, we generated new values for the wave parameters and the initial ion distribution, then performed the simulations with the same mode amplitudes as in the A runs. The maximum gyroradius ρ_{max} and corresponding temperature T_{max} to which the ions were accelerated also appear in Table H.1. The distributions $N(\rho)$ appear in Figures H.4 to H.15.

Each of these simulations was performed on a CRAY X-MP supercomputer, using single precision real variables (14 digit accuracy). The integrator time step was chosen with $j = 25$ (see (3.8)).

Perhaps the first difference which one notices in the heating profiles is the value of ρ_{max} in runs 1B, 2B and 3B; it is significantly lower than in the corresponding A runs. This can be explained, however, in terms of the minimum modal phase velocities. The slowest modes in the A and B runs respectively had normalized phase velocities of

$$\left\{ \frac{\nu_i^{(A)}}{k_i^{(A)}} \right\}_{min} \simeq 5.57 \text{ m} \quad \text{and} \quad \left\{ \frac{\nu_i^{(B)}}{k_i^{(B)}} \right\}_{min} \simeq 7.56 \text{ m}.$$

Now, for a particle to be effectively accelerated by a wave, it must be moving with a velocity *not* substantially less than the phase velocity of that wave. Otherwise, as seen in Figure H.16, no resonant interaction will occur. This effect is manifested in our simulation, where the faster moving B wave is less effective at providing the first jolts of acceleration than the slower A wave. This is one aspect of particle acceleration, however, that is greatly enhanced by the presence of a stochastic web. Because of the large first-order islands created by resonant particles which are initially located close to the origin in phase space ($\mathcal{T} < 1$ eV) may be swept out to substantially higher energies than would be possible otherwise. This is seen clearly in Figure G.1, where the separatrix mesh which surrounds the first-order islands reaches very close to the origin. This effect is not observed in Figure G.2, where the invariant tori divide the phase space into successive annulus-like regions.

Next, it happens that the maximum velocity to which a particle may be accelerated is also dependent upon the values of the modal phase velocities. To see this, note that in the A and B runs respectively, the maximum normalized phase velocities were

$$\left\{ \frac{\nu_i^{(A)}}{k_i^{(A)}} \right\}_{max} \simeq 92.2 \text{ m} \quad \text{and} \quad \left\{ \frac{\nu_i^{(B)}}{k_i^{(B)}} \right\}_{max} \simeq 67.2 \text{ m}.$$

The larger phase velocity in case A allows stochastic diffusion to occur at correspondingly larger gyroradii. As a result, for the maximum electric field amplitudes

in runs 5A and 6B, case A exhibits superior particle heating characteristics.

If lower hybrid waves are indeed responsible for the bulk heating of ions in the ionosphere, we hope that the simulations described herein might help elucidate some of details of the wave-particle interactions involved. Indeed, by studying this simple single particle model, we can gain a better understanding of the characteristics and limitations of LH heating.

Unfortunately, as was mentioned earlier on, the processes which we have tried to model in this chapter are still quite poorly understood. Further, lower hybrid heating is by no means the only possible mechanism for ion acceleration in the suprathermal region. While the upper limit of $T_{max} \sim 1$ keV (at RMS fields of roughly 1.2 V/m) is of the same order of magnitude as temperatures of observed hot ions populations, more experimental data is needed before researchers are able to construct a truly reliable picture of these ionospheric processes.

3.6 The Disappearance of Landau Damping

Recall that one may define the *dielectric response function* $\epsilon(\mathbf{k}, \omega)$ of a plasma in terms of the dielectric tensor $\epsilon(\mathbf{k}, \omega)$ according to

$$\epsilon(\mathbf{k}, \omega) \equiv \frac{\mathbf{k} \cdot \epsilon(\mathbf{k}, \omega) \cdot \mathbf{k}}{k^2}. \quad (3.12)$$

For a plasma in a uniform, external magnetic field such as that pertaining to (2.1), we can write this response as a sum over all ion species σ according to [16]

$$\epsilon(\mathbf{k}, \omega) = 1 - \sum_{\sigma} \sum_{n=-\infty}^{\infty} \int d^3v \frac{F_{\sigma,n}(\mathbf{v})}{n\Omega_{\sigma} + k_z v_z - \omega - i\eta}. \quad (3.13)$$

The explicit form of $F_{\sigma,n}(\mathbf{v})$, which is not important for our purposes, is determined by the single-particle velocity distribution function $f_{\sigma}(\mathbf{v})$. When the wave propagates obliquely to the magnetic field, the contributions to the response occur at

3.6 The Disappearance of Landau Damping 38

values of v_z where the denominator in the integral vanishes. These resonances, of course, are the sources of *linear Landau damping* of the plasma wave. However, if we let the wave propagate transversely to the magnetic field as in (1.2), then the new set of resonances $\omega = n\Omega_e$ are independent of v – and the Landau damping vanishes. This phenomenon has been examined closely in [23] and [37], where it is shown that the paradoxical disappearance of Landau damping is accompanied by the emergence of a particular form of nonlinear damping. This new damping is related to the stochastic instability of particle motion. In particular, stochastic web formation is one example of this phenomenon.

CHAPTER FOUR

PERTURBATIVE ANALYSIS

4.1 The Wave Driven Linear Oscillator

The Hamiltonian for a linear oscillator perturbed by a plane wave,

$$H(x, p, t) = \frac{1}{2} (x^2 + p^2) + \epsilon \cos(x - \nu t), \quad (4.1)$$

has been seriously studied by a number of authors. In particular, the recent works of Chernikov, *et. al.* [5,6] have examined the development of *Stochastic Webs* in phase space for the Hamiltonian (4.1). These interesting structures occur when the system is strongly degenerate – that is, when $\nu \in \mathbb{Z}$. In an earlier paper by Karney [19], a theoretical estimate of the global stochasticity threshold was established for arbitrary ν . It is the intent of this chapter¹ to study the hierarchy of resonances which occur in the system described by (4.1) when $\nu = r/s$, such that r and s are relatively prime positive integers [33].

Our perturbative approach will be facilitated by the introduction of the unperturbed action and angle variables (P_ϕ, ϕ) according to

$$\begin{aligned} x &= \rho \sin \phi, \\ p &= \rho \cos \phi, \end{aligned}$$

where $\rho \equiv \sqrt{2P_\phi}$. This canonical change of variables, along with a Fourier decomposition of the perturbation, transforms the Hamiltonian (4.1) into the standard

¹This chapter has been submitted for publication in manuscript form to *Physica D*.

form

$$H(\phi, P_\phi, t) = P_\phi + \epsilon \sum_{m=-\infty}^{\infty} J_m(\rho) \cos(m\phi - \nu t), \quad (4.2)$$

where $J_m(\rho)$ is a Bessel function of order m .

4.2 Deprit Perturbation Series

The formalism which we use to obtain perturbative solutions to (4.2) is based on the construction of a Lie transform ordered in the parameter ϵ . This method was developed by Deprit [10], and is summarized clearly in a report by Cary [2]. As noted in [2], the explicit nature of this transformation theory makes it much more efficient than the traditional Poincaré-Von Zeipel perturbation theory. A brief summary of the general Lie method is presented below.

First, let us restrict our attention to the class of Hamiltonian functions which can be expanded as a power series in some small parameter according to

$$H(z, t, \epsilon) = \sum_{n=0}^{\infty} \epsilon^n H_n(z, t), \quad (4.3)$$

such that the zero order function $H_0(z, t)$ is exactly solvable. As usual, we define $z \equiv (x_1, \dots, x_N; p_1, \dots, p_N) \in \mathbb{R}^N \times \mathbb{R}^N$ to be the usual composite vector of coordinates and momenta. The theory then gives us a prescription for calculating a new Hamiltonian $\bar{H}(z, t, \epsilon)$, and a transformation operator $\hat{T}(t, \epsilon)$ with similar expansions:

$$\bar{H}(z, t, \epsilon) = \sum_{n=0}^{\infty} \epsilon^n \bar{H}_n(z, t), \quad (4.4)$$

$$\hat{T}(t, \epsilon) = \sum_{n=0}^{\infty} \epsilon^n \hat{T}_n(t). \quad (4.5)$$

Operationally, the variables z are dummy variables; for example, the new Hamiltonian \bar{H} is properly a function of some new set of variables $\bar{z}(z, t)$ which directly

replace the dummy variables z . Moreover, the transformation operator \hat{T} and its inverse act on functions according to

$$f(\bar{z}(z, t, \epsilon)) = \hat{T}f(z), \quad (4.6)$$

$$f(z(\bar{z}, t, \epsilon)) = \hat{T}^{-1}f(\bar{z}), \quad (4.7)$$

thus revealing the explicit relationship between old and new variables. The operator \hat{T} is defined using the components $w_n(z, t)$ of the Lie generating function

$$w(z, t, \epsilon) = \sum_{n=0}^{\infty} \epsilon^n w_{n+1}(z, t), \quad (4.8)$$

according to the recursive formula

$$\hat{T}_0 = I \quad \text{and} \quad \hat{T}_n = -\frac{1}{n} \sum_{m=0}^{n-1} \hat{T}_m : w_{n-m} : . \quad (4.9)$$

Similarly, the inverse transformation operator \hat{T}^{-1} satisfies

$$\hat{T}_0^{-1} = I \quad \text{and} \quad \hat{T}_n^{-1} = \frac{1}{n} \sum_{m=0}^{n-1} : w_{n-m} : \hat{T}_m^{-1} . \quad (4.10)$$

Throughout this paper, we shall use $: f(z, t) :$ to denote the *Lie operator* associated with the function $f(z, t)$. This notation is due to Dragt [11], and is defined in terms of Poisson brackets according to

$$: f : g \equiv [f, g] = \sum_{i=1}^N \left\{ \frac{\partial f}{\partial x_i} \frac{\partial g}{\partial p_i} - \frac{\partial f}{\partial p_i} \frac{\partial g}{\partial x_i} \right\} . \quad (4.11)$$

As expected, the transformation operators reduce to the identity when $\epsilon = 0$. For this reason, we also require that $\bar{H}_0 = H_0$. As can be inferred from (4.9) and (4.10), the first order components of the transformation operators are

$$\hat{T}_1 = - : w_1 : \quad \text{and} \quad \hat{T}_1^{-1} = : w_1 : ,$$

and the second order components are

$$\hat{T}_2 = \frac{: w_1 :^2 - : w_2 :}{2} \quad \text{and} \quad \hat{T}_2^{-1} = \frac{: w_1 :^2 + : w_2 :}{2} .$$

Finally, to obtain each component w_n of the generator w , we must solve the differential equation

$$\frac{\partial w_n}{\partial t} + :w_n : H_0 = n (\bar{H}_n - H_n) - \sum_{m=1}^{n-1} (:w_{n-m} : \bar{H}_m + m \hat{T}_{n-m}^{-1} H_m) \quad (4.12)$$

by choosing \bar{H}_n at each order to remove any secularity or intrinsic resonance. The rules for choosing \bar{H}_n at each order will be made clear later.

4.3 Calculation of w_1

The general form of equation (4.12) when $n = 1$ is

$$\frac{\partial w_1}{\partial t} + :w_1 : H_0 = \bar{H}_1 - H_1. \quad (4.13)$$

Substituting H_1 from (4.2) into (4.13) yields

$$\frac{\partial w_1}{\partial t} + \frac{\partial w_1}{\partial \phi} = \bar{H}_1 - \sum_m J_m(\rho) \cos(m\phi - \nu t). \quad (4.14)$$

Case 1: $s > 1$

If $s > 1$, so that the wave frequency $\nu = r/s$ is not an integer, it happens that the time average of the sum in (4.14) is zero. Accordingly, we may choose \bar{H}_1 to be zero as well. This choice leads to the solution

$$w_1 = \sum_m J_m(\rho) \frac{\sin(m\phi - \nu t)}{\nu - m}. \quad (4.15)$$

To first order, the new Hamiltonian is simply the zero-order component of the old Hamiltonian, now properly expressed in terms of the new action:

$$\bar{H} = \bar{P}_\phi. \quad (4.16)$$

Then, by acting on P_ϕ with the operator \hat{T} , we see that the new action can be written as

$$\bar{P}_\phi = P_\phi - \epsilon \sum_m m J_m(\rho) \frac{\cos(m\phi - \nu t)}{\nu - m} \quad (4.17)$$

(equation (11) of reference [26], which is analogous to the above equation (4.17), erroneously shows the addition of the sum to the momentum P_ϕ).

An expression for $\bar{\phi}$ may be obtained in an analogous fashion. It is worth mentioning that one may also find the inverse transformation (i.e., the old variables as functions of the new ones) by applying the operator \hat{T}^{-1} .

Case 2: $s = 1$

When $s = 1$, so that ν is an integer, we must choose \bar{H}_1 to remove the resonant term $m = \nu$ from the sum in (4.14). Doing so yields the solution

$$w_1 = \sum_{m \neq \nu} J_m(\rho) \frac{\sin(m\phi - \nu t)}{\nu - m}, \quad (4.18)$$

where it should be understood that the sum is over all m not equal to ν . Thus, we are left with the new Hamiltonian

$$\bar{H} = \bar{P}_\phi + \epsilon J_\nu(\bar{\rho}) \cos(\nu\bar{\phi} - \nu t), \quad (4.19)$$

where $\bar{\rho} \equiv \sqrt{2\bar{P}_\phi}$. At this point we mention that the singularity which would have occurred in (4.15) for $m = \nu$ represents an *intrinsic* [22] resonance in the system. By this, we mean that the resonant denominator $(\nu - m)$ does not depend on the action. Cases for which the singularity depends on the action represent an *accidental* resonance, and are discussed in detail by McNamara [24].

The Hamiltonian (4.19) can be used to construct an invariant function S_ν on the surface of section $t = 0 \pmod{2\pi/\nu}$. Using the type 2 generating function

$F_2 = \tilde{P}_\phi(\bar{\phi} - t)$, we transform to the new variables

$$\begin{aligned}\tilde{P}_\phi &= \bar{P}_\phi, \\ \tilde{\phi} &= \bar{\phi} - t.\end{aligned}$$

Changing to these new variables leaves us with the time-independent Hamiltonian

$$\tilde{H} = \epsilon J_\nu(\sqrt{2\tilde{P}_\phi}) \cos(\nu\tilde{\phi}),$$

which has been identified in [5] as the stationary (or averaged) part of the Hamiltonian (4.2). Thus, to zeroth order in ϵ , the function

$$S_\nu^{(1)} = J_\nu(\rho) \cos(\nu\phi) \tag{4.20}$$

is invariant on the surface of section. In obtaining this result, we have made use of the near-identity relationship between the old and new variables. The invariant (4.20) is independent of the perturbation strength ϵ (taken to be non-zero). This is in contrast to the ϵ -dependent form of the invariant action (4.17) which is valid if $\nu \neq \mathbb{Z}$. Figure I.1 shows some arbitrary level contours of the invariant (4.20) in the (x, p) phase plane for $\nu = 3$.

Also, we numerically integrated (4.1) using the fourth-order symplectic integration algorithm as described in Chapter 2. This algorithm simply replaces exact Hamiltonian system with an explicit symplectic map which is topologically close to the original system. The results are shown in Figure I.2, and compare well with invariant surfaces predicted by (4.20) (Figure I.1).

In the sections that follow, we restrict our interest to situations for which $s > 1$ (so that w_1 is correctly given by (4.15)).

4.4 Calculation of w_2

When $n = 2$, equation (4.12) can be written

$$\frac{\partial w_2}{\partial t} + :w_2 : H_0 = 2\bar{H}_2 - :w_1 : (\bar{H}_1 + H_1). \quad (4.21)$$

Upon substitution of (4.15) into (4.21) (with $\bar{H}_1 = 0$), the equation determining w_2 becomes

$$\frac{\partial w_2}{\partial t} + \frac{\partial w_2}{\partial \phi} = 2\bar{H}_2 - \sum_m \sum_n \Gamma_{mn}, \quad (4.22)$$

where

$$\Gamma_{mn} = J_m(\rho) \dot{J}_n(\rho) \left\{ \frac{\sin(m\phi - \nu t) \sin(n\phi - \nu t)}{\nu - n} + \frac{\cos(m\phi - \nu t) \cos(n\phi - \nu t)}{\nu - m} \right\}.$$

Note that a dot is used here to denote a derivative with respect to P_ϕ . An expansion of the trigonometric products in Γ_{mn} yields

$$\Gamma_{mn} = \frac{m J_m(\rho) \dot{J}_n(\rho)}{(\nu - m)(\nu - n)} \left\{ \left[\nu - \frac{m+n}{2} \right] \cos[(n-m)\phi] + \frac{m-n}{2} \cos[(m+n)\phi - 2\nu t] \right\}.$$

Case 1: $s > 2$

If $s > 2$, we need only remove the secularity which would arise from the Γ_{mm} terms in (4.22). This can be accomplished by choosing

$$2\bar{H}_2 = \sum_m \Gamma_{mm} = \sum_m \frac{m J_m(\rho) \dot{J}_m(\rho)}{\nu - m}, \quad (4.23)$$

in which case (4.22) becomes

$$\frac{\partial w_2}{\partial t} + \frac{\partial w_2}{\partial \phi} = - \sum_{\substack{m \\ m \neq n}} \sum_n \Gamma_{mn}. \quad (4.24)$$

Hence, the second order component of the Lie generating function is

$$w_2 = \sum_m \sum_{\substack{n \\ m \neq n}} J_m(\rho) \dot{J}_n(\rho) \{A_{mn} \sin[(m-n)\phi] + B_{mn} \sin[(m+n)\phi - 2\nu t]\}, \quad (4.25)$$

where the coefficients A_{mn} and B_{mn} have the form

$$A_{mn} = \frac{m[2\nu - (m+n)]}{2(n-m)(\nu-m)(\nu-n)} \quad \text{and} \quad B_{mn} = \frac{m(m-n)}{2[2\nu - (m+n)](\nu-m)(\nu-n)}.$$

So, correct to $O(\epsilon^2)$, the new Hamiltonian is

$$\bar{H} = \bar{P}_\phi + \frac{\epsilon^2}{4} \frac{d}{d\bar{P}_\phi} \sum_m \frac{m J_m^2(\bar{\rho})}{\nu - m}. \quad (4.26)$$

As a point of interest, we note that the corresponding equations of motion are

$$\begin{aligned} \frac{d\bar{P}_\phi}{dt} &= 0, \\ \frac{d\bar{\phi}}{dt} &= 1 + \frac{\epsilon^2}{4} \frac{d^2}{d\bar{P}_\phi^2} \sum_m \frac{m J_m^2(\bar{\rho})}{\nu - m}, \end{aligned}$$

the latter of which is a result previously obtained by Karney [19].

Case 2: $s = 2$

Now, when $s = 2$, there are additional terms in (4.22) which must be removed to avoid a divergence in the solution for w_2 . Indeed, all terms Γ_{mn} for which $m+n = 2\nu$ must be cancelled by the component \bar{H}_2 of the new Hamiltonian. This consideration leads to

$$2\bar{H}_2 = \sum_m \frac{m J_m(\rho) \dot{J}_m(\rho)}{\nu - m} + \sum_m \sum_{\substack{n \\ m+n=2\nu}} \frac{m(m-n) J_m(\rho) \dot{J}_n(\rho)}{2(\nu-m)(\nu-n)} \cos[(m+n)\phi - 2\nu t]. \quad (4.27)$$

Upon simplification of this expression, we can write the new Hamiltonian as

$$\bar{H} = \bar{P}_\phi + \frac{\epsilon^2}{2} \left\{ \sum_m \frac{m J_m(\bar{\rho}) \dot{J}_m(\bar{\rho})}{\nu - m} + \cos[2\nu(\bar{\phi} - t)] \sum_m \frac{m J_m(\bar{\rho}) \dot{J}_{2\nu-m}(\bar{\rho})}{\nu - m} \right\}. \quad (4.28)$$

By making the same canonical transformation as in Case 2 of Section 4.3, it follows that when $\nu = r/2$, the function

$$S_\nu^{(2)} = F_\nu(\rho) + \cos(2\nu\phi)G_\nu(\rho), \quad (4.29)$$

where

$$F_\nu(\rho) \equiv \sum_m \frac{m J_m(\rho) \dot{J}_m(\rho)}{\nu - m} \quad \text{and} \quad G_\nu(\rho) \equiv \sum_m \frac{m J_m(\rho) \dot{J}_{2\nu-m}(\rho)}{\nu - m},$$

is invariant on the surface of section $t = 0 \pmod{2\pi/\nu}$. Notice that the resonant invariant $S_\nu^{(2)}$, like $S_\nu^{(1)}$, is independent of the perturbation strength. This interesting property, though, exists only for $s \leq 2$, as a result of the secular term (4.23). In Appendices C and D, the series defining F_ν and G_ν are summed analytically.

Level contours of the invariant (4.29) are shown in Figure I.3, and agree well with the numerically calculated trajectories which appear in Figure I.4. These figures show that even for arbitrarily small values of ϵ , the $s = 2$ resonant tori occupy most all of the phase volume. However, as one can see from Figure I.3, the phase space topology which occurs in the $s = 2$ case is fundamentally different from that which is associated with the stochastic web ($s = 1$). When $s = 2$, the resonant tori are divided into annular groups by larger nonresonant tori - thus allowing stochastic diffusion to occur only within localized regions along a separatrix layer (see Figure I.5). Of course, for large values of ϵ , a complete breakdown of these structures will occur, followed by the onset of global stochasticity. This effect is illustrated in Figure I.6.

4.5 Higher-Order Invariants

The analysis of the previous sections may be extended, in principle, to any order. However, the amount of algebra needed to calculate w_n explicitly as n increases beyond 2 or 3 becomes prohibitively large. Furthermore, the usefulness of these results for higher orders is questionable. In any case, we are still able to comment on the general form which the transformed Hamiltonian takes in the higher orders.

Secularity

At each *even* order, terms must be removed from the right hand side of (4.12) to avoid secularity. This implies that the transformed (averaged) Hamiltonian for irrational ν must reduce to

$$\bar{H} = \bar{P}_\phi + \sum_{m=1}^{[n/2]} \epsilon^{2m} \bar{H}_{2m}(\bar{P}_\phi), \quad (4.30)$$

where n is the order to which the perturbation theory is computed (and $[n/2]$ is the greatest integer less than or equal to $n/2$). As $\epsilon \rightarrow 0$, the behavior of this general Hamiltonian uniformly approaches that of its unperturbed counterpart. That is to say, for arbitrarily small ϵ and irrational ν , the structure of phase space is topologically the same as in the unperturbed case.

Resonance

It can be shown inductively that for even n , the equation for w_n contains angle dependent functions of the form

$$\cos(m\phi), \cos(m\phi - 2\nu t), \dots, \cos(m\phi - n\nu t),$$

where m is an arbitrary integer. The first term in this sequence (for $m = 0$) is the secular term mentioned in the previous discussion. Similarly, for odd n , the equation for w_n contains

$$\cos(m\phi - \nu t), \cos(m\phi - 3\nu t), \dots, \cos(m\phi - n\nu t).$$

Clearly, if $\nu = r/n$, an angle dependent resonance of the form

$$f_\nu(\bar{P}_\phi) \cos[n\nu(\bar{\phi} - t)] \tag{4.31}$$

must be added to the Hamiltonian (4.39). It appears, however, that as n increases, the size of the resonant islands rapidly decreases. This leads to the resonant tori becoming strongly “sandwiched” between the larger nonresonant tori, as illustrated in the numerically computed Poincaré maps shown in Figures I.7 and I.8.

4.6 Implications

In recent years, several authors [38] have studied the stochastic dynamics of a linear oscillator forced by a temporally periodic sequence of delta-functions (or, equivalently, by an infinite number of electrostatic waves evenly spaced in frequency). The Hamiltonian difference equations describing this system lead to the tiling of phase space by a global web structure with complex symmetry properties. However, as this is often not a physically viable wave-particle interaction model, the motion of particles in the field of a finite number of electrostatic waves has also been investigated in [26] and [32]. It has been shown in these cases that a web-like separatrix mesh does exist, but with a thickness that rapidly decreases with increasing distance from the origin in phase space. Similarly, a single electrostatic wave with frequency $\nu \in \mathbb{Z}$ (cf. Figures I.1 and I.2) also leads to the development of a stochastic web. In all these situations, the topology of phase space is drastically different than that found in weakly perturbed linear oscillations. Furthermore, the shape of the separatrix mesh is, to lowest order, independent of the wave amplitude. The global character of such a web, however, may have little practical importance for particle heating and diffusion in the limit of small wave amplitudes – since the stochastic mesh narrows very rapidly. Consequently, in our examples (Figure I.2), particles will experience only a local diffusion, remaining close to the origin in phase space.

Generally speaking, the Hamiltonian function (4.1) is a dynamical model of a particle moving in the field of an electrostatic wave which propagates perpendicularly to a constant magnetic field. Of course, such a model has many applications in plasma physics. It is also related to the well-known paradox of the disappearance of Landau damping [29], [37]. For perpendicular wave propagation, the resonance $\delta(\omega - kv)$ responsible for linear Landau damping is replaced by the set of discrete

resonances $\delta(\omega - n\omega_H)$, where ω_H is the particle gyrofrequency. This paradox has been resolved in the aforementioned references by introducing particle trapping effects. Studies of resonant cases, for which $\omega = n\omega_H$ (or $\nu = n$ in our normalized variables), have indicated fundamental problems with linear theory based on regular particle trajectories. One of the results of this work is to show that the web-like structures which arise for $\omega/\omega_H = r/2$ (and persist in the limit of vanishingly small wave amplitude) may lead to similar problems in the linearized Vlasov theory.

CHAPTER FIVE

CONCLUSION

In Chapter 2, we generalized the method of Ruth [28] to obtain an SIA accurate to 4th order in the time-step (SIA4). This algorithm was tested using several numerical examples, including the nonlinear pendulum, the motion of a charged particle in a standing wave, and a harmonic oscillator perturbed by a plane wave. This testing indicated that SIA4 is computationally more efficient than both the classical Runge-Kutta method of order 4 (RKI4) and the implicit method given in [4]. Also, SIA4 was found to be inherently more stable than RKI4 during long-time integrations.

Using the algorithm derived in Chapter 2, we turned in Chapter 3 to the study of lower hybrid heating. If lower hybrid waves are indeed responsible for the bulk heating of ions in the ionosphere, we hope that the simulations which were performed might help elucidate some of details of the wave-particle interactions involved. Indeed, by studying this simple single particle model, we can gain a better understanding of the characteristics and limitations of LH heating.

Unfortunately, as was mentioned earlier on, the processes which we have tried to model in Chapter 3 are still quite poorly understood. Further, lower hybrid heating is by no means the only possible mechanism for ion acceleration in the suprathermal region. While the upper limit of $T_{max} \sim 1$ keV (at RMS fields of roughly 1.2 V/m) is of the same order of magnitude as temperatures of observed hot ions populations, more experimental data is needed before researchers are able to construct a truly reliable picture of these ionospheric processes.

Finally a perturbative analysis of the single wave model studied in Chapter 3

indicated that rational wave frequencies $\nu = r/s$ give rise to intrinsic resonances. Furthermore, it was found that the prominence of these resonances diminishes as s increases.

BIBLIOGRAPHY

- [1] V. I. Arnold, *Mathematical Methods of Classical Mechanics* (Springer-Verlag, New York, Second Ed. 1989), pp. 201.
- [2] J. R. Cary, *Phys. Reports* **79** (1981) 129.
- [3] T. Chang, G. B. Crew and J. M. Retterer, *Computer Physics Communications* **49** (1988) 61.
- [4] P. J. Channell and C. Scovel, preprint, Los Alamos National Laboratory, LA-UR-88-1828 (1988)
- [5] A. A. Chernikov, M. Ya. Natenzon, B. A. Petrovichev, R. Z. Sagdeev and G. M. Zaslavsky, *Phys. Lett.* **122A** (1987) 39. *Proceedings No. 87* (1981) 147.
- [6] A. A. Chernikov, R. Z. Sagdeev and G. M. Zaslavsky, *Physica D* **33** (1988) 65.
- [7] A. A. Chernikov, R. Z. Sagdeev, D. A. Usikov, M. Yu. Zakharov and G.M. Zaslavsky, *Nature* **326** (1989) 559.
- [8] B. V. Chirikov, *Phys. Rep.* **52** (1979) 265.
- [9] G B. Crew and T. Chang, in: *Physics of Space Plasmas (1985-87)*, eds. T. Chang, J. Belcher, J. R. Jasperse and G. B. Crew, *SPI Conf. Proc. and Reprint Series*, vol. 6 (Scientific Publishers, Cambridge, MA, 1987) p. 55.
- [10] A. Deprit, *Cel. Mech.* **1** (1969) 2043.
- [11] A. J. Dragt, Fermilab Summer School, AIP Conference
- [12] N. N. Filonenko, R. Z. Sagdeev and G. M. Zaslavsky, *Nuclear Fusion* **7** (1967) 253.

- [13] E. Forest and R. D. Ruth, *Physica D*, to be published.
- [14] A. Fukuyama, H. Momota, R. Itatani and T. Takizuka, *Phys. Rev. Lett.* **38** (1977) 701.
- [15] I. S. Gradshteyn and I. M. Ryzhik, *Table of Integrals, Series, and Products*, (Academic Press, Florida, Fourth Ed. 1980), pp. 40, 739.
- [16] S. Ichimaru, *Basic Principles of Plasma Physics*, (Benjamin/Cummings, Reading, Mass. 1973) pp. 51-59.
- [17] T. Itoh and K. Abe, *J. Comp. Phys.* **77** (1988) 85.
- [18] H. Karimabadi and V. Angelopoulos, *Phys. Rev. Lett.* **62** (1989) 2342.
- [19] C. F. F. Karney, *Phys. Fluids* **21** (1978) 1584; **22** (1979) 2188.
- [20] H. E. Koskinen, *J. Geophys. Res.*, **90** (1985) 8361.
- [21] A. J. Lichtenberg, in: *Stochastic Behavior in Classical and Quantum Hamiltonian Systems*, G. Casati and J. Ford, eds. (Springer-Verlag, New York, 1979).
- [22] A. J. Lichtenberg and B. P. Wood, *Phys. Rev.* **39**, (1989) 2153.
- [23] M. A. Malkov and G. M. Zaslavsky, *Phys. Lett.* **106A** (1984) 257.
- [24] B. McNamara, *J. Math Phys.* **19** (1978) 2154.
- [25] W. E. Milne, *Numerical Solution of Differential Equations*, (Dover Publications Inc., New York, Second Ed. 1970), pp. 72.
- [26] S. Murakami, T. Sato and A. Hasegawa, *Physica D* **32** (1988) 259.
- [27] A. Ralston, *A First Course in Numerical Analysis*, (McGraw-Hill Inc., New York, 1965), pp. 200.

- [28] R. D. Ruth, IEEE Trans. Nucl. Sci., NS-30 (1983) 2669.
- [29] R. Z. Sagdeev and V. D. Shapiro, JETP Lett. 17 (1973) 279.
- [30] J. A. Sanders and F. Verhulst, Averaging Methods in Nonlinear Dynamical Systems, (Springer-Verlag, New York, 1985), pp. 119.
- [31] G. Schmidt, Comments Plasma Phys. Controlled Fusion 7 (1982) 87.
- [32] G. Schmidt, Comments Plasma Phys. Controlled Fusion 13 (1989) 77.
- [33] H. N. Shapiro, *Introduction to the Theory of Numbers*, (John Wiley and Sons, New York, 1983) pp. 13.
- [34] G. R. Smith and A. N. Kaufman, Phys. Rev. Lett. 34 (1975) 1613.
- [35] G. R. Smith and A. N. Kaufman, Phys. Fluids 21 (1978) 2230.
- [36] G. N. Watson, *A Treatise on the Theory of Bessel Functions*, (Cambridge University Press, London, Second Ed. 1966), pp. 30, 32, 150.
- [37] G. M. Zaslavsky, M. A. Malkov, R. Z. Sagdeev and V. D. Shapiro, Sov. J. Plasma Phys. 12(7) (1986) 453.
- [38] G. M. Zaslavsky, M. Yu. Zakharov, R. Z. Sagdeev, D. A. Usikov and A. A. Chernikov, Sov. Phys. JETP 64(2) (1986) 294.

APPENDIX A

RKI2 AND RKI4 ALGORITHMS

The two Runge-Kutta methods which are used to numerically integrate the vector differential equation

$$\frac{dx}{dt} = f(x, t)$$

from the initial conditions x_0 at time $t = t_0$ to the coordinates x at time $t = t_0 + \delta t$ are RKI2:

$$x = x_0 + f\left(x_0 + \frac{\delta t}{2}f(x_0, t_0), t_0 + \frac{\delta t}{2}\right)\delta t$$

and RKI4:

$$x = \frac{1}{6}(k_1 + 2k_2 + 2k_3 + k_4)$$

$$k_1 = f(x_0, t_0)\delta t$$

$$k_2 = f\left(x_0 + \frac{k_1}{2}, t_0 + \frac{\delta t}{2}\right)\delta t$$

$$k_3 = f\left(x_0 + \frac{k_2}{2}, t_0 + \frac{\delta t}{2}\right)\delta t$$

$$k_4 = f(x_0 + k_3, t_0 + \delta t)\delta t.$$

APPENDIX B

ISIA4 ALGORITHM

The ISIA4 algorithm, shown below, for the Hamiltonian (43) is derived according to the procedure in [4]. It is accurate to 4th order in the time step. Here, (q_0, p_0) are the initial conditions at time $t = t_0$, and (q, p) are the integrated variables at time $t = t_0 + \delta t$. Note that the first equation,

$$q = q_0 + p_0 \delta t - \frac{\delta t^2}{2} (\epsilon \sin q \cos t) + \frac{\delta t^3}{3} (\epsilon p_0 \cos q \cos t - \epsilon \sin q \sin t) + \frac{\delta t^4}{24} [6\epsilon p_0 \cos q \sin t + 3\epsilon(p_0^2 + 1) \sin q \cos t - 5\epsilon^2 \sin q \cos q \cos^2 t],$$

is implicit for q , while the second,

$$p = p_0 - \delta t (\epsilon \sin q \cos t) + \frac{\delta t^2}{2} (\epsilon p_0 \cos q \cos t - \epsilon \sin q \sin t) + \frac{\delta t^3}{6} [2\epsilon p_0 \cos q \sin t + \epsilon(p_0^2 + 1) \sin q \cos t - 2\epsilon^2 \sin q \cos q \cos^2 t] + \frac{\delta t^4}{24} [5\epsilon^2 p_0 \cos^2 t (\cos^2 q - \sin^2 q) + \epsilon(3p_0^2 + 1) \sin q \sin t - \epsilon p_0(p_0^2 + 3) \cos q \cos t - 10\epsilon^2 \sin q \cos q \sin t \cos t]$$

is explicit for p .

APPENDIX C

THE FUNCTION F_ν

The function F_ν , which appears as the first term on the right hand side of the invariant (29), can be expressed completely as a function of ρ according to

$$F_\nu(\rho) = \frac{1}{2\rho} \frac{d}{d\rho} \sum_{m=-\infty}^{\infty} \frac{m J_m^2(\rho)}{\nu - m}, \quad (\text{C.1})$$

Rewriting this as a sum over positive integers gives

$$F_\nu(\rho) = \frac{1}{2\rho} \frac{d}{d\rho} \left\{ J_0^2(\rho) + 2\nu^2 \sum_{m=1}^{\infty} \frac{J_m^2(\rho)}{\nu^2 - m^2} \right\}.$$

Then, using the Bessel function identity [36]

$$J_m^2(\rho) = \frac{1}{\pi} \int_0^\pi J_0(2\rho \sin \psi) \cos(2m\psi) d\psi, \quad (\text{C.2})$$

together with the result [15] (valid for $\psi \in [0, \pi]$)

$$\sum_{m=1}^{\infty} \frac{\cos(2m\psi)}{\nu^2 - m^2} = -\frac{1}{2\nu^2} + \frac{\pi}{2\nu} \sin(2\nu\psi), \quad (\text{C.3})$$

shows that F_ν may be expressed in terms of a derivative of an integral:

$$F_\nu(\rho) = \frac{\nu}{2\rho} \frac{d}{d\rho} \left\{ \int_0^\pi J_0(2\rho \sin \psi) \sin(2\nu\psi) d\psi \right\}.$$

Referring to [15], we see that this integral may be reduced to the simple form

$$\int_0^\pi J_0(2\rho \sin \psi) \sin(2\nu\psi) d\psi = \pi(-1)^k J_{-\nu}(\rho) J_\nu(\rho), \quad (\text{C.4})$$

where k is the integer part of ν . Since ν is a half an odd integer, the final result is most naturally expressed in terms of the spherical Bessel functions $j_k(\rho)$ and $y_k(\rho)$.

After some algebra, one can indeed show

$$F_\nu(\rho) = 2\nu y_k(\rho) \left[j_{k+1}(\rho) - \frac{\nu}{\rho} j_k(\rho) \right] - \frac{\nu}{\rho^2}. \quad (\text{C.5})$$

Furthermore, the Taylor series representation

$$F_\nu(\rho) = \nu \sum_{m=1}^{\infty} \frac{m(-1)^m(2m)!}{4^m(\nu)_{m+1}(1-\nu)_m(m!)^2} \rho^{2(m-1)} \quad (\text{C.6})$$

confirms our intuition that F_ν should be analytic everywhere.

APPENDIX D

THE FUNCTION G_ν

The function G_ν , which appears as the second term on the right hand side of the invariant (29), satisfies

$$\rho G_\nu(\rho) = \sum_{m=-\infty}^{\infty} \frac{m}{\nu - m} J_m(\rho) J'_{2\nu-m}(\rho), \quad (\text{D.1})$$

where the prime denotes a derivative with respect to ρ . If we replace m by the expression $\nu - (\nu - m)$ in the numerator, and apply Neumann's addition theorem [36], (38) becomes

$$\rho G_\nu(\rho) = -\frac{dJ_{2\nu}(2\rho)}{d(2\rho)} + \sum_{m=-\infty}^{\infty} \frac{\nu}{\nu - m} J_m(\rho) J'_{2\nu-m}(\rho). \quad (\text{D.2})$$

Next, the recurrence relation $J'_n(\rho) = [J_{n-1}(\rho) - J_{n+1}(\rho)]$, together with the integral formula [36]

$$J_m(\rho) J_n(\rho) = \frac{2}{\pi} \int_0^{\pi/2} J_{m+n}(2\rho \cos \psi) \cos[(m-n)\psi] d\psi, \quad (\text{D.3})$$

give rise to the identity

$$J_m(\rho) J'_{2\nu-m}(\rho) = \frac{1}{\pi} \int_0^{\pi/2} \{J_{2\nu-1}(\eta) \cos[(\gamma-1)\psi] - J_{2\nu+1}(\eta) \cos[(\gamma+1)\psi]\} d\psi,$$

where $\eta \equiv 2\rho \cos \psi$ and $\gamma \equiv 2(\nu - m)$. By introducing this identity into the sum in (39), and then shifting summation indices, it can be shown that

$$\sum_{m=-\infty}^{\infty} \frac{\nu}{\nu - m} J_m(\rho) J'_{2\nu-m}(\rho) = \frac{2\nu}{\pi\rho} \int_0^{\pi/2} \frac{J_{2\nu}(2\rho \cos \psi)}{\cos \psi} \sum_{m=-\infty}^{\infty} \frac{\cos(2m\psi)}{m + 1/2} d\psi.$$

Finally, when $\psi \in [0, \pi]$, the Fourier series

$$\frac{1}{\pi} \sum_{m=-\infty}^{\infty} \frac{\cos(2m\psi)}{m + 1/2} = \sin \psi \quad (\text{D.4})$$

reduces the expression for G_ν to

$$\rho G_\nu(\rho) = -\frac{dJ_{2\nu}(2\rho)}{d(2\rho)} + \frac{2\nu^2}{\rho} \int_0^{2\rho} \frac{J_{2\nu}(u)}{u} du, \quad (\text{D.5})$$

which can be expressed in terms of tabulated functions as

$$G_\nu(\rho) = -\frac{1}{\rho} \frac{dJ_{2\nu}(2\rho)}{d(2\rho)} + \frac{\nu}{\rho^2} \left\{ \int_0^{2\rho} J_0(u) du - J_1(2\rho) \right\} - \frac{2\nu}{\rho^3} \sum_{m=0}^k m J_{2m}(2\rho), \quad (\text{D.6})$$

where k is the integer part of ν . The Taylor series

$$G_\nu(\rho) = \rho^{2\nu} \sum_{m=0}^{\infty} \frac{(-\rho^2)^m}{m!(2\nu+m)!(\nu+m+1)} \quad (\text{D.7})$$

shows that G_ν is analytic for all positive ν .

APPENDIX E
TABLES AND FIGURES

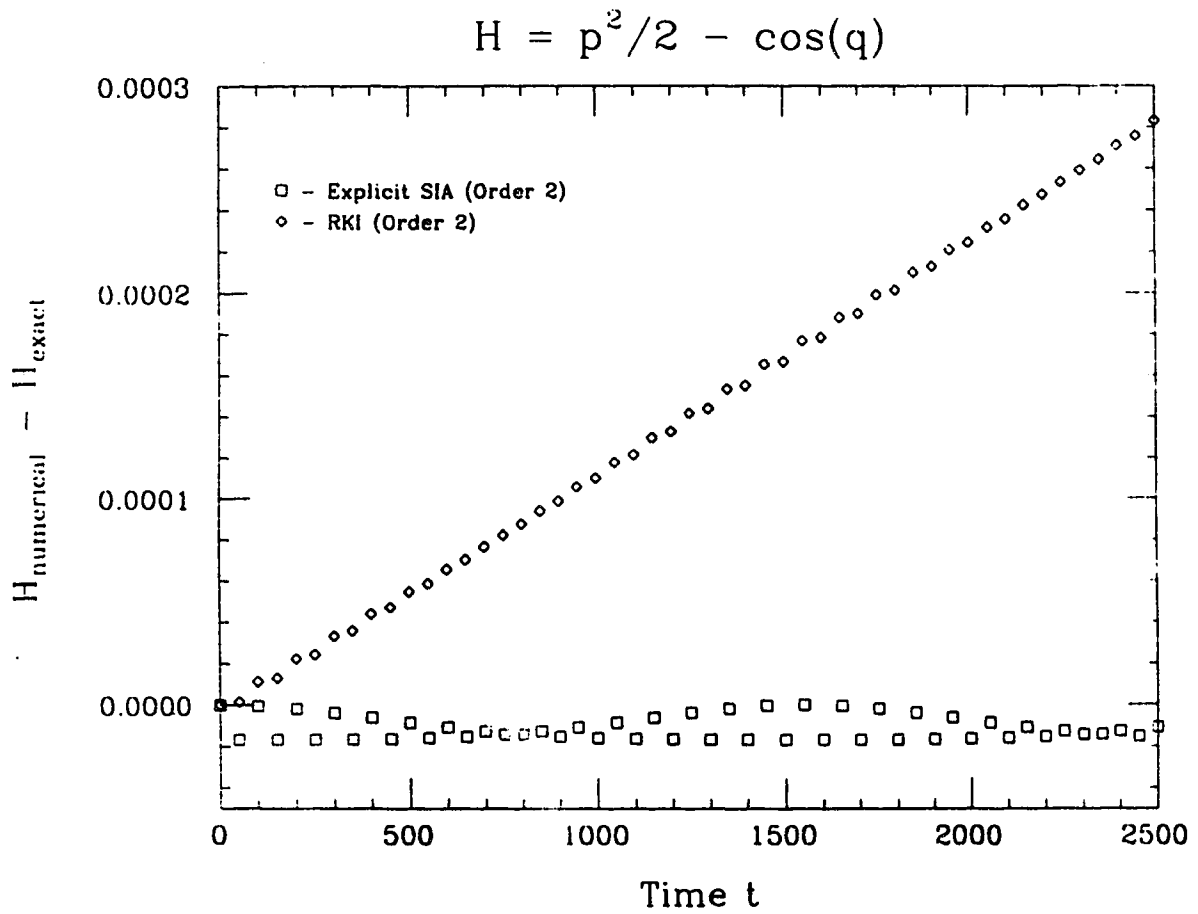


Figure E.1: Comparison of the relative error in energy when using SIA2 and RKI2 to integrate (2.41), with initial conditions $(q_0, p_0, t_0) = (0, 1.4, 0)$, and time step $\delta t = 0.01$.

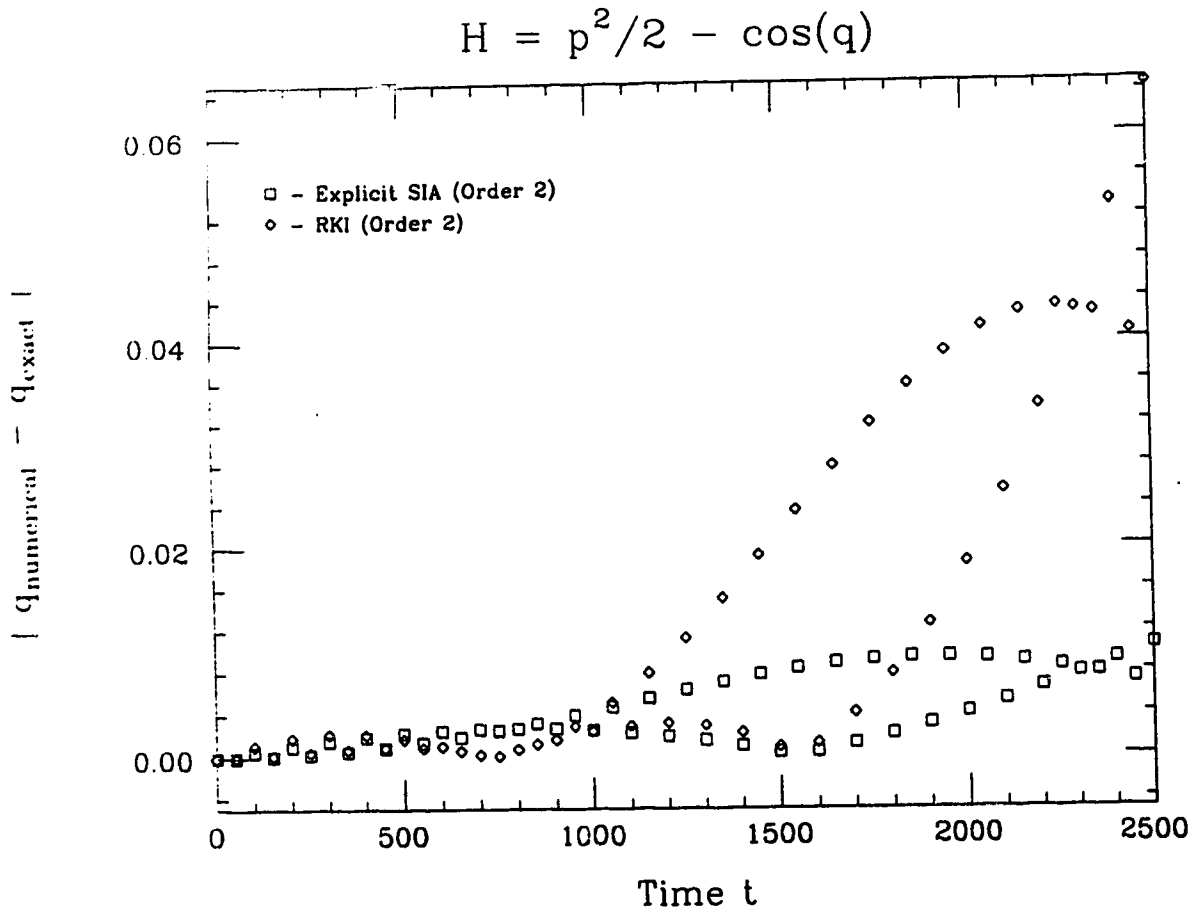


Figure E.2: Comparison of the absolute error in position when using SIA2 and RKI2 to integrate (2.41), with initial conditions $(q_0, p_0, t_0) = (0, 1.4, 0)$, and time step $\delta t = 0.01$.

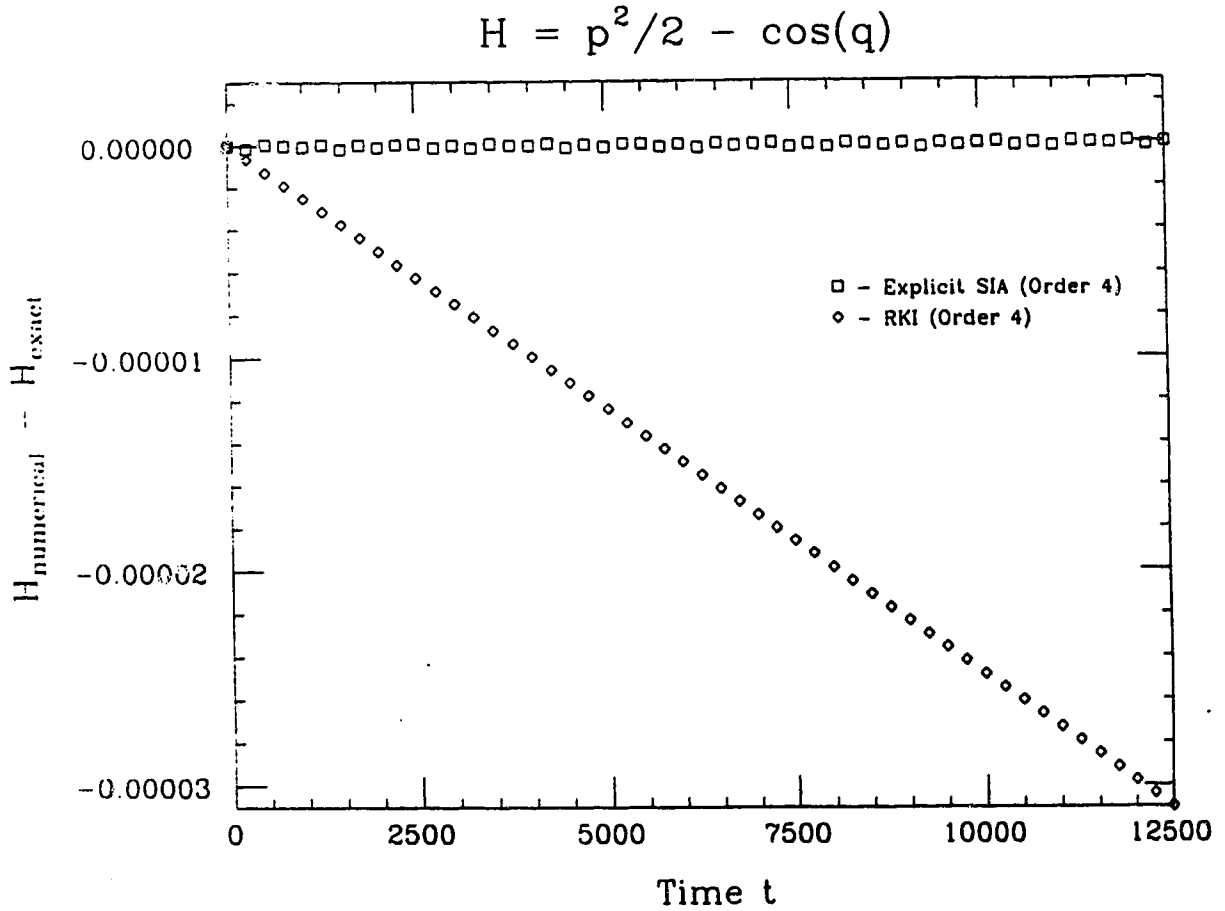


Figure E.3: Comparison of the relative error in energy when using SIA2 and RKI2 to integrate (2.41), with initial conditions $(q_0, p_0, t_0) = (0, 1.4, 0)$, and time step $\delta t = 0.05$.

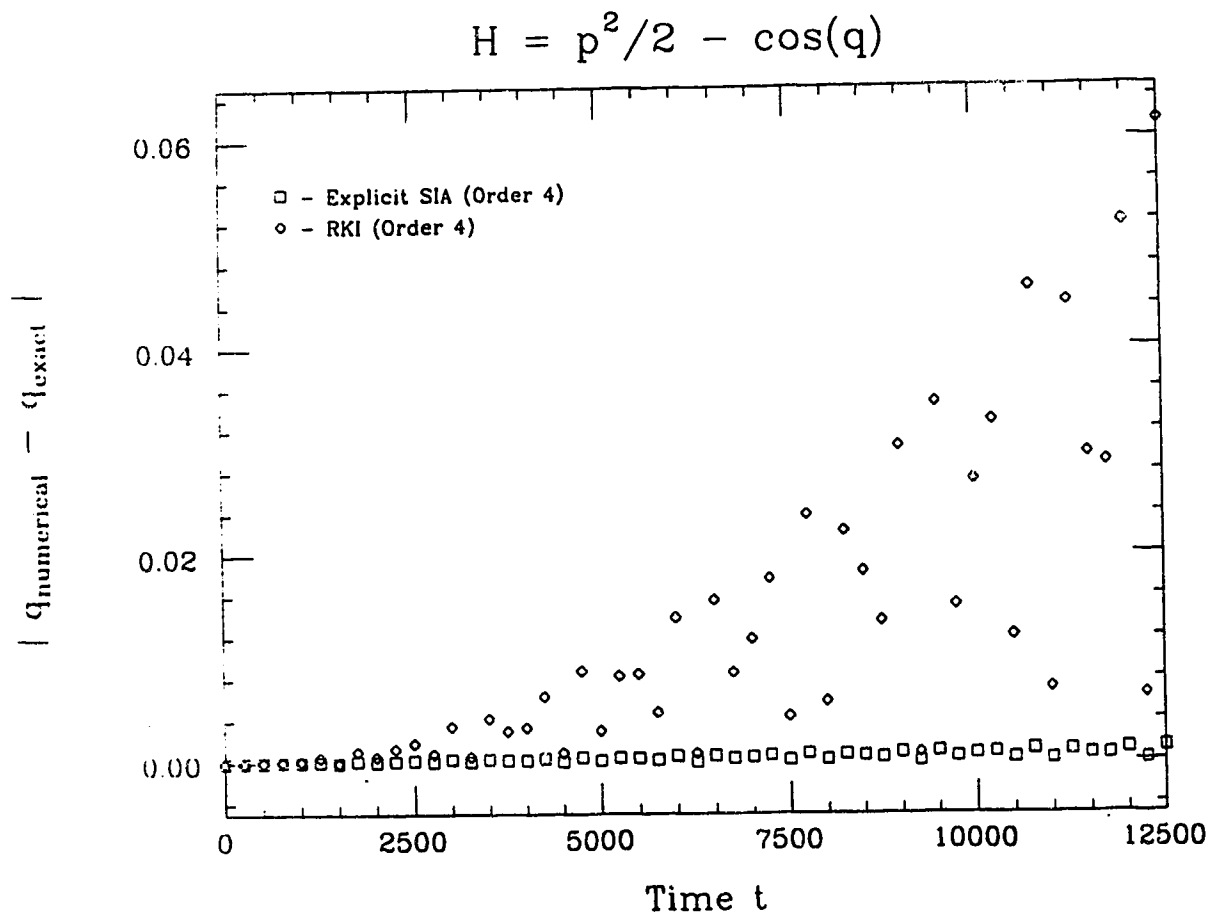


Figure E.4: Comparison of the absolute error in position when using SIA2 and RKI2 to integrate (2.41), with initial conditions $(q_0, p_0, t_0) = (0, 1.4, 0)$, and time step $\delta t = 0.05$.

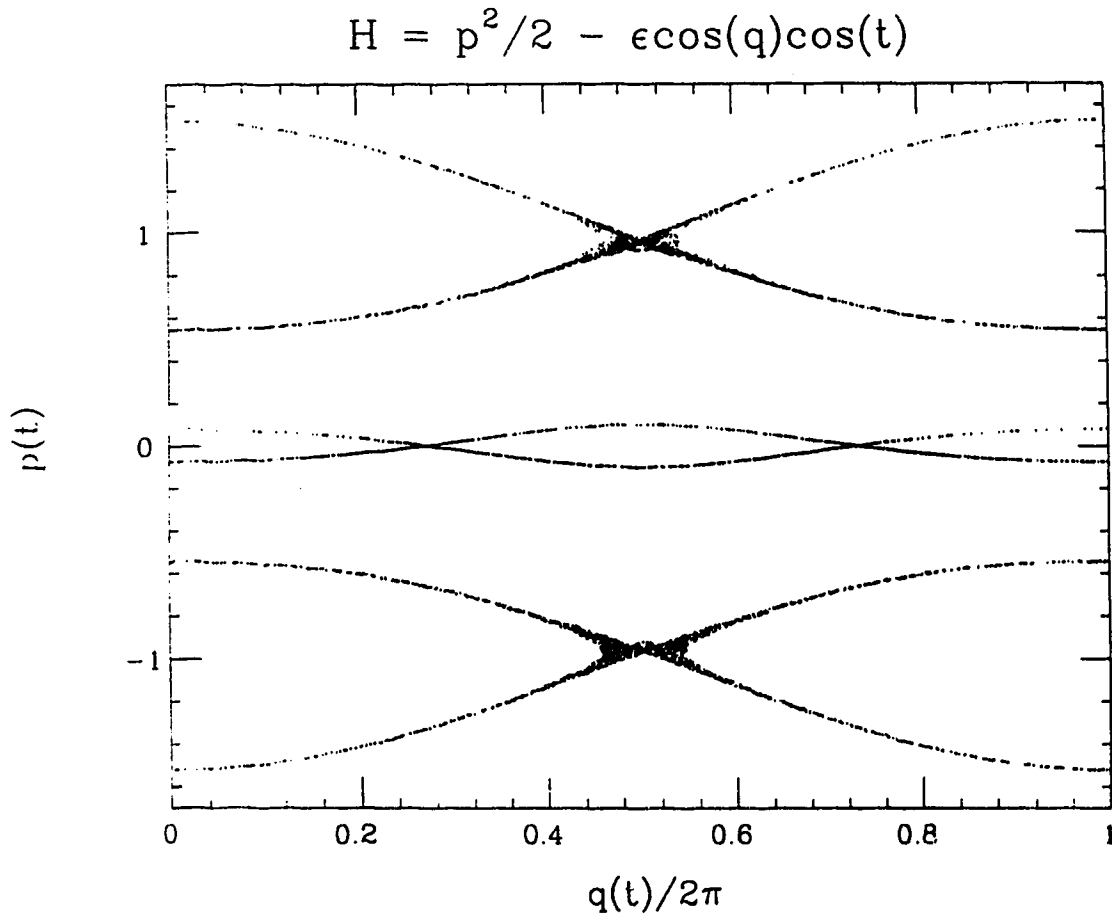


Figure E.5: Phase space of (2.43) for $\epsilon = 1/8$. The large separatrices at top and bottom correspond to resonance with the travelling waves in (2.42). The small, middle separatrix corresponds to the ponderomotive potential well.

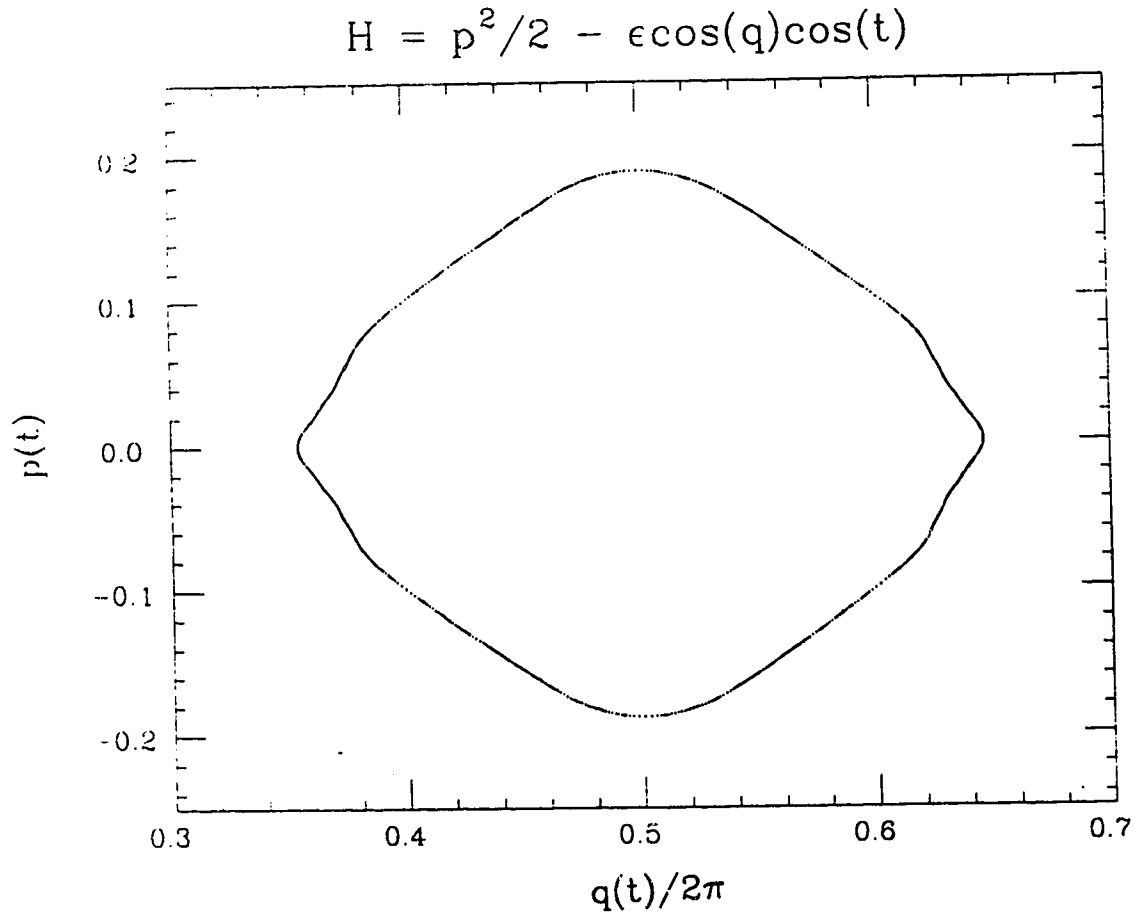


Figure E.6: Poincaré map of a single trajectory of (2.43) using SIA4. The initial conditions are $(q_0, p_0, t_0) = (\pi, 0.188, 0)$, $\epsilon = 0.73/\pi \simeq 0.23$, $\delta t = 2\pi/25 \simeq 0.25$, with 30 000 plotted points.

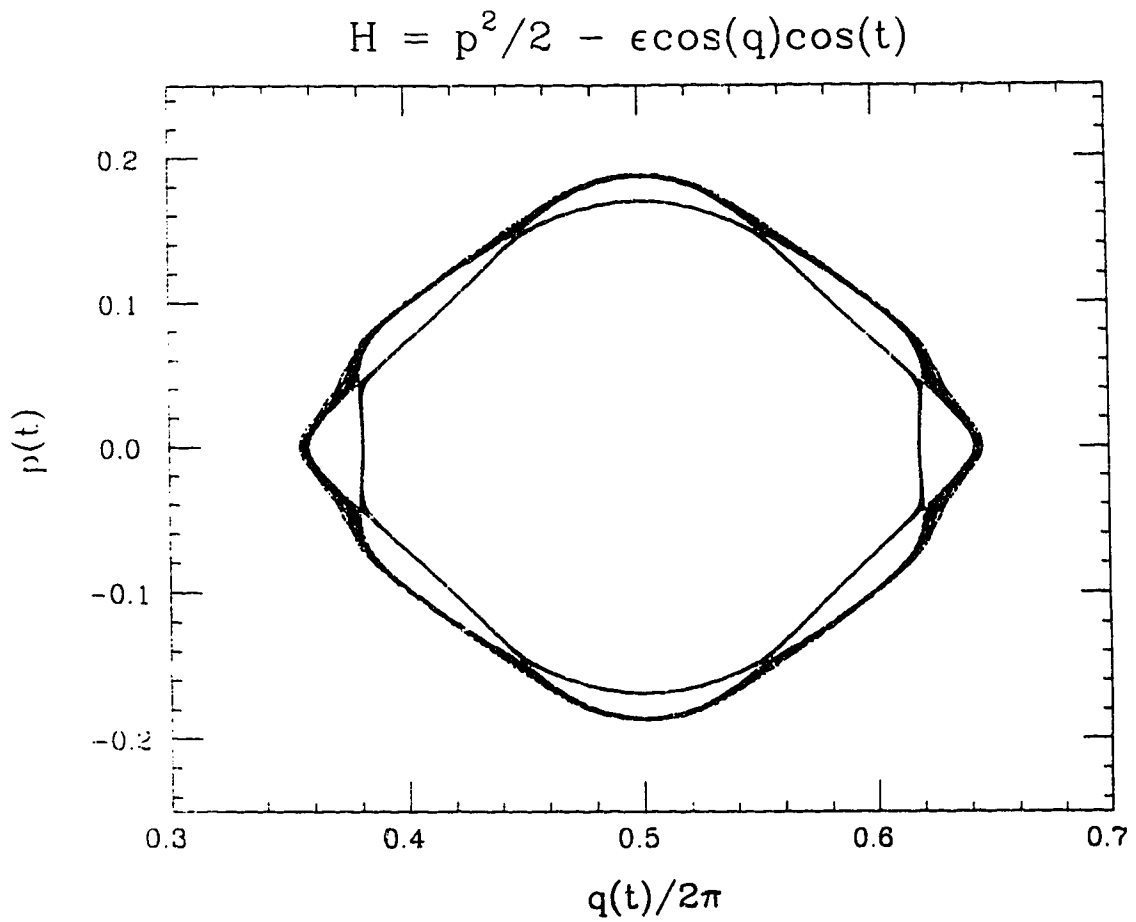


Figure E.7: Same as in Figure E.6, except using RKI4.

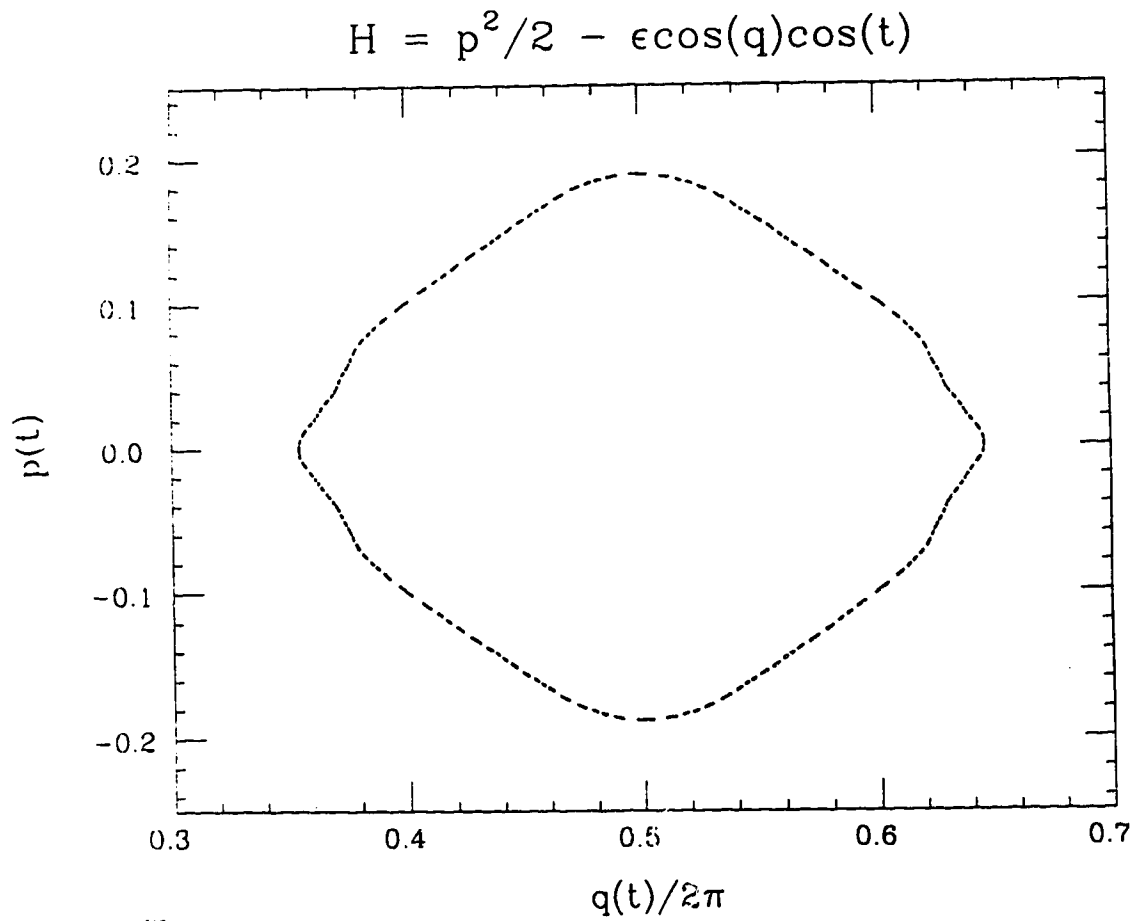


Figure E.8: Same as in Figure E.6, except using ISIA4.

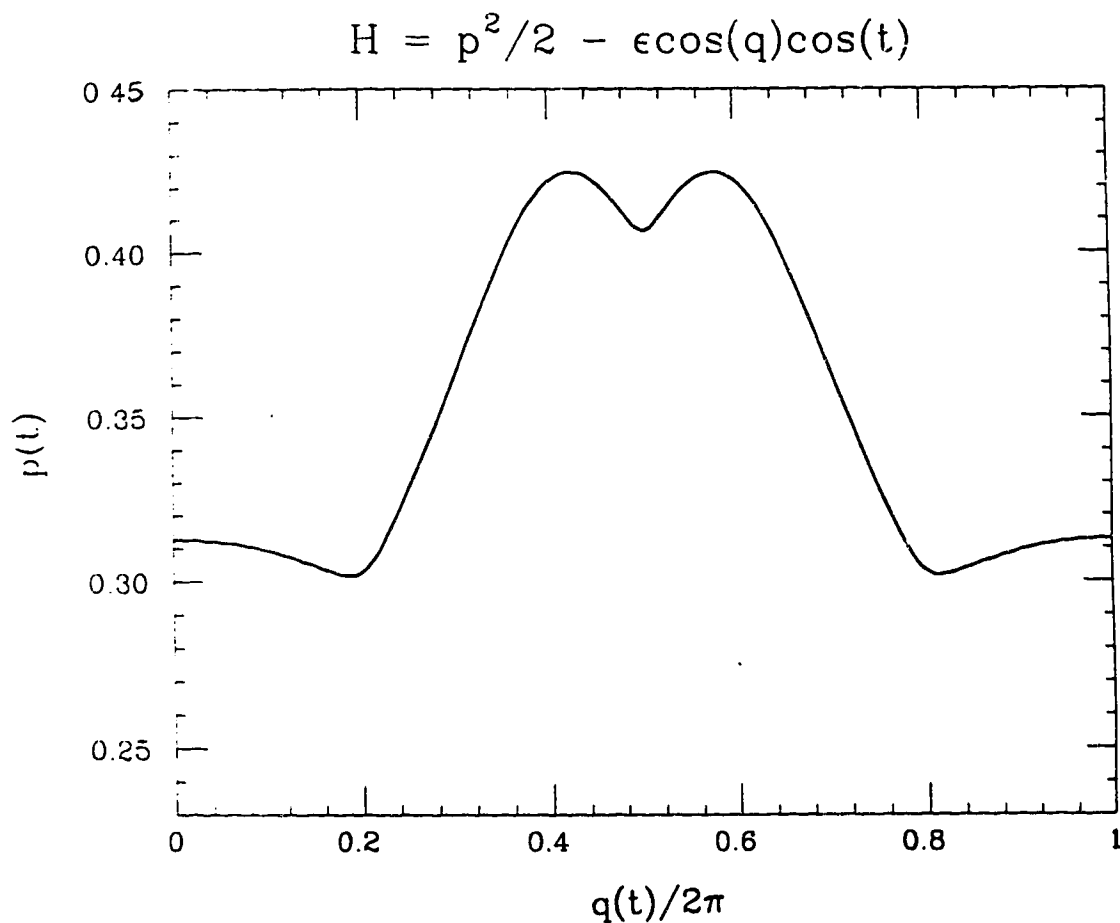


Figure E.9: Poincaré map of a single trajectory of (2.43) using SIA4. The initial conditions are $(q_0, p_0, t_0) = (0, 0.31255, 0)$, $\epsilon = 1/2\pi \simeq 0.16$, $\delta t = 2\pi/30 \simeq 0.21$, with 30 000 plotted points.

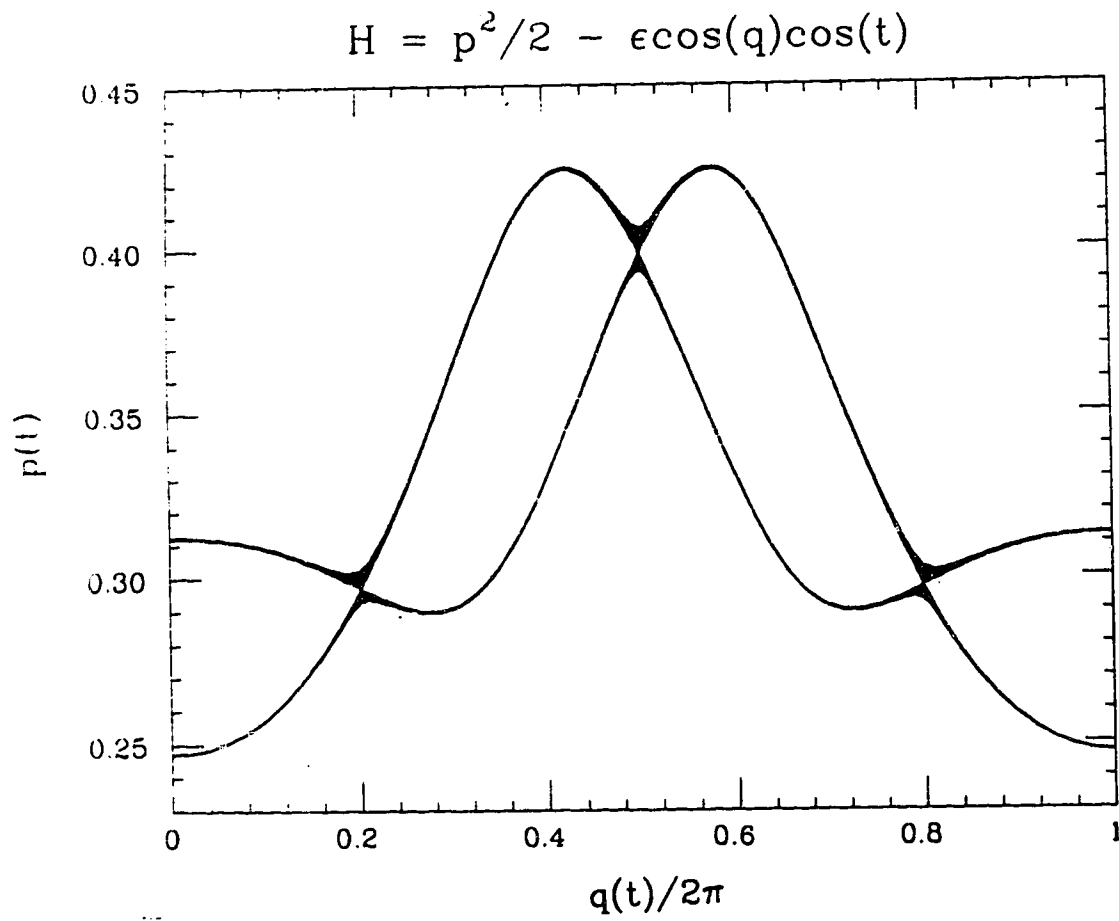


Figure E.10: Same as in Figure E.9, except using RKI4.

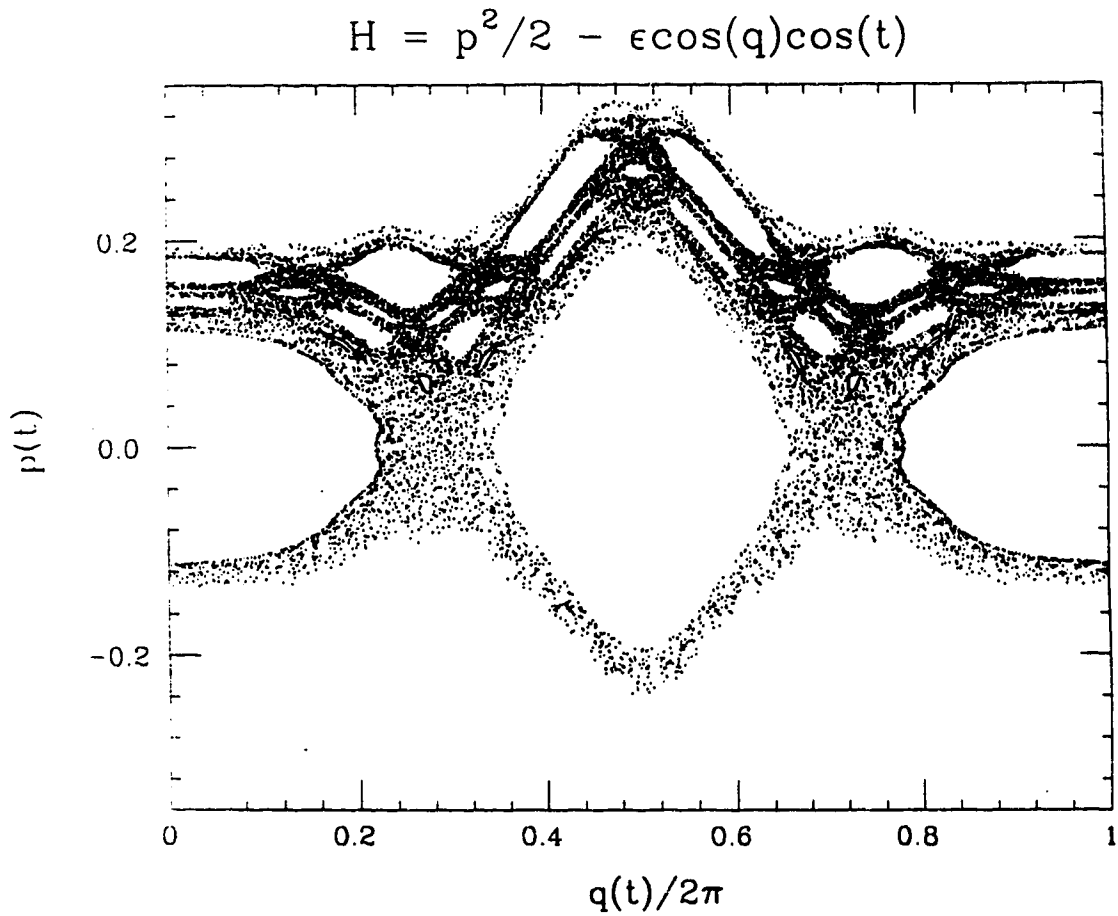


Figure E.11: Poincaré map of a single trajectory of (2.43) using SIA4. The initial conditions are $(q, p, t) = (\pi, 0.255, 0)$, $\epsilon = 0.73/\pi \simeq 0.23$, $\delta t = 2\pi/30 \simeq 0.21$, with 25 000 plotted points.

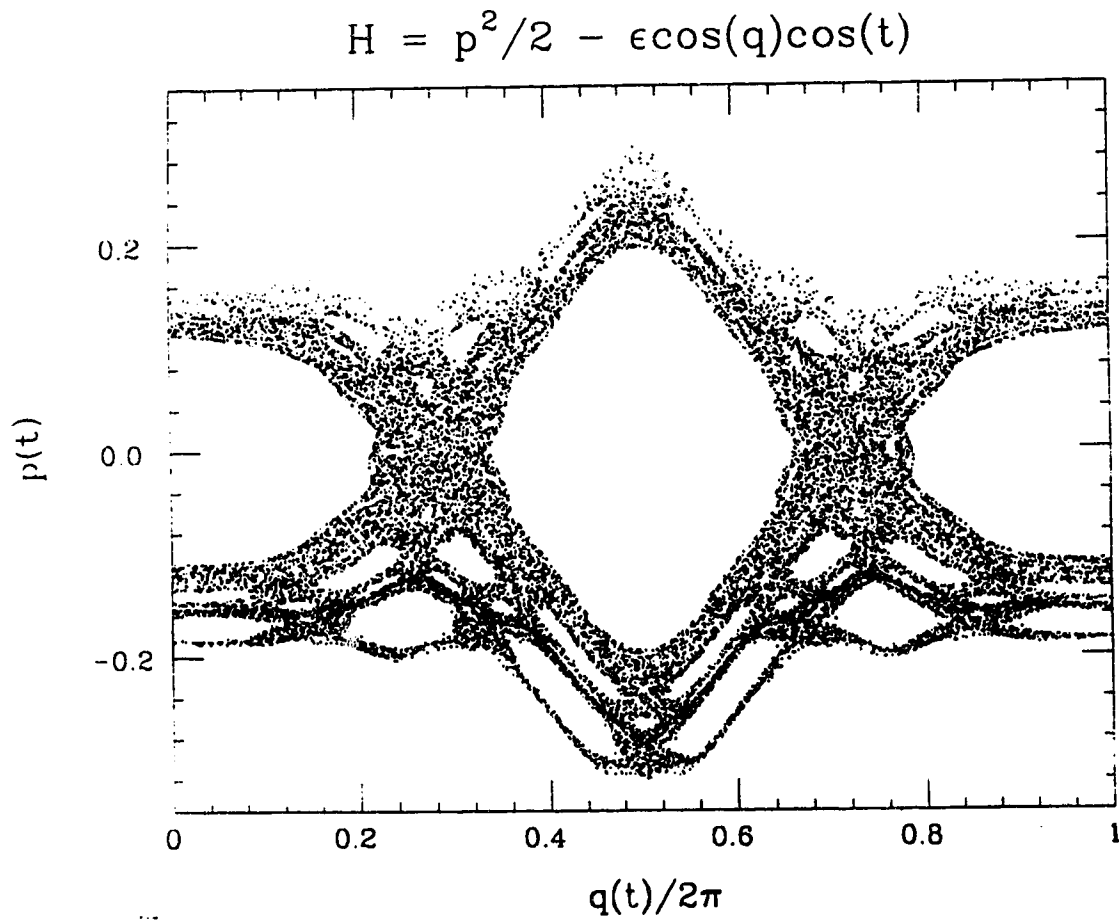


Figure E.12: Same as in Figure E.11, except using RKI4.

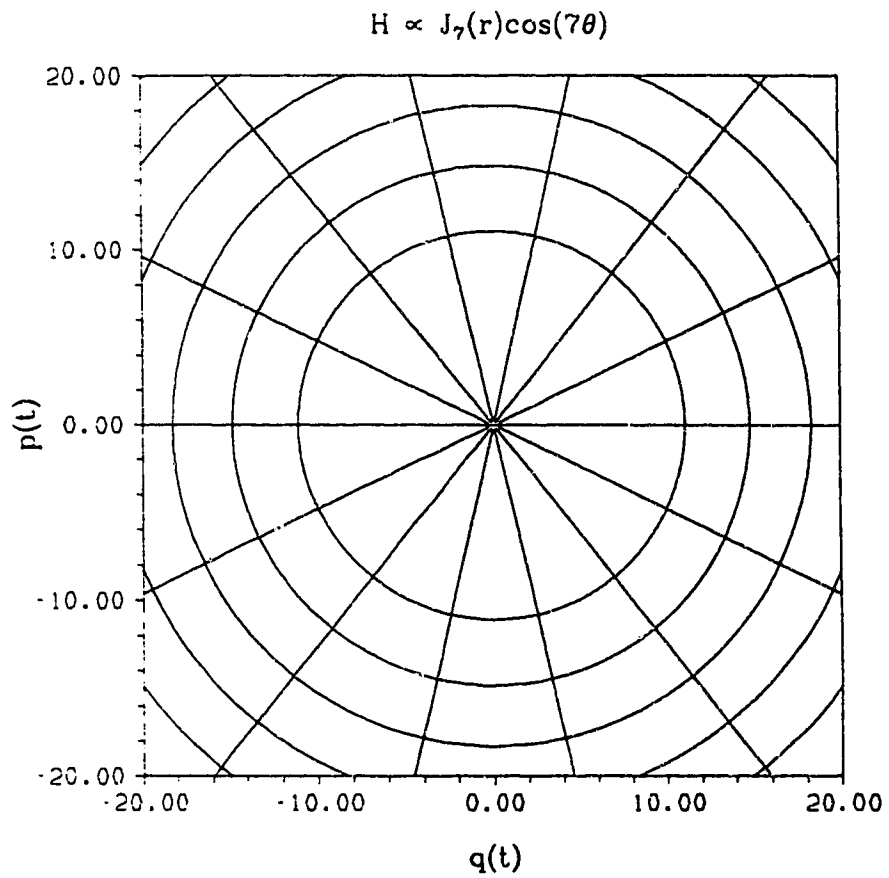


Figure E.13: Separatrix mesh of (2.45) after averaging, for $\omega = 7$ and $\epsilon \ll 1$. The variables are defined by $q = r \sin \theta$ and $p = r \cos \theta$.

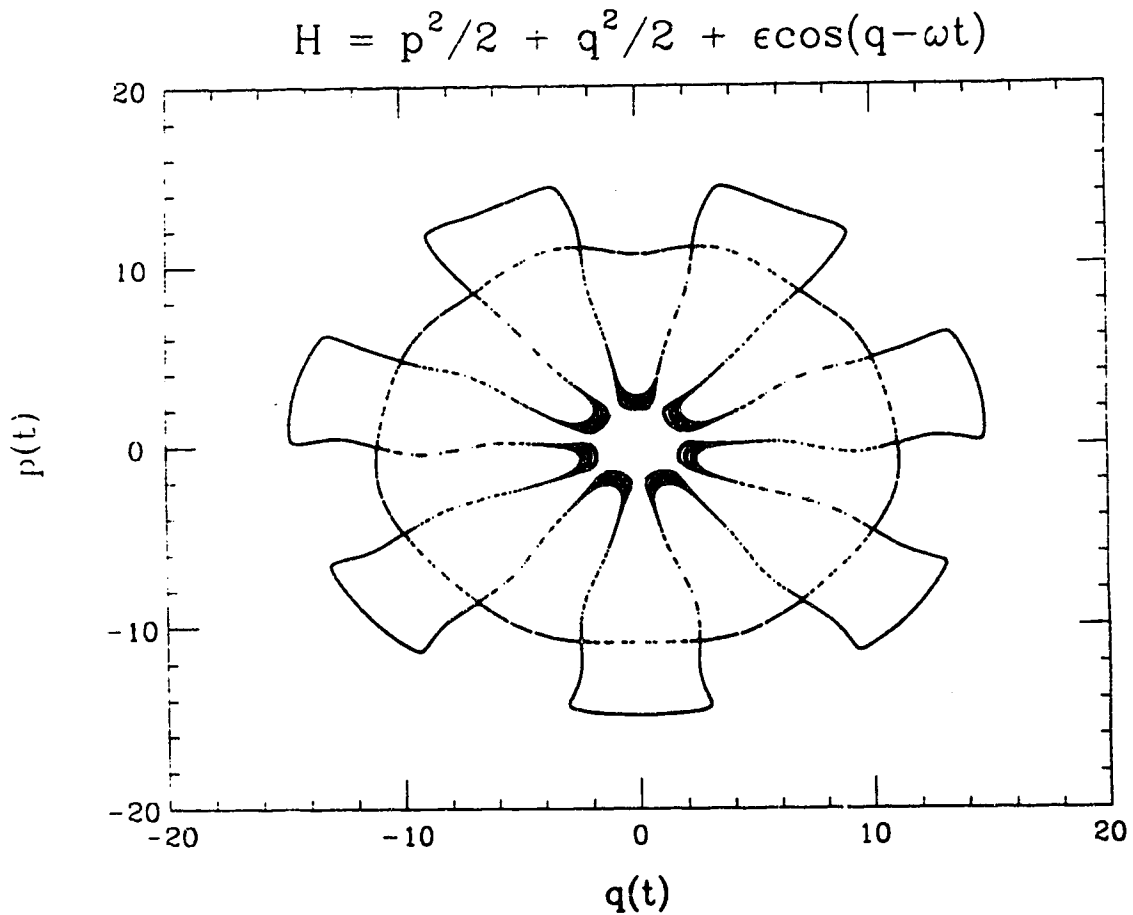


Figure E.14: Poincaré map of a single trajectory of (2.45) using SIA4. The initial conditions are $(q_0, p_0, t_0) = (0, 10.5939, 0)$, $\epsilon = 0.8$, $\omega = 7$, $\delta t = 2\pi/63 \simeq 0.1$, with 35 000 plotted points.

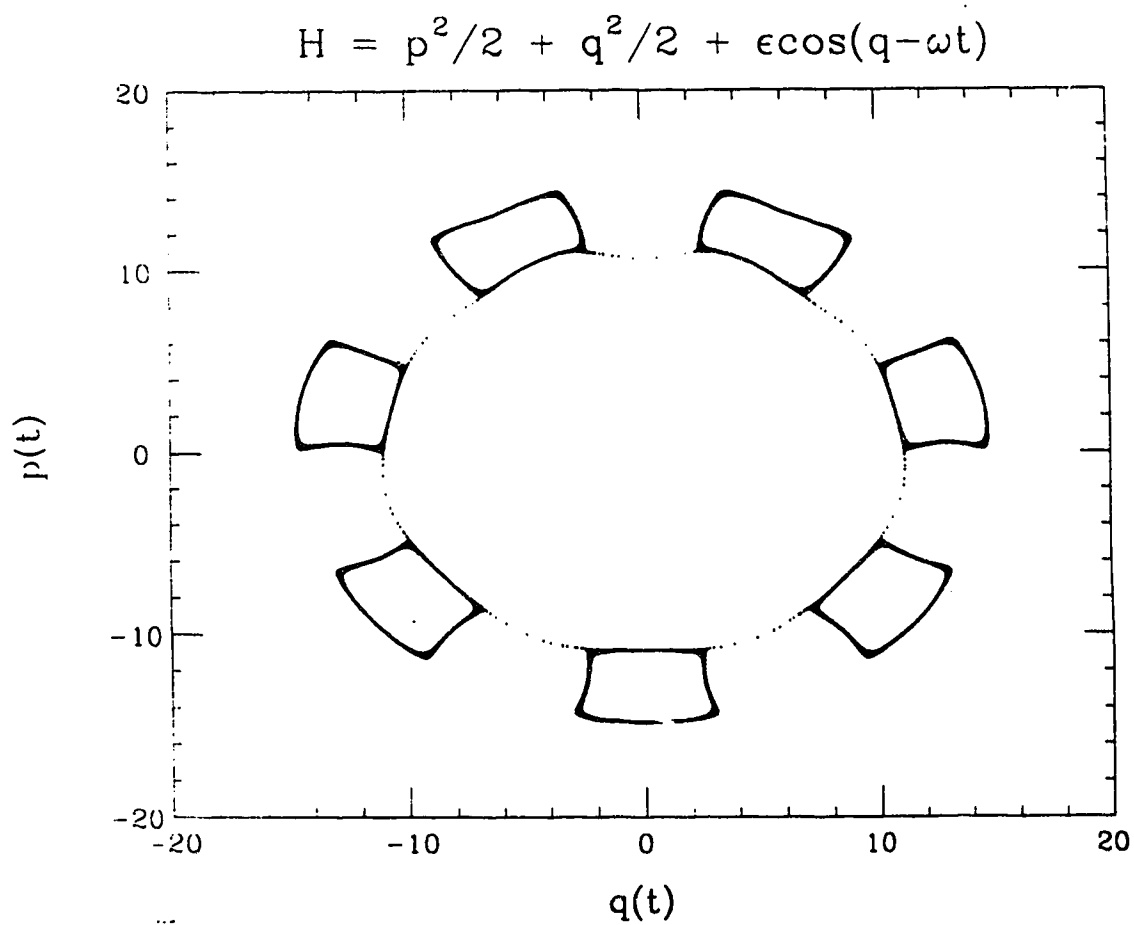


Figure E.15: Same as in Figure E.14, except using RKI4.

APPENDIX F
TABLES AND FIGURES (CONT'D)

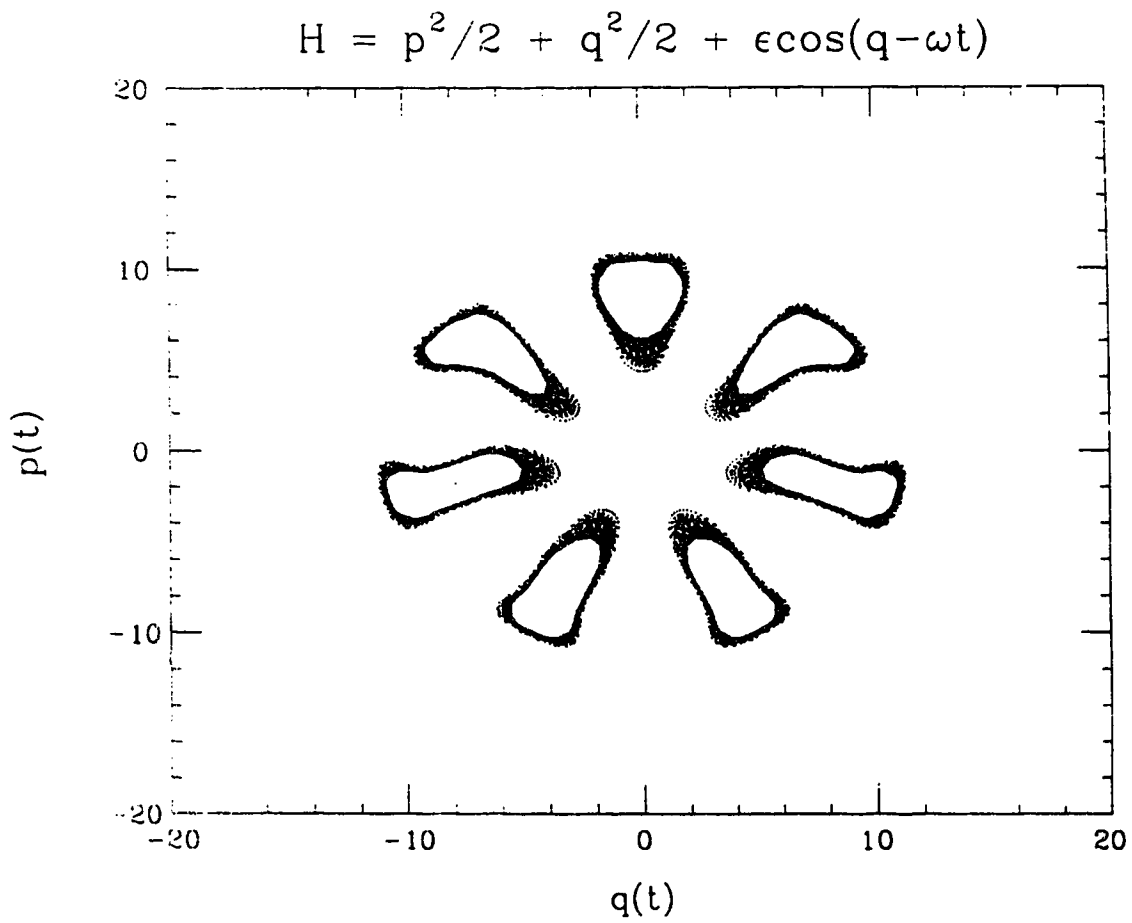


Figure F.1: Poincaré map of a single trajectory of (2.45) using SIA2. The initial conditions are $(q_0, p_0, t_0) = (0, 4.5, 0)$, $\epsilon = 1.2$, $\omega = 7$, $\delta t = 2\pi/210 \simeq 0.03$, with 20 000 plotted points.

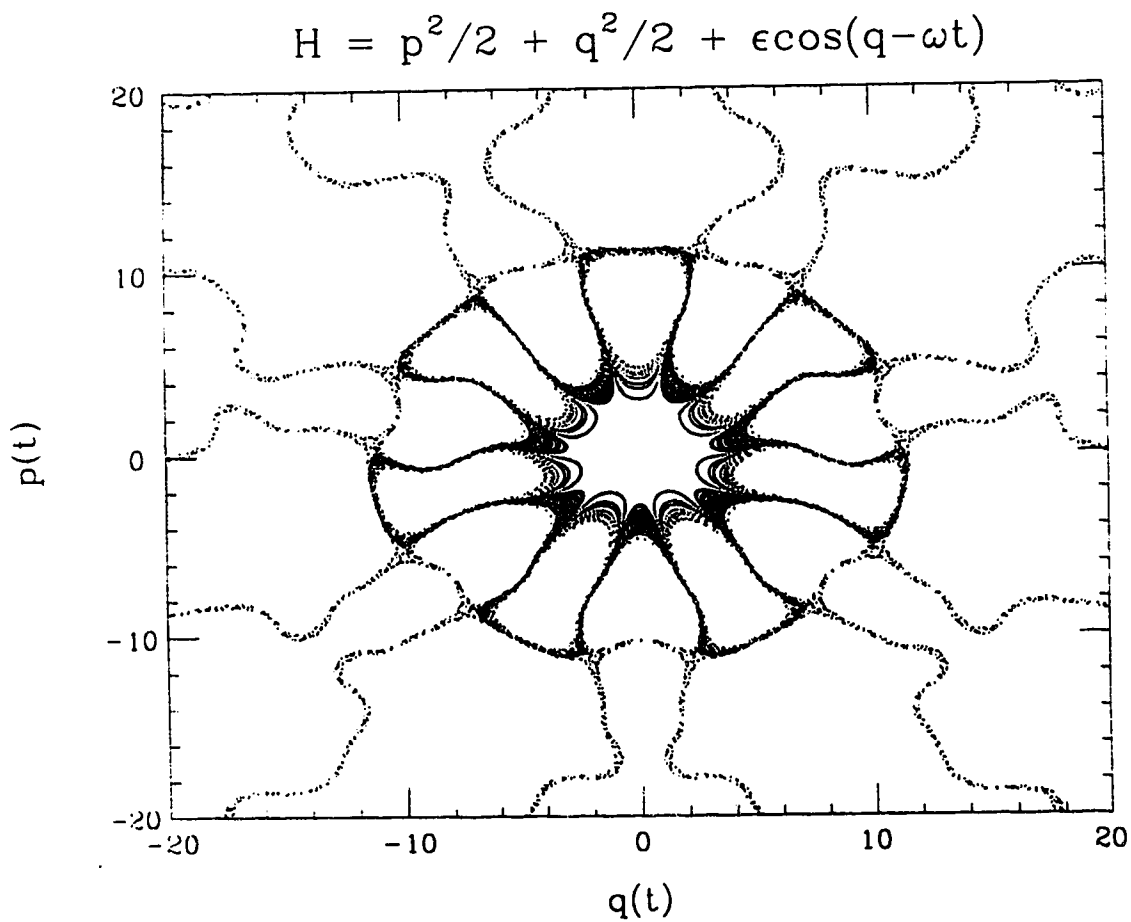


Figure F.2: Same as in Figure F.1, except using RKI4.

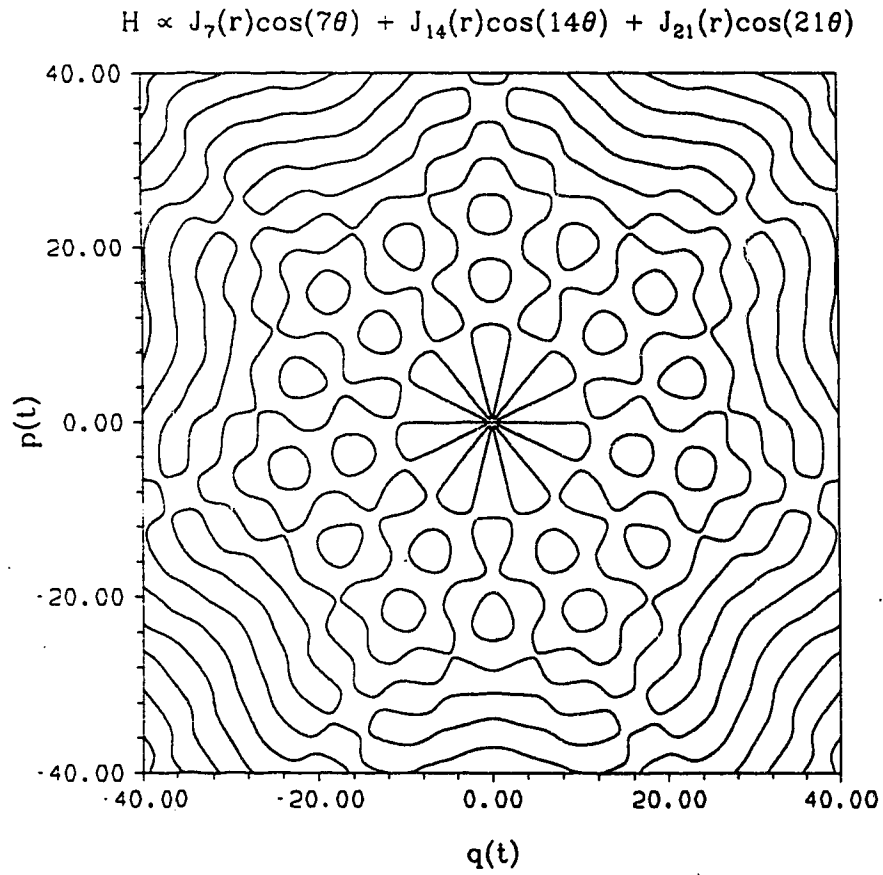


Figure F.3: Separatrix mesh of (2.46) after averaging, for $s = 3$, $\omega_1 = 7$, $\omega_2 = 14$, $\omega_3 = 21$ and $\epsilon \ll 1$. The variables are defined by $q = r \sin \theta$ and $p = r \cos \theta$.

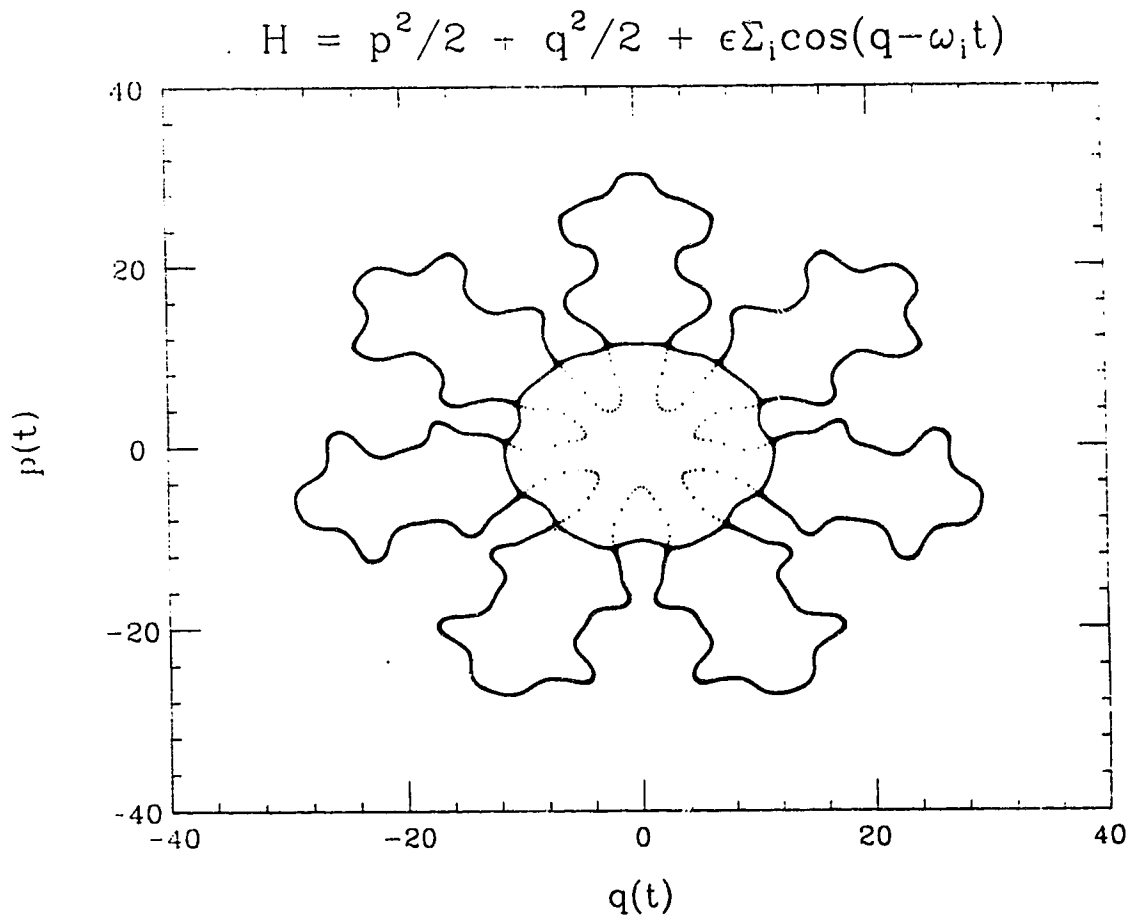


Figure F.4: Poincaré map of a single trajectory of (2.46) using SIA4. The initial conditions are $(q_0, p_0, t_0) = (0, 11.2075, 0)$, $\epsilon = 1$, $s = 3$, $\omega_1 = 7$, $\omega_2 = 14$, $\omega_3 = 21$, $\delta t \doteq 2\pi/105 \simeq 0.06$, with 38 000 plotted points.

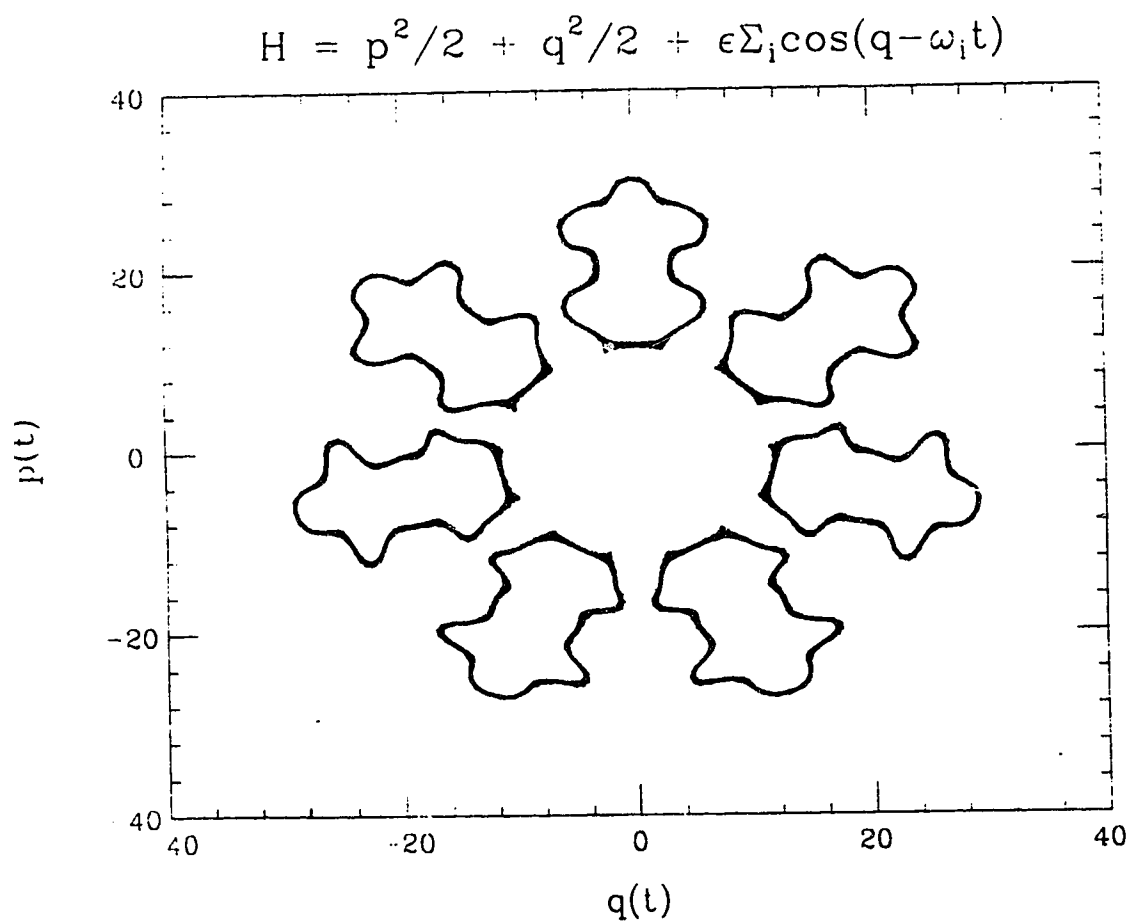


Figure F.5: Same as in Figure F.4, except using RKI4.

Table F.1: Summary of different choices of algorithms.

order	equate to zero	n	equations	variables
1	h_0	1	2	2
2	h_0, h_1	2	3	4
3	h_0, h_1, h_2	3	5	6
4	h_0, h_1, h_2, h_3	4	8	8

Table F.2: Summary of coefficients for various algorithms.

order (n)	coefficients
1	$(a_1, b_1) = (1, 1)$
2	$(a_1, a_2, b_1, b_2) = (\frac{1}{2}, \frac{1}{2}, 0, 1)$
3	$(a_1, a_2, a_3, b_1, b_2, b_3) = (\frac{2}{3}, -\frac{2}{3}, 1, \frac{7}{24}, \frac{3}{4}, -\frac{1}{24})$
4	$a_1 = a_4 = \frac{1}{6}(2 + 2^{1/3} + 2^{-1/3})$ $a_2 = a_3 = \frac{1}{6}(1 - 2^{1/3} - 2^{-1/3})$ $b_1 = 0$ $b_2 = b_4 = (2 - 2^{1/3})^{-1}$ $b_3 = (1 - 2^{2/3})^{-1}$

Table F.3: General scheme for a δt time-step integration.

Hamiltonian: $H(\mathbf{q}, \mathbf{p}) = T(\mathbf{p}) + V(\mathbf{q})$
Initial Conditions: $(\mathbf{q}_0, \mathbf{p}_0)$ at $t = t_0$
<p>Do for $i = 1$ to n:</p> $\mathbf{p}_i = \mathbf{p}_{i-1} + b_i \mathbf{F}(\mathbf{q}_{i-1}) \delta t \quad \mathbf{q}_i = \mathbf{q}_{i-1} + a_i \mathbf{P}(\mathbf{p}_i) \delta t$
Integrated Variables: $(\mathbf{q}_n, \mathbf{p}_n)$ at $t = t_0 + \delta t$

Table F.4: General scheme for a δt time-step integration.

<p>Hamiltonian: $H(\mathbf{q}, \mathbf{p}, t) = T(\mathbf{p}) + V(\mathbf{q}, t)$</p>
<p>Initial Conditions: $(\mathbf{q}_0, \mathbf{p}_0)$ at $t = t_0$</p>
<p>Do for $i = 1$ to n:</p> $\mathbf{p}_i = \mathbf{p}_{i-1} + b_i \mathbf{F}(\mathbf{q}_{i-1}, t_{i-1}) \delta t \quad \mathbf{q}_i = \mathbf{q}_{i-1} + a_i \mathbf{P}(\mathbf{p}_i) \delta t$ $t_i = t_{i-1} + a_i \delta t$
<p>Integrated Variables: $(\mathbf{q}_n, \mathbf{p}_n)$ at $t = t_0 + \delta t$</p>

Table F.5: Execution time (in sec.) for various integration methods.

	$\delta t = 0.5$	$\delta t = 0.1$	$\delta t = 0.01$
SIA4	22.31	22.25	21.59
RKI4	31.79	31.74	30.88
ISIA4	42.64	32.77	26.69

APPENDIX G
TABLES AND FIGURES (CONT'D)

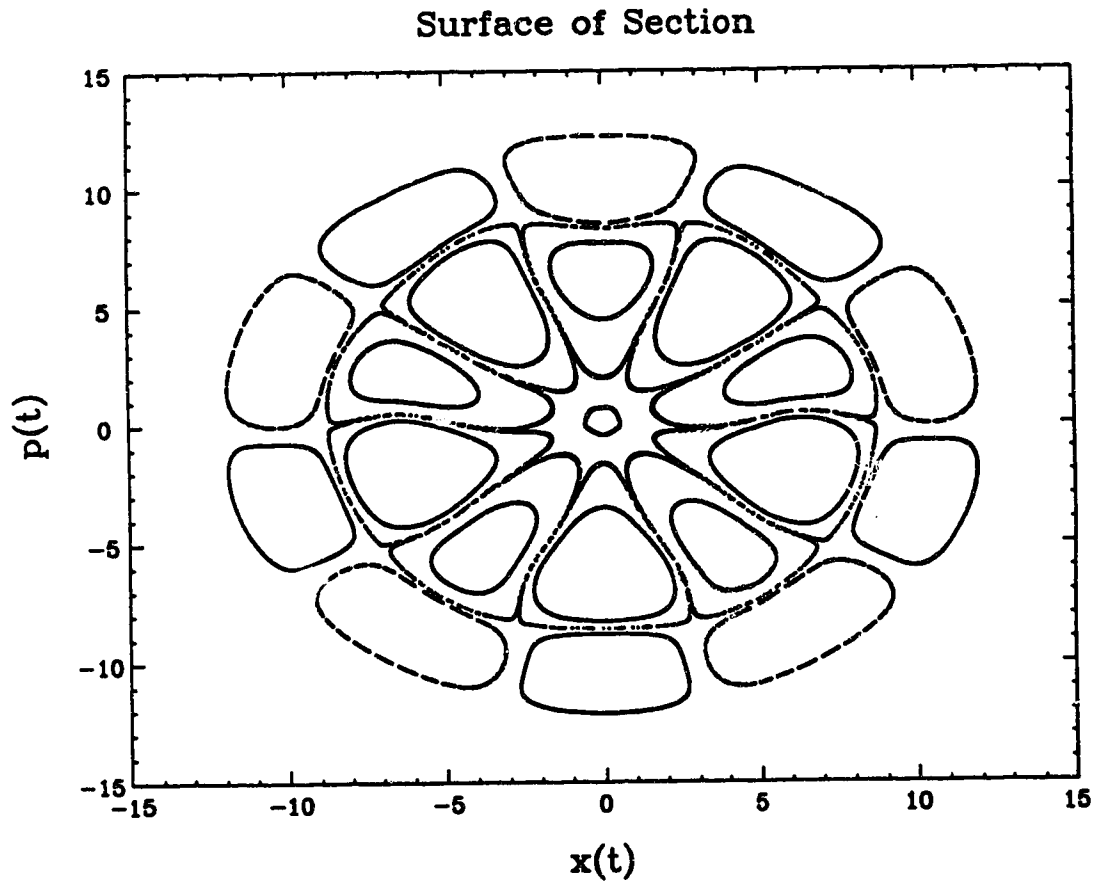


Figure G.1: Surface of section of the Hamiltonian (3.2) for $N = 1$. The wave parameters are $\epsilon_1 = 0.7$ m, $\nu_1 = 5$, $k_1 = 1$ m⁻¹ and $\varphi_1 = 0$. Points are plotted at the times $T_p = 2\pi p/\nu_1$. Trajectories corresponding to various initial conditions are plotted, and the integration parameter j is 20.

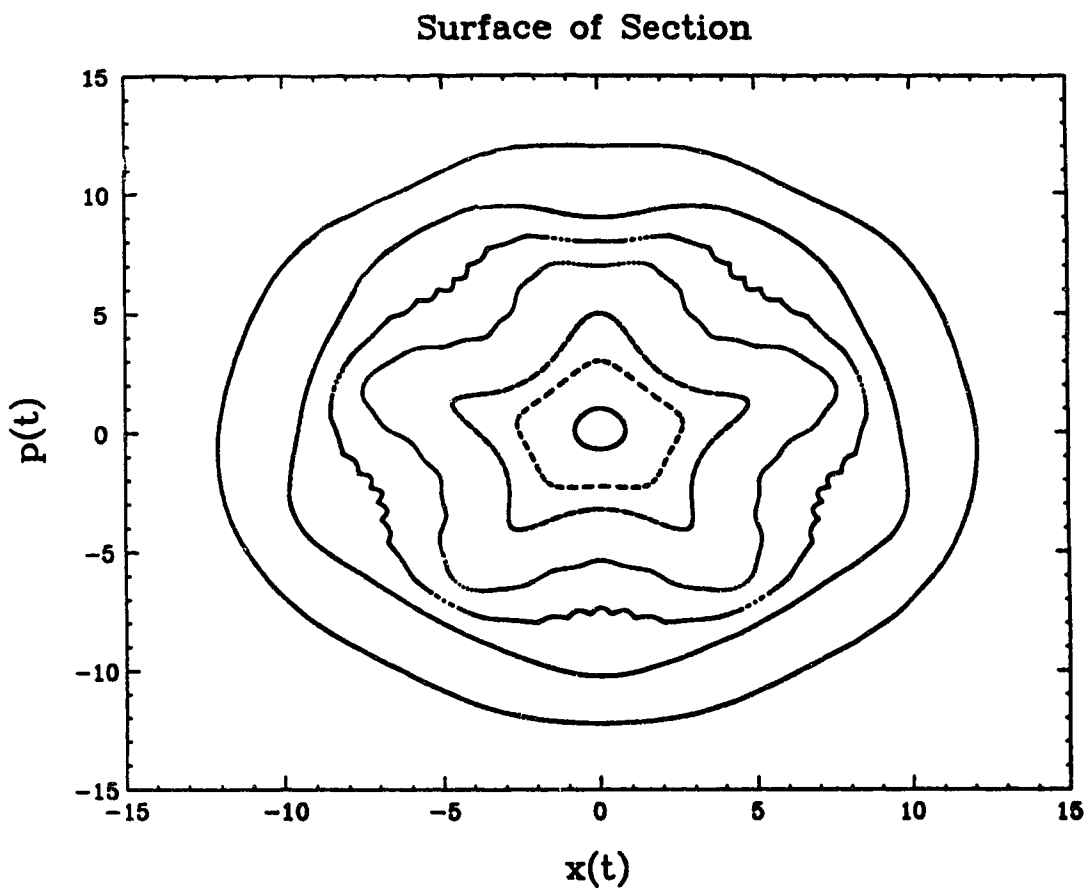


Figure G.2: Same as Figure G.1, except $\nu_1 = 5.16$.

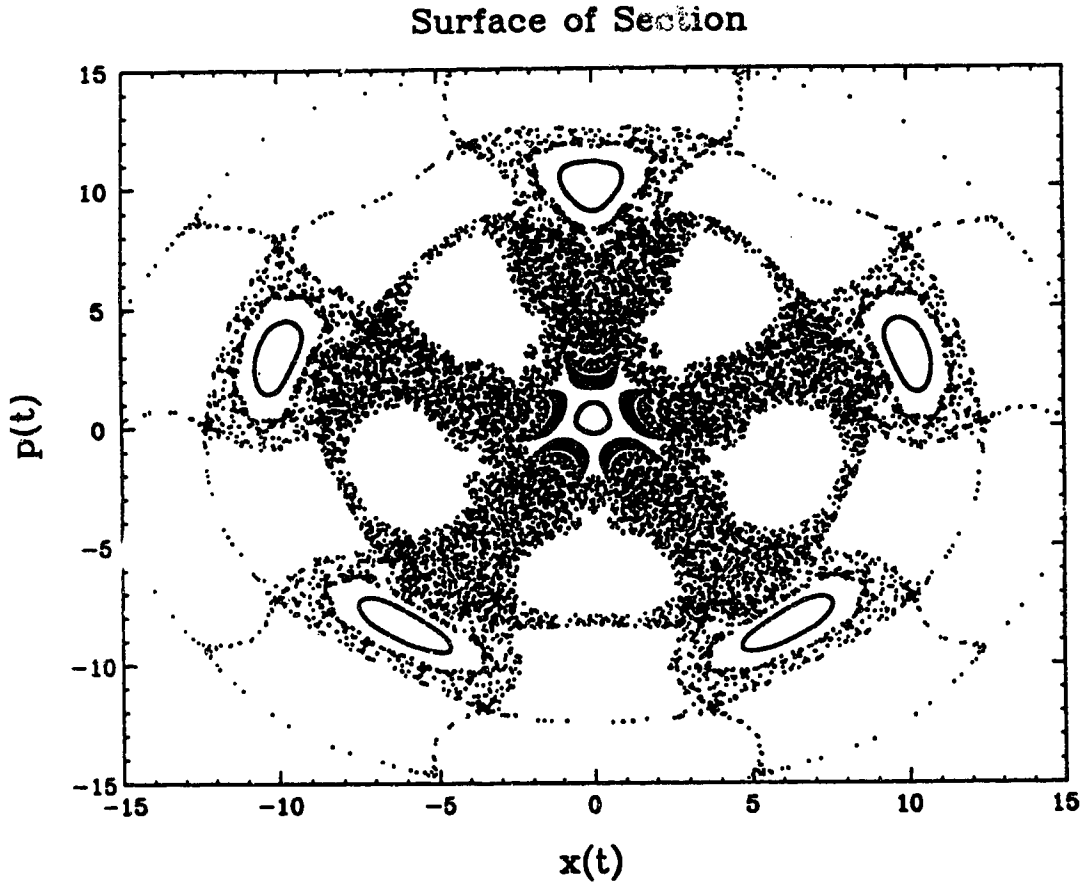


Figure G.3: Surface of Section of the Hamiltonian (3.2) for $N = 1$. The wave parameters are $\epsilon_1 = 1 \text{ m}$, $\nu_1 = 5$, $k_1 = 1 \text{ m}^{-1}$ and $\varphi_1 = 0$. Points are plotted at the times $T_p = 2\pi p/\nu_1$. Trajectories corresponding to various initial conditions are plotted, and the integration parameter j is 20.

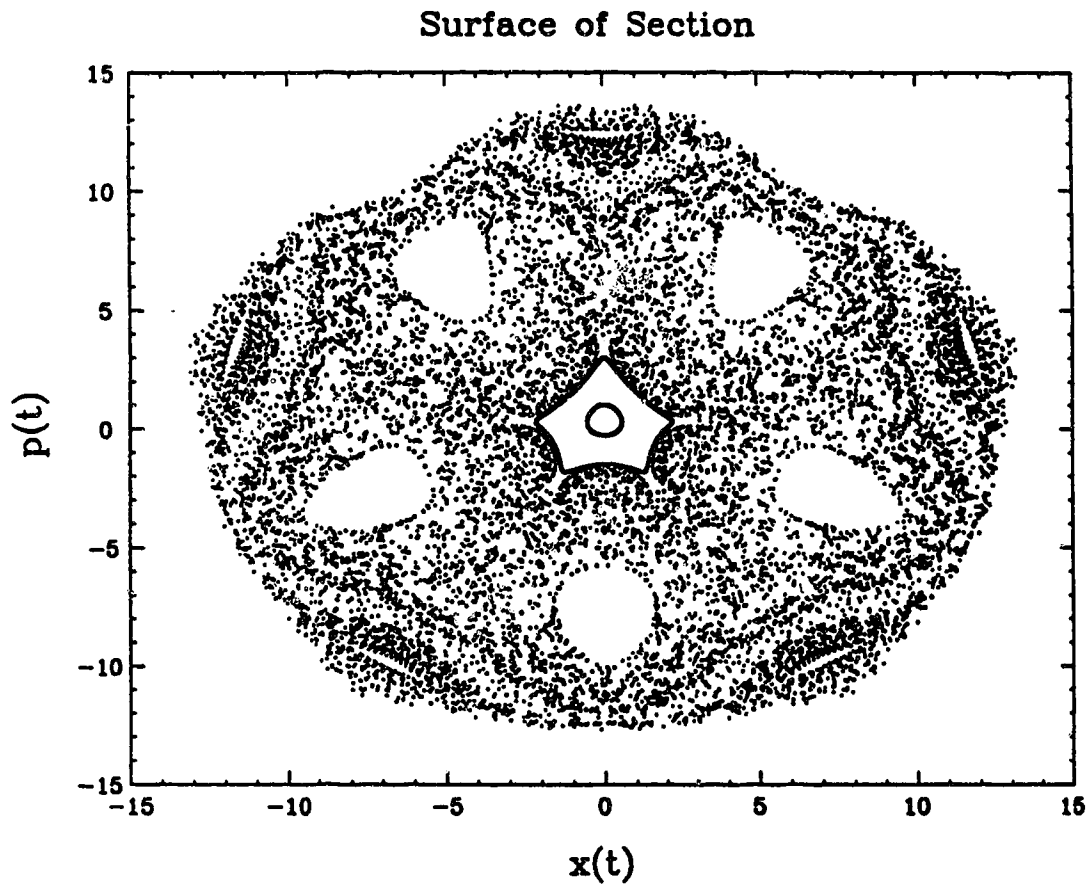


Figure G.4: Same as Figure G.3, except $\nu_1 = 5.16$.

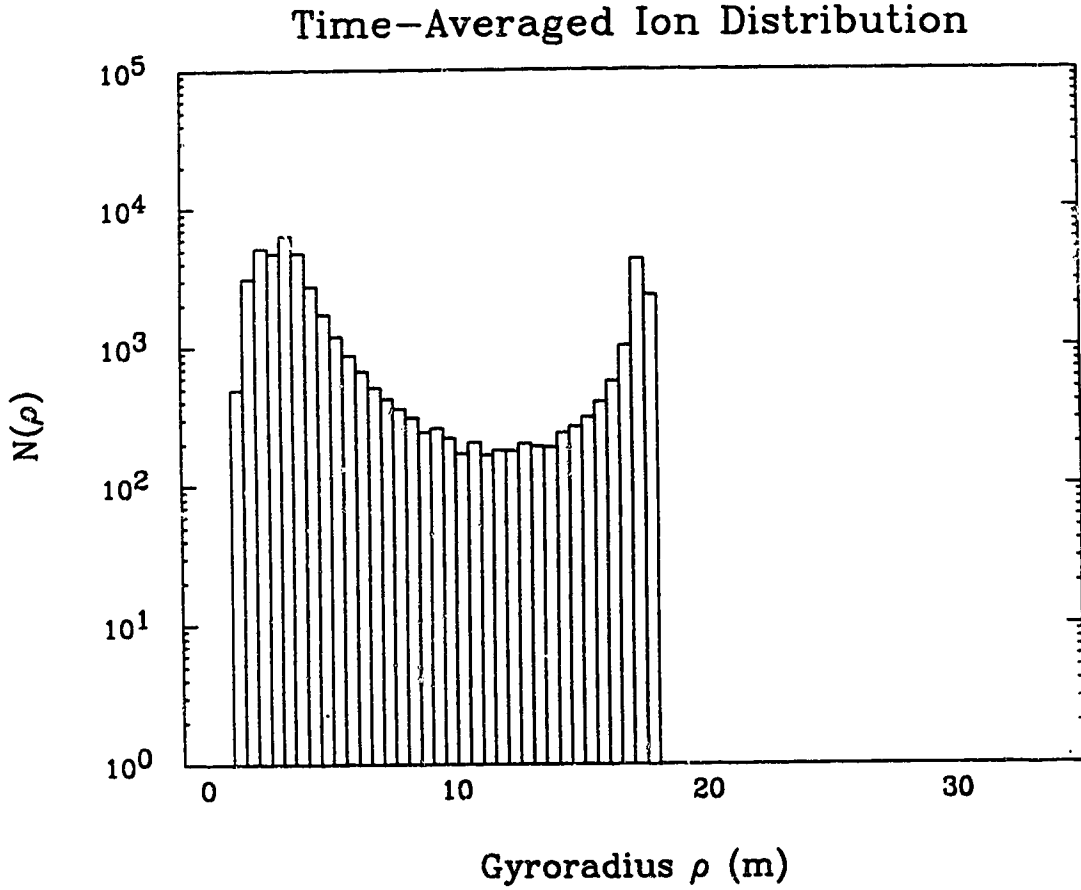


Figure G.5: Time-averaged ion distribution $N(\rho)$ versus gyroradius ρ for the Hamiltonian (3.2). Ten ions in the field of a single ($N = 1$) wave are averaged over the interval $200\pi \leq T \leq 2000\pi$. The wave parameters are $\epsilon_1 = 1$ m, $\nu_1 = 5$, $k_1 = 0.5 \text{ m}^{-1}$ and $\varphi_1 = 0$, and the integration parameter j is 25.

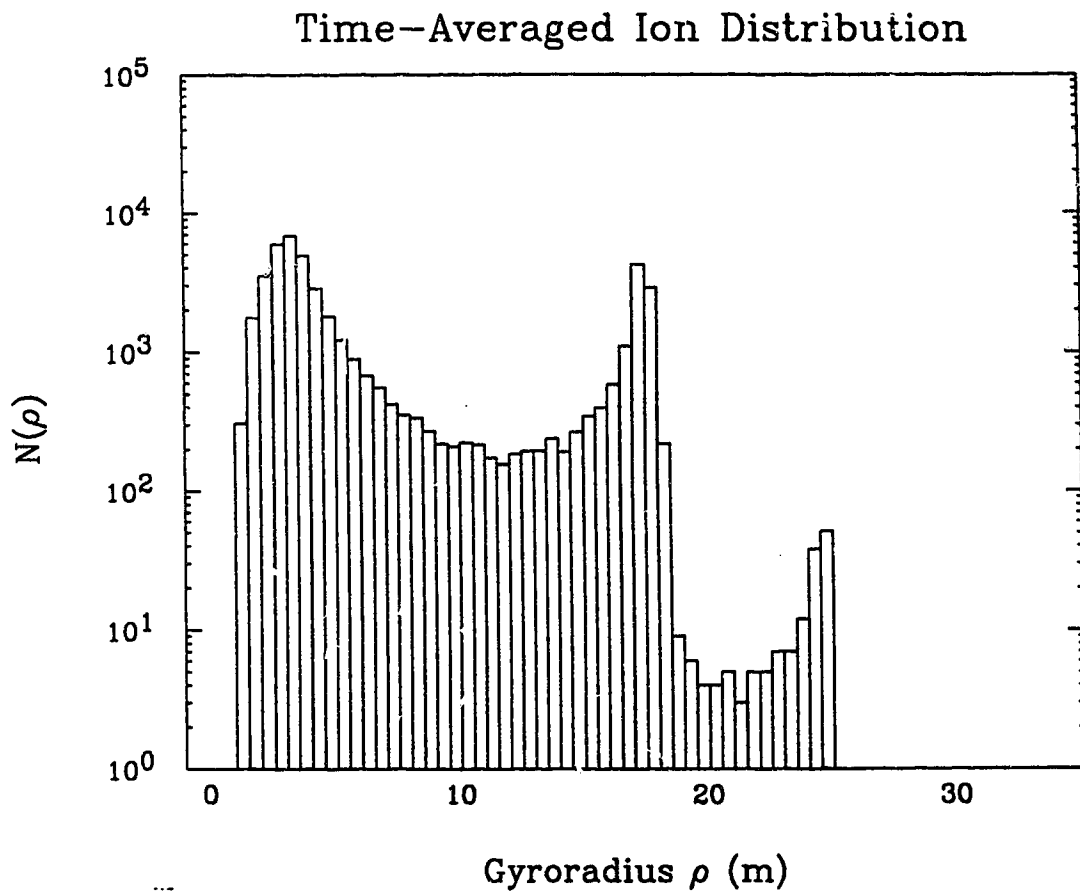


Figure G.6: Same as Figure G.5, except $\epsilon_1 = 1.5$ m.

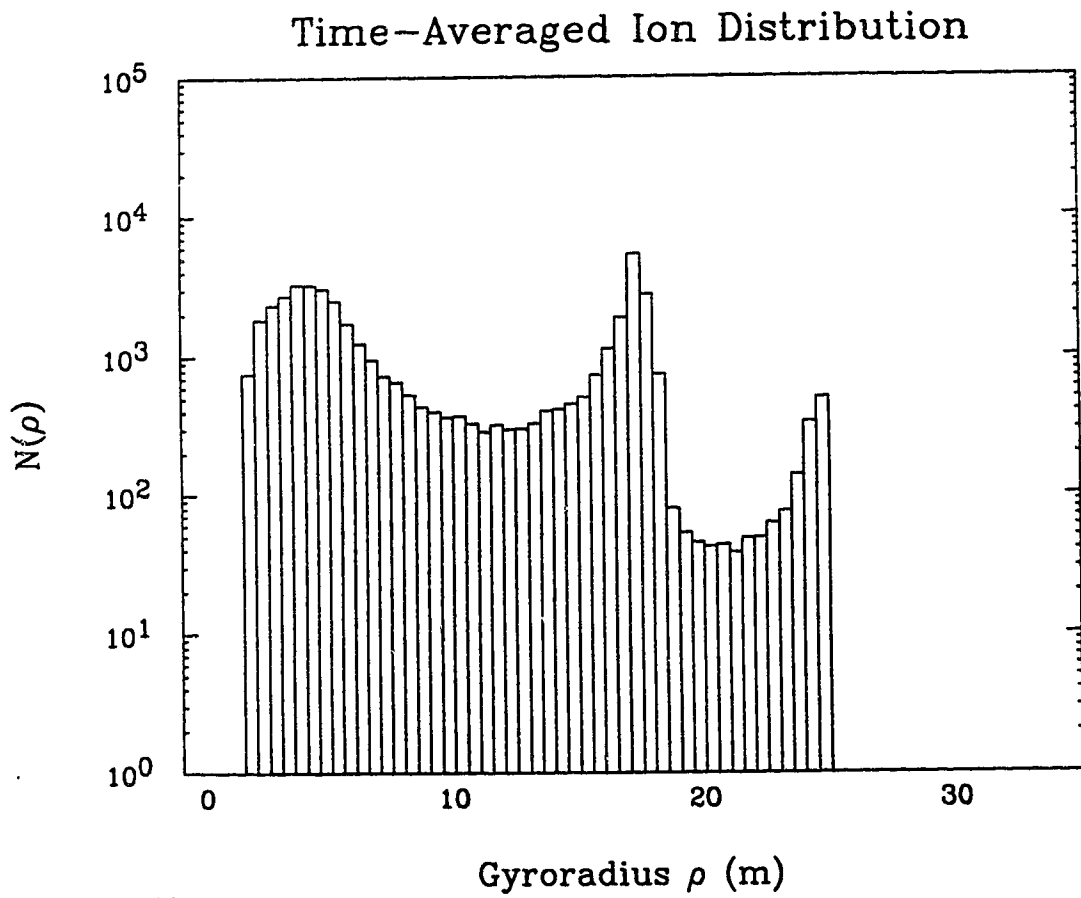


Figure G.7: Same as Figure G.5, except $\epsilon_1 = 2$ m.

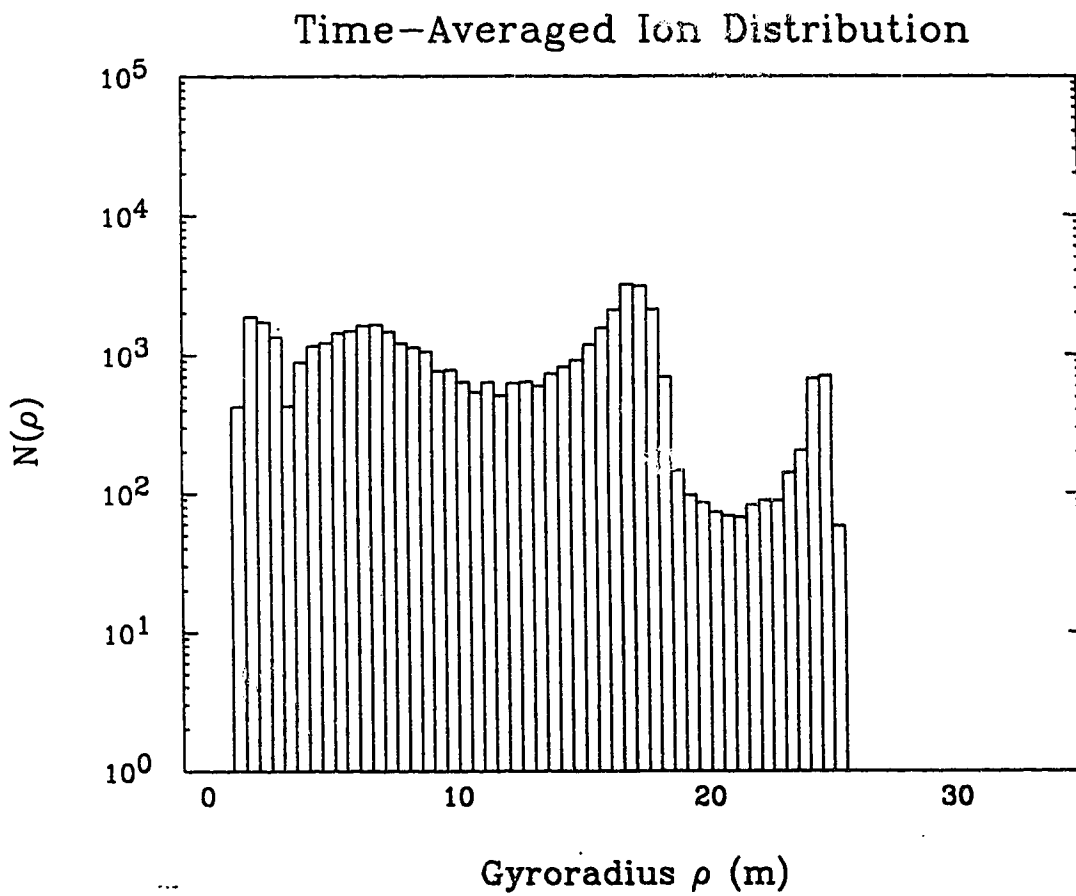


Figure G.8: Same as Figure G.5, except $\epsilon_1 = 2.5$ m.

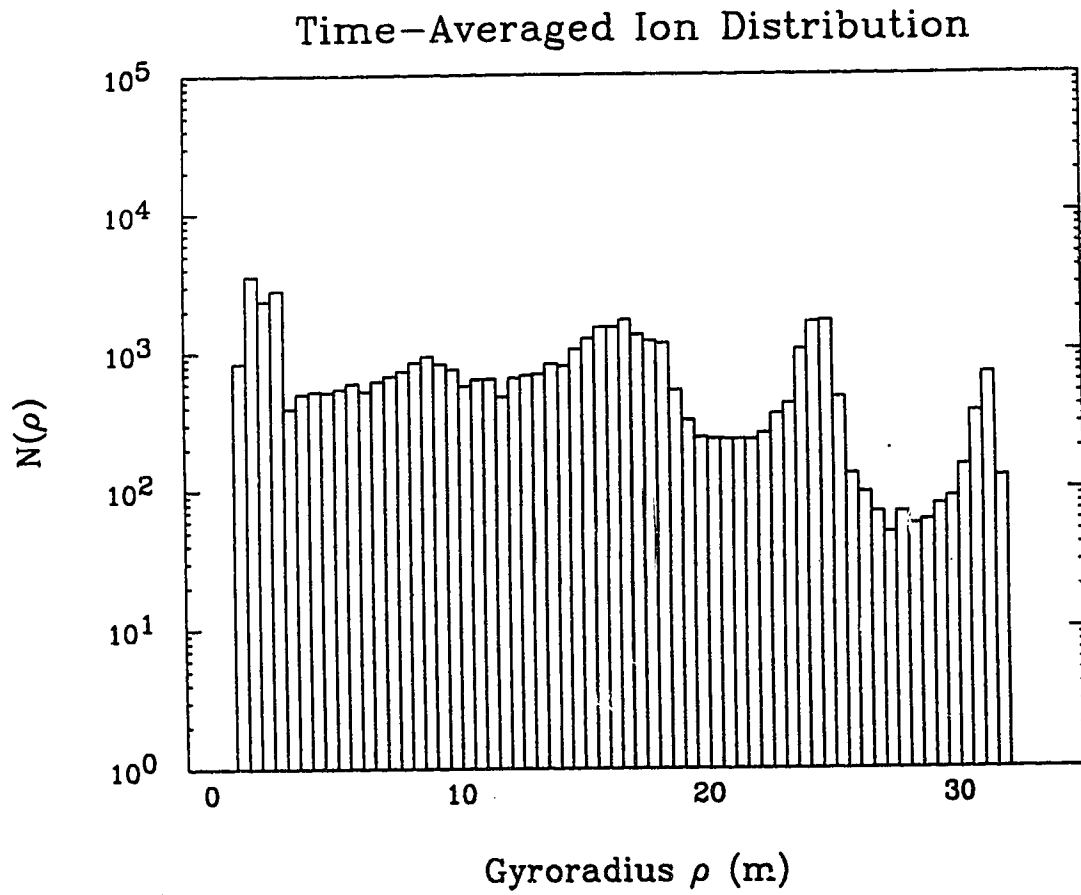


Figure G.9: Same as Figure G.5, except $\epsilon_1 = 3$ m.

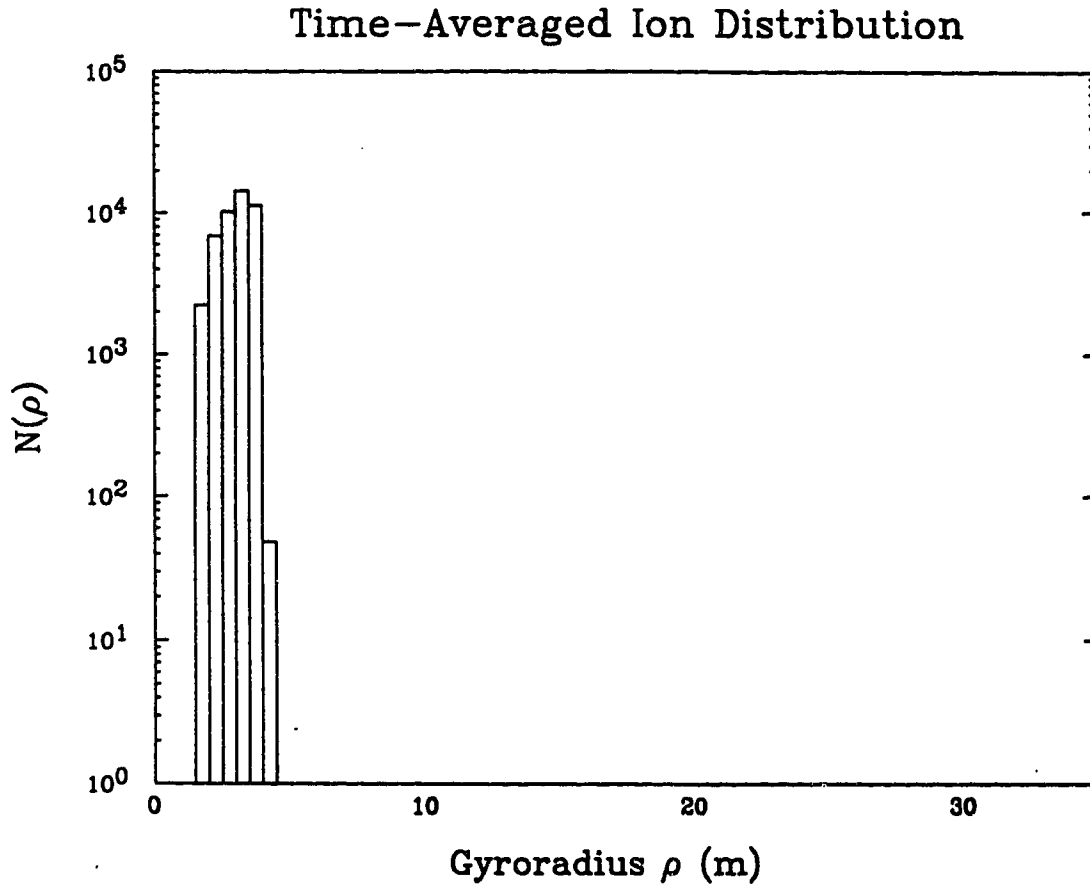


Figure G.10: Time-averaged ion distribution $N(\rho)$ versus gyroradius ρ for the Hamiltonian (3.2). Ten ions in the field of a single ($N = 1$) wave are averaged over the interval $200\pi \leq T \leq 2000\pi$. The wave parameters are $\epsilon_1 = 1$ m, $\nu_1 = 5.16$, $k_1 = 0.5 \text{ m}^{-1}$ and $\varphi_1 = 0$, and the integration parameter j is 25.

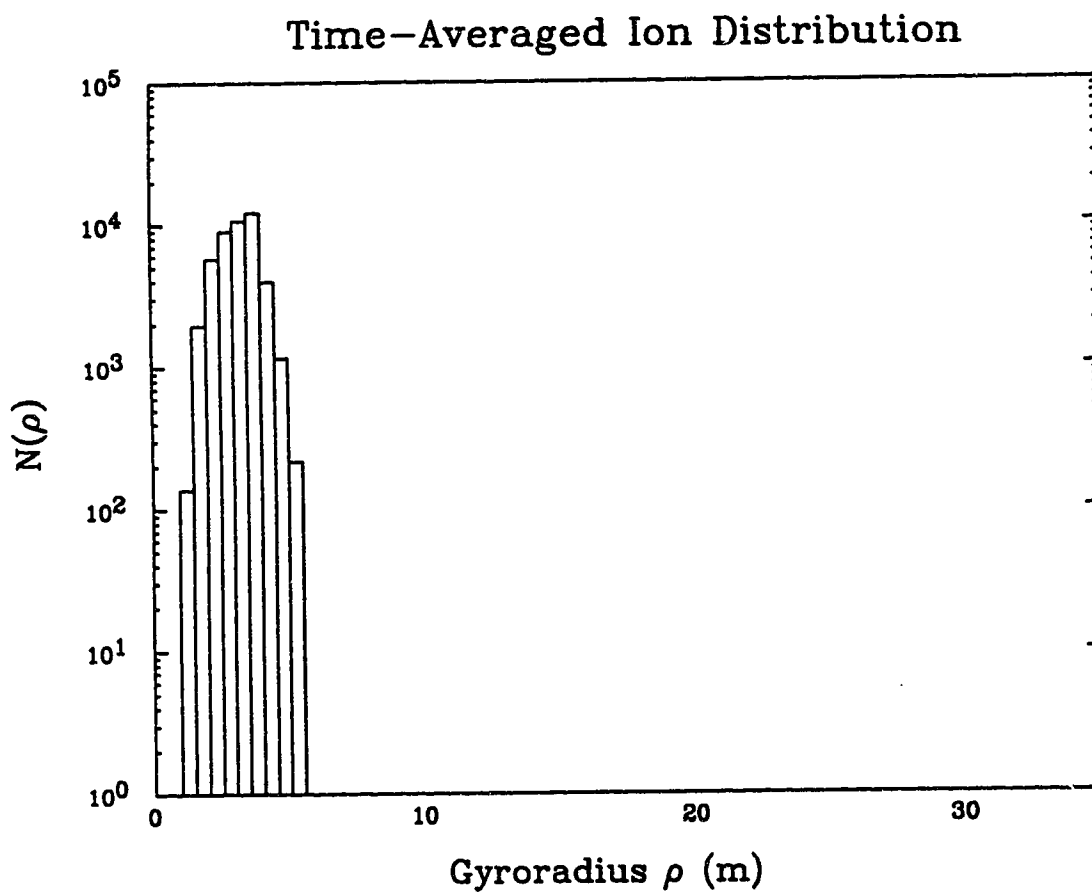


Figure G.11: Same as Figure G.10, except $\epsilon_1 = 3$ m.

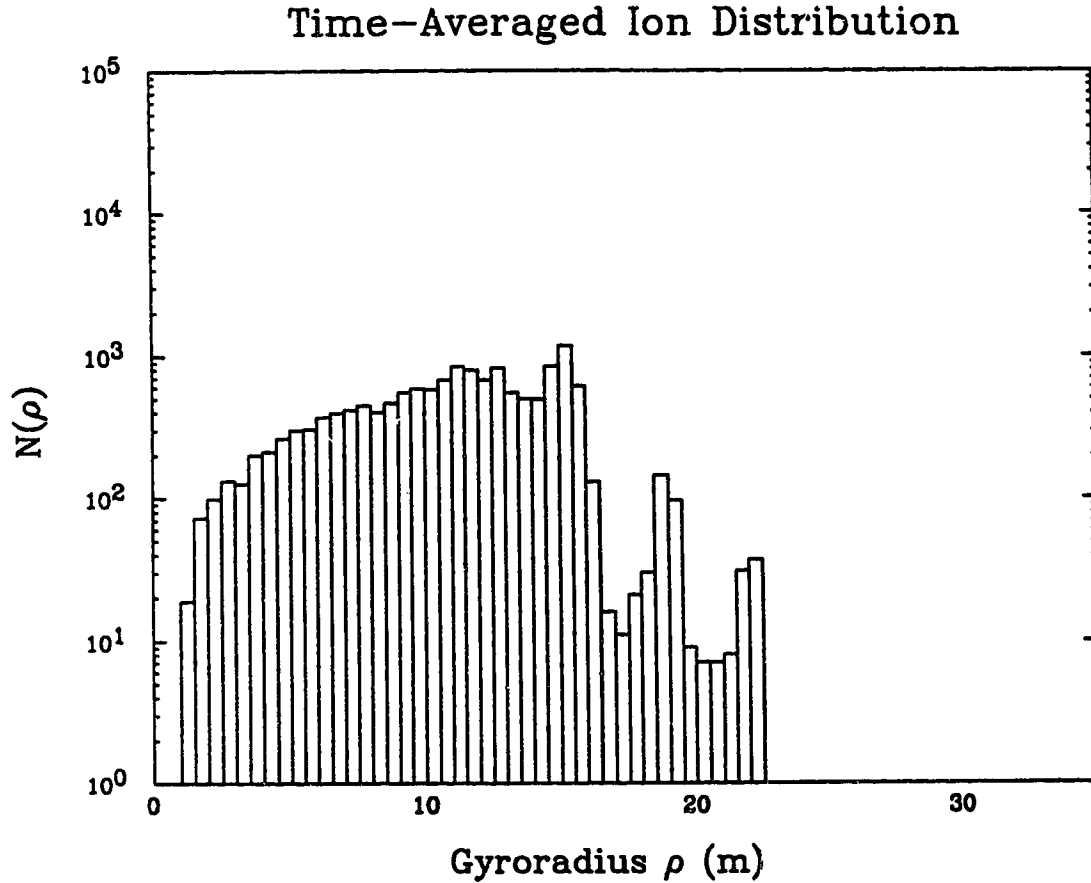


Figure G.12: Time-averaged ion distribution $N(\rho)$ versus gyroradius ρ for the Hamiltonian (3.2). One ion in the field of a single ($N = 1$) wave is averaged over the interval $200\pi \leq T \leq 6000\pi$. The wave parameters are $\epsilon_1 = 3$ m, $\nu_1 = 5$, $k_1 = 1 \text{ m}^{-1}$ and $\varphi_1 = 0$, and the integration parameter j is 20.

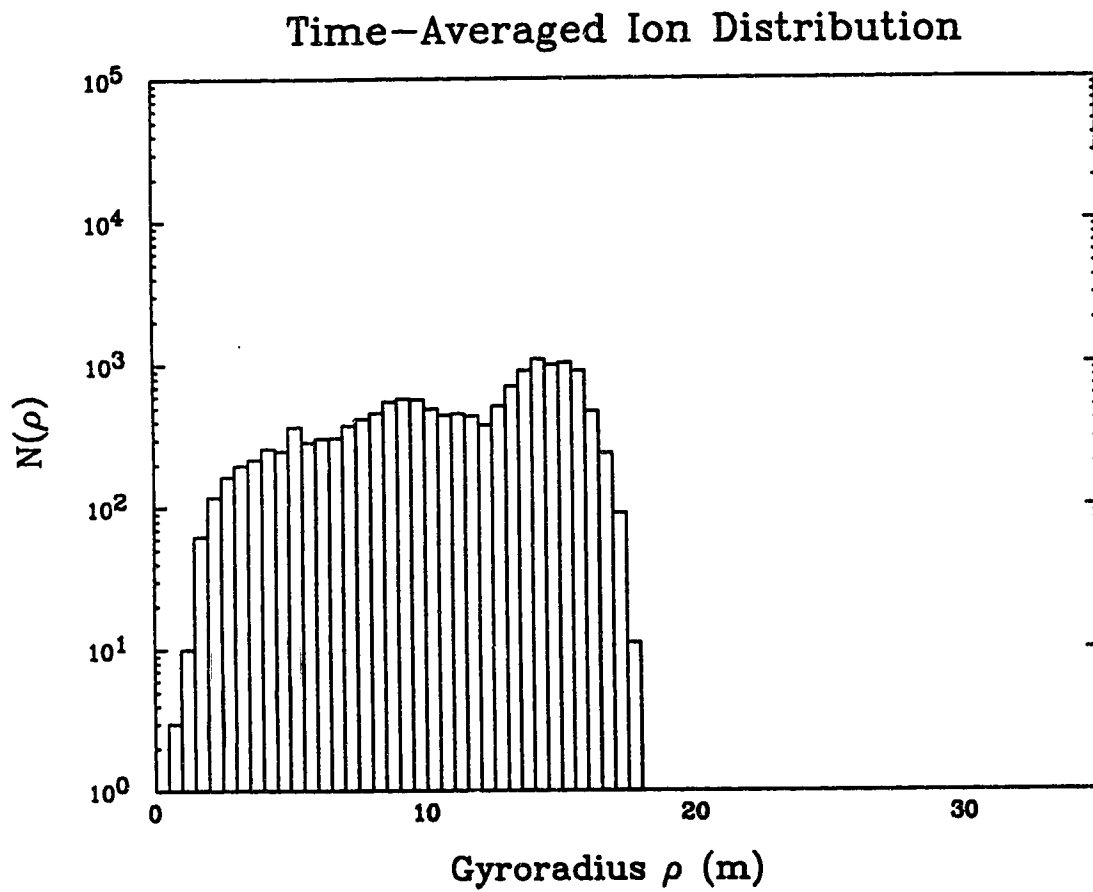


Figure G.13: Same as Figure G.12, except $\nu_1 = 5.16$ m.

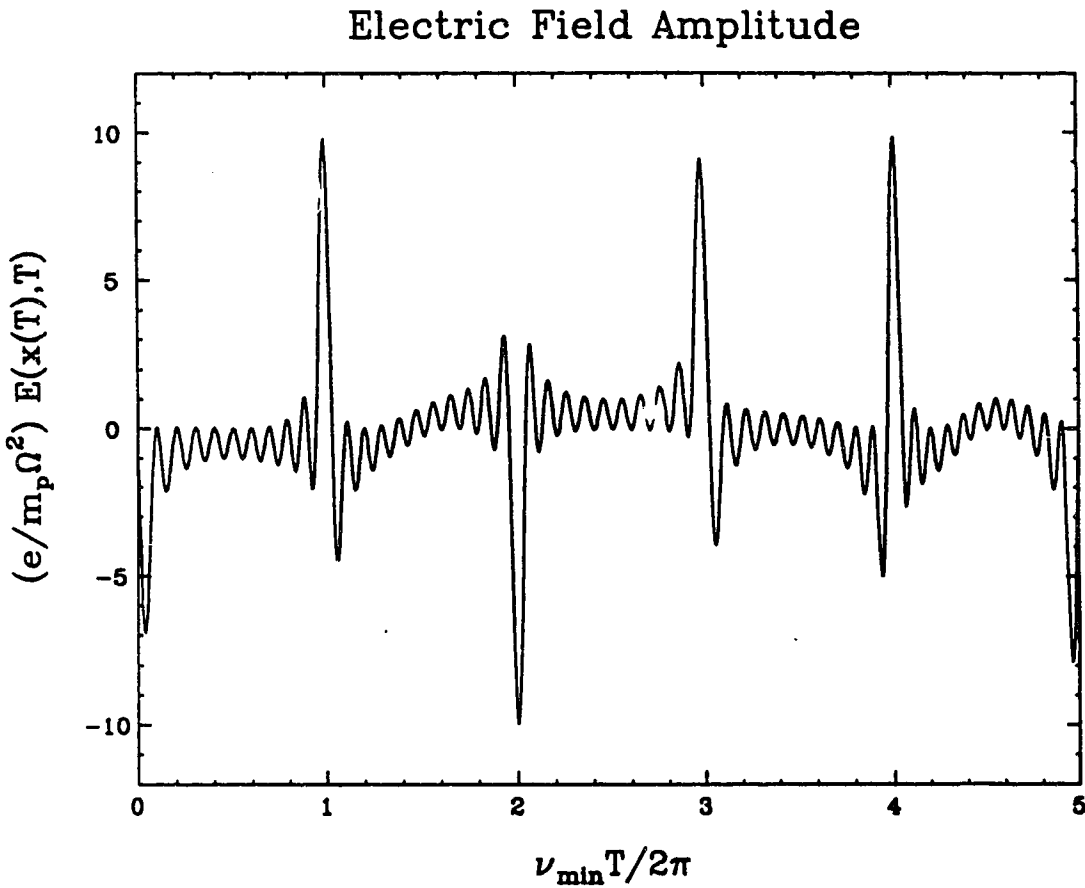


Figure G.14: The normalized electric field $\mathcal{E}(x(T), T)$ as seen by a particle in the field of 10 waves. The wave parameters are $\epsilon_i = 1 \text{ m}$, $\nu_i = 3i$, $k_i = 1 \text{ m}^{-1}$ and $\varphi_i = 0$ for $i = 1, \dots, 10$. The horizontal axis shows the number of spatial periods of the slowest wave, and integration parameter j is 20.

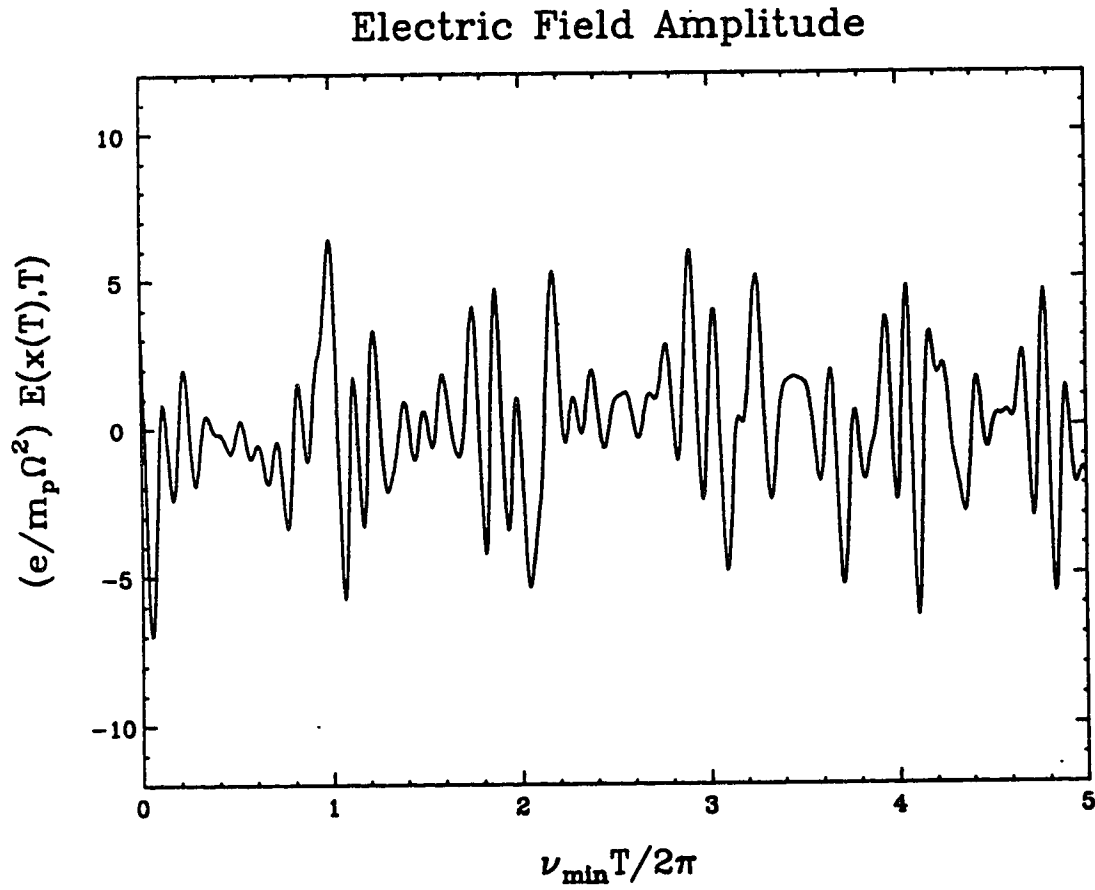


Figure G.15: The normalized electric field $\mathcal{E}(x(T), T)$ as seen by a particle in the field of 10 waves. The wave parameters are $\epsilon_i = 1$ m, with ν_i , k_i and φ_i chosen at random for $i = 1, \dots, 10$. The horizontal axis shows the number of spatial periods of the slowest wave, and integration parameter j is 20.

APPENDIX H
TABLES AND FIGURES (CONT'D)

...

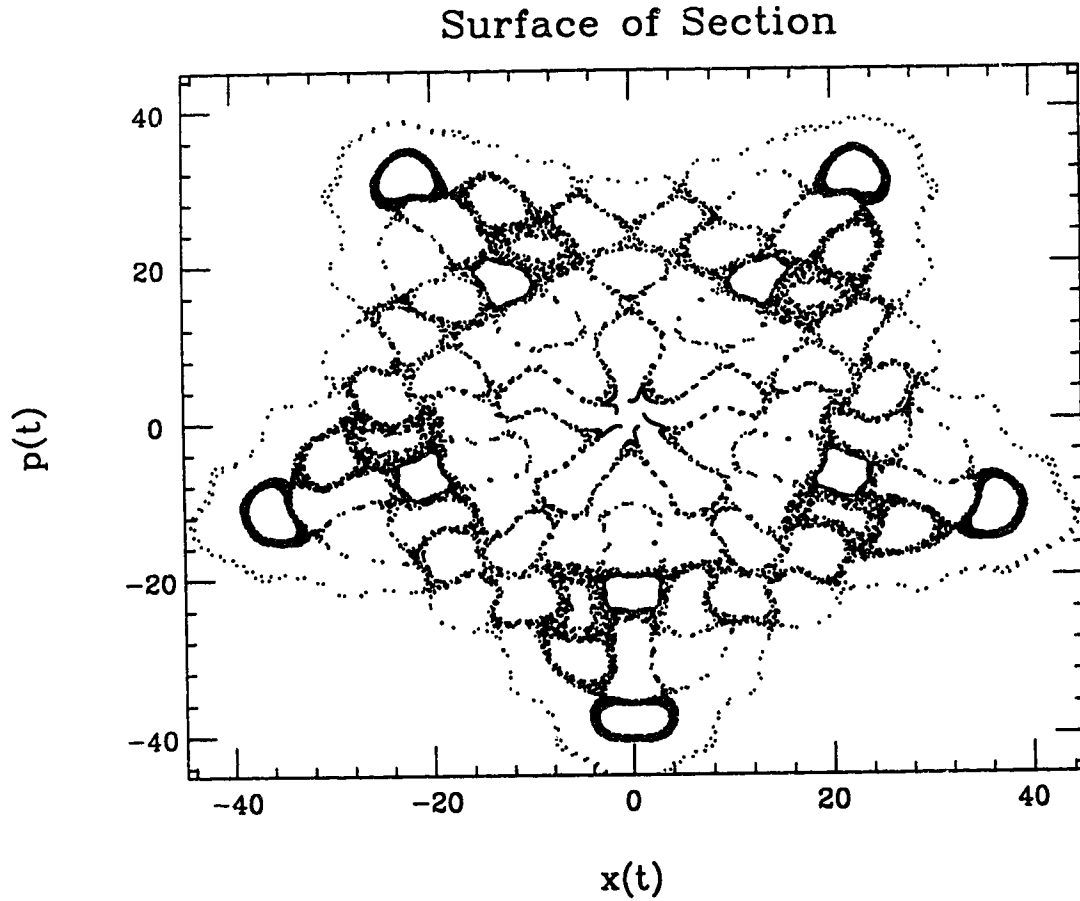


Figure H.1: Surface of section of the Hamiltonian (3.2) for $N = 4$. The wave parameters are $\epsilon_i = 1.75$ m, $\nu_i = 5i$, $k_i = 0.7$ m $^{-1}$ and $\varphi_i = 0$ for $i = 1, \dots, 4$. Points are plotted at the times $T_p = 2\pi p/\nu_1$, for $p = 1, \dots, 15000$. The initial gyroradius is 2.5 m, and the integration parameter $j = 17.5$ is not an integer in this special case.

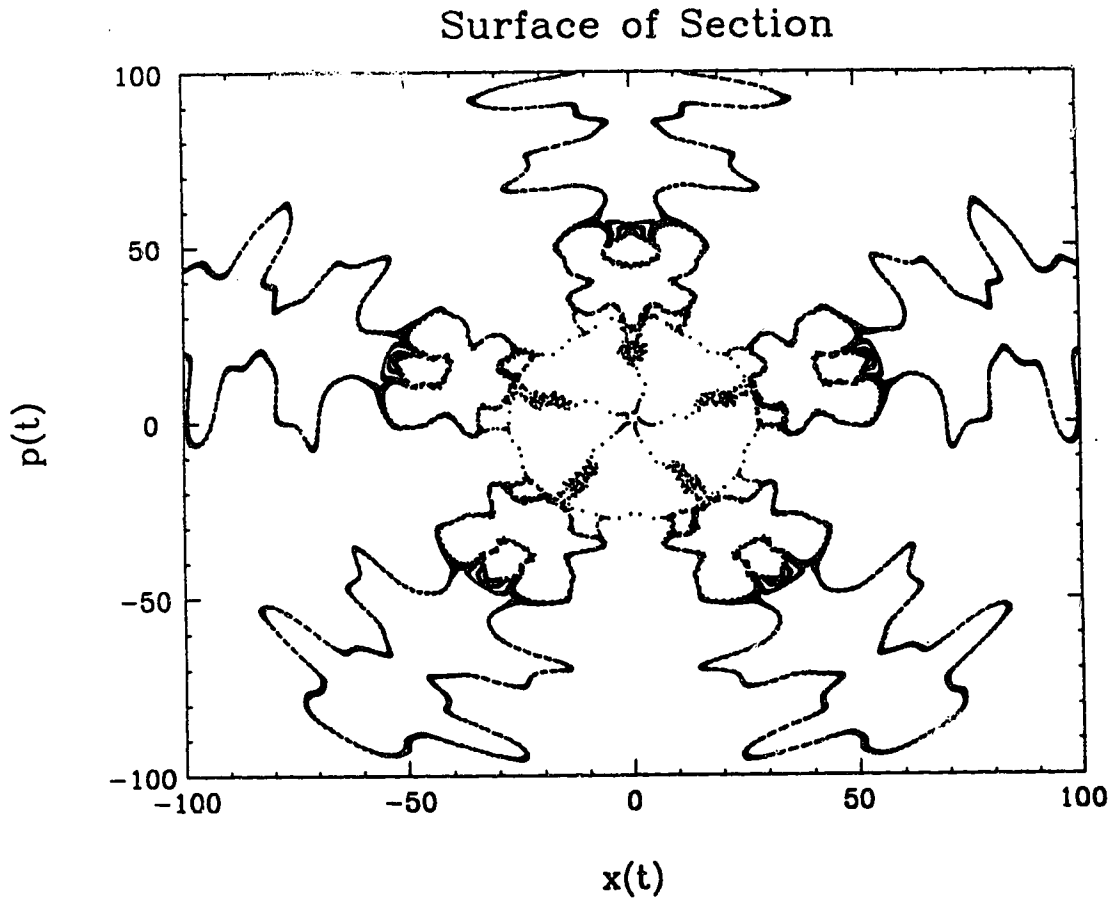


Figure H.2: Surface of section of the Hamiltonian (3.2) for $N = 5$. Wave parameters are $\epsilon_i = 1.8$ m, $(\nu_1, \dots, \nu_5) = (5, 10, 10, 15, 15)$, $(k_1, \dots, k_5) = (0.7, 0.75, 0.55, 0.7, 0.35)$ m $^{-1}$ and $\varphi_i = 0$ for $i = 1, \dots, 5$. Points are plotted at the times $T_p = 2\pi p/\nu_1$, for $p = 1, \dots, 15000$. The initial gyroradius is 2.6 m, and the integration parameter is $j = 22$.

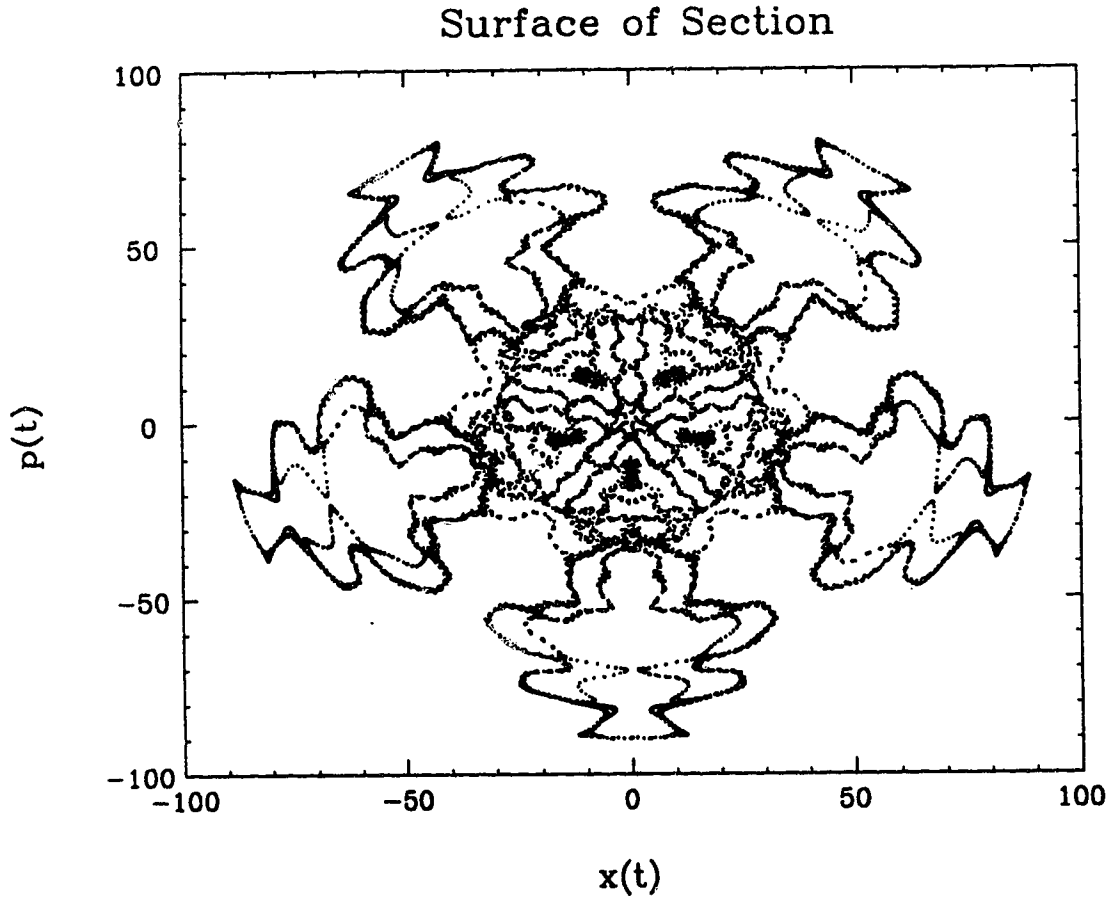


Figure H.3: Surface of section of the Hamiltonian (3.2) for $N = 6$. Wave parameters are $\epsilon_i = 1.8$ m, $(\nu_1, \dots, \nu_6) = (5, 10, 10, 15, 15, 20)$, $(k_1, \dots, k_6) = (0.7, 0.75, 0.55, 0.7, 0.35, 0.7)$ m⁻¹ and $\varphi_i = 0$ for $i = 1, \dots, 6$. Points are plotted at the times $T_p = 2\pi p/\nu_1$, for $p = 1, \dots, 15000$. The initial gyroradius is 2.6 m, and the integration parameter $j = 17.5$ is not an integer in this special case.

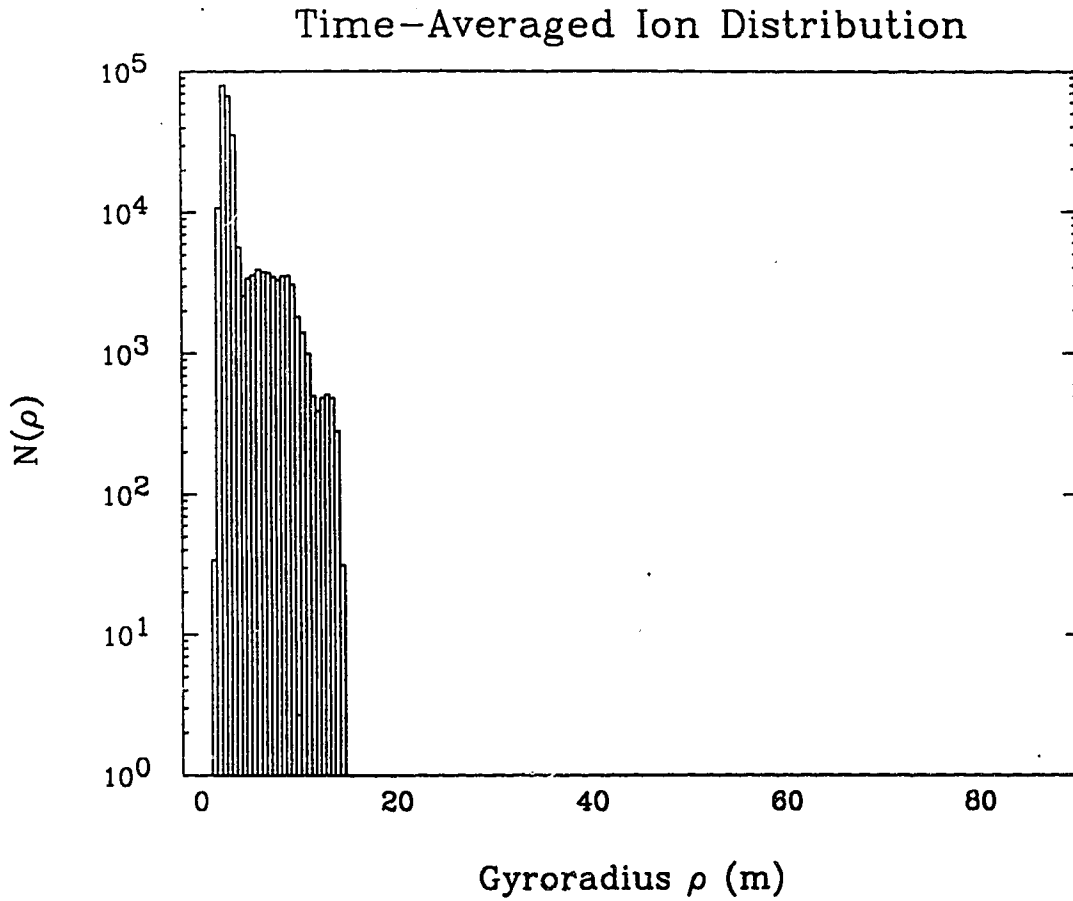


Figure H.4: Time-averaged ion distribution $N(\rho)$ versus gyroradius ρ for the Hamiltonian (3.2). Ten ions in the field of ten waves are averaged over the interval $200\pi \leq T \leq 2000\pi$. The wave parameters are chosen at random according to the prescriptions in the text (case A), with the mode amplitude range $[\epsilon_{min}, \epsilon_{max}] = [0, 1]$ m. The integration parameter j is 25.

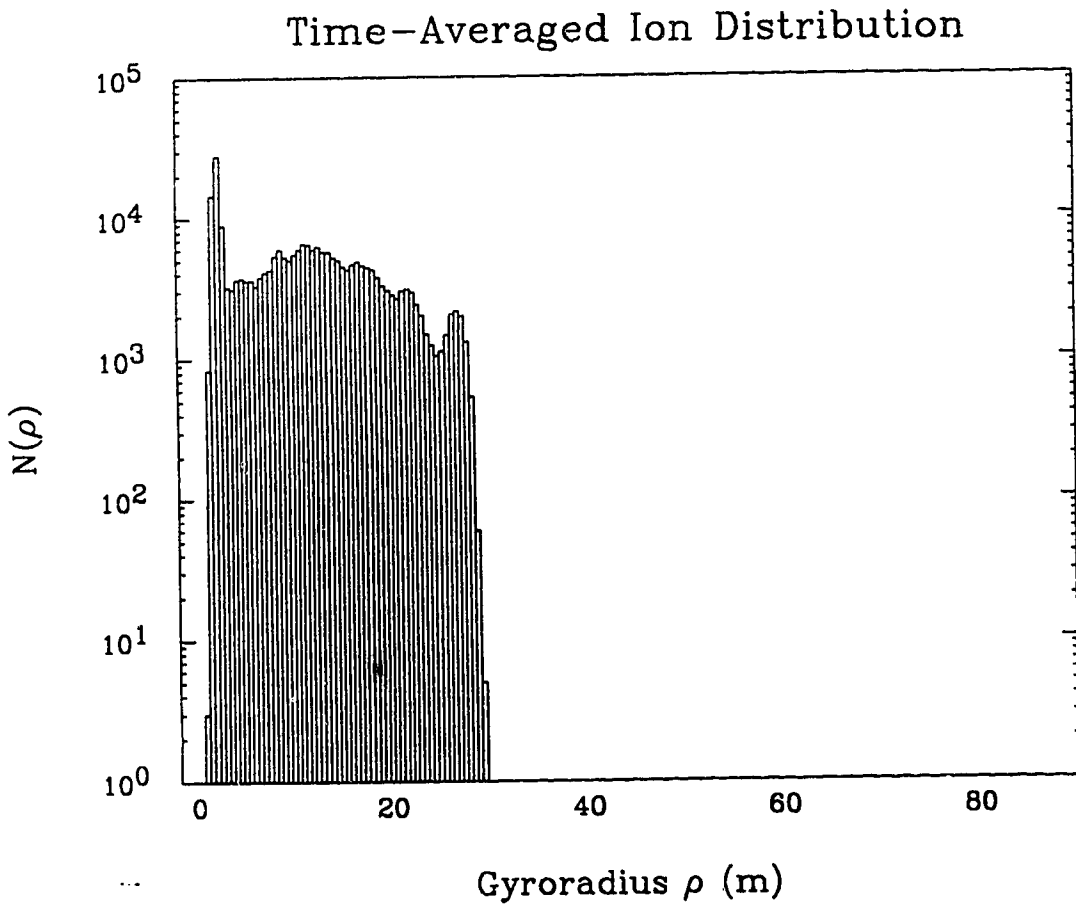


Figure H.5: Same as Figure H.4, except $[\epsilon_{min}, \epsilon_{max}] = [0.5, 1.5]$ m.

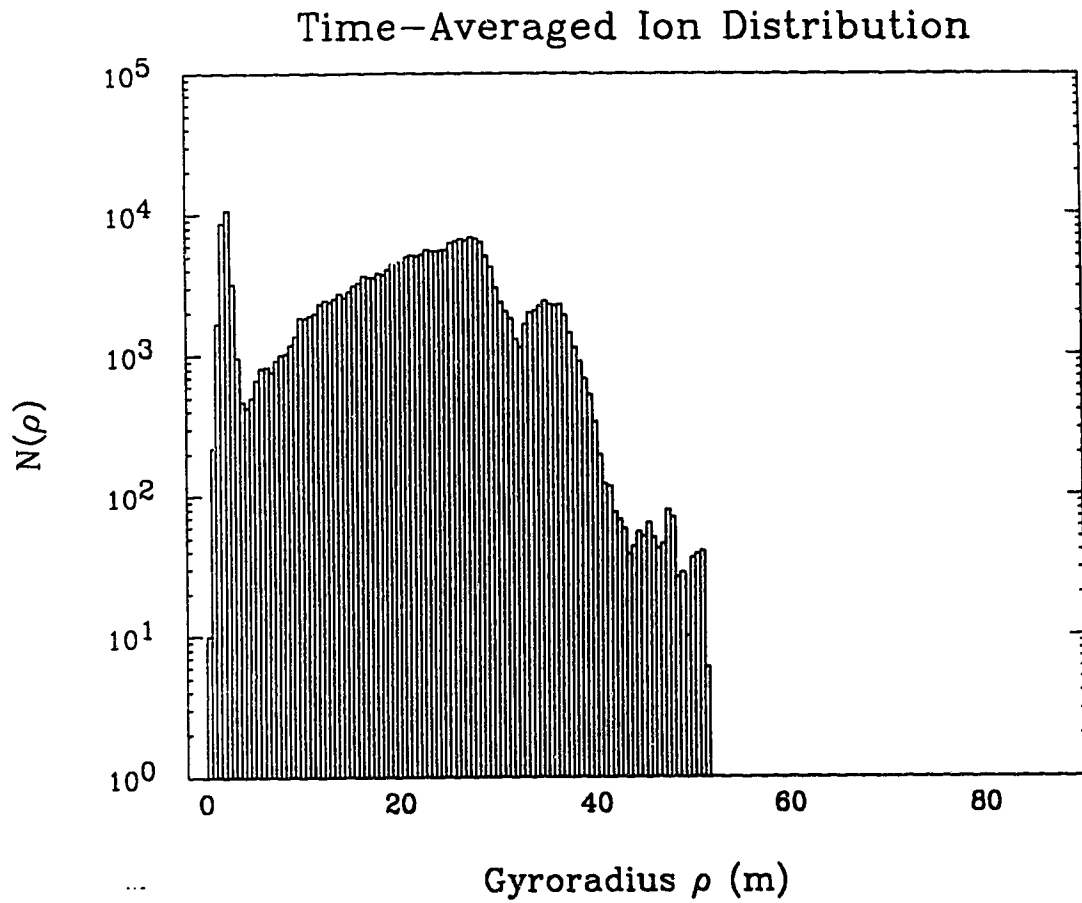


Figure H.6: Same as Figure H.4, except $[\epsilon_{min}, \epsilon_{max}] = [1, 2]$ m.

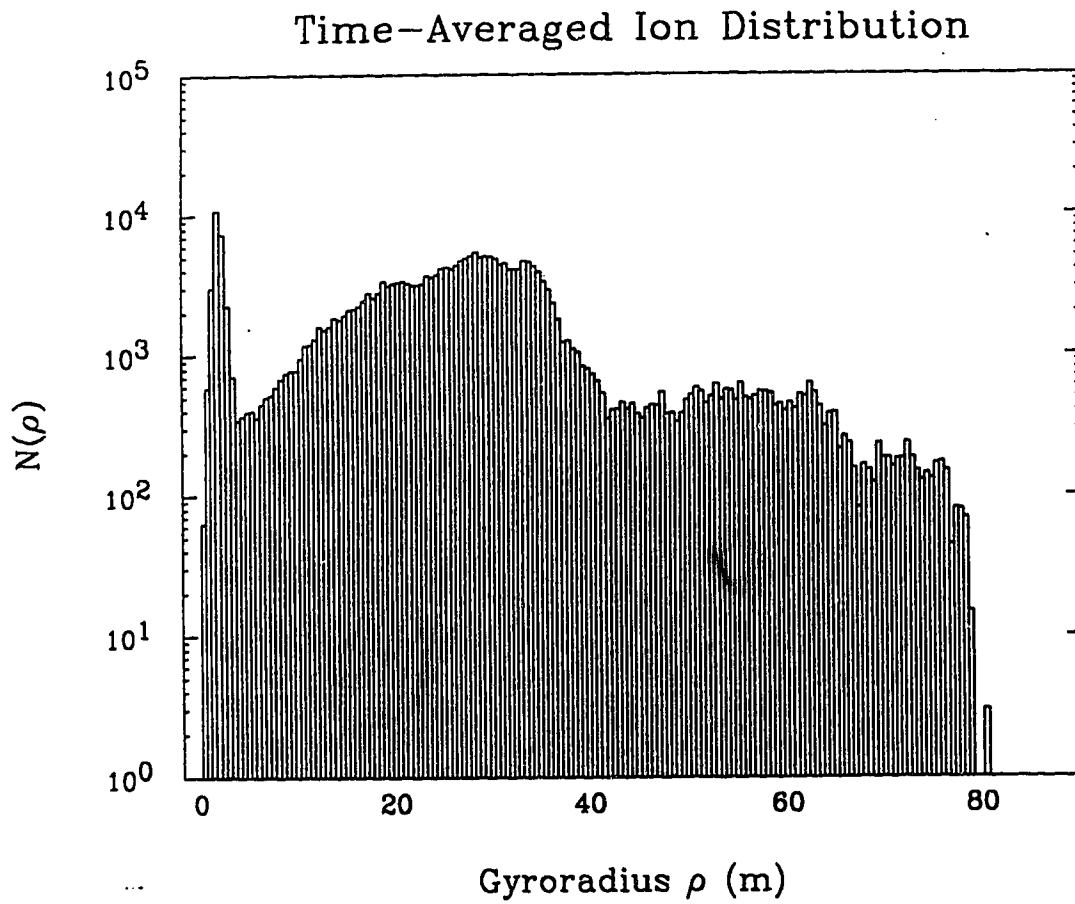


Figure H.7: Same as Figure H.4, except $[\epsilon_{min}, \epsilon_{max}] = [1.5, 2.5]$ m.

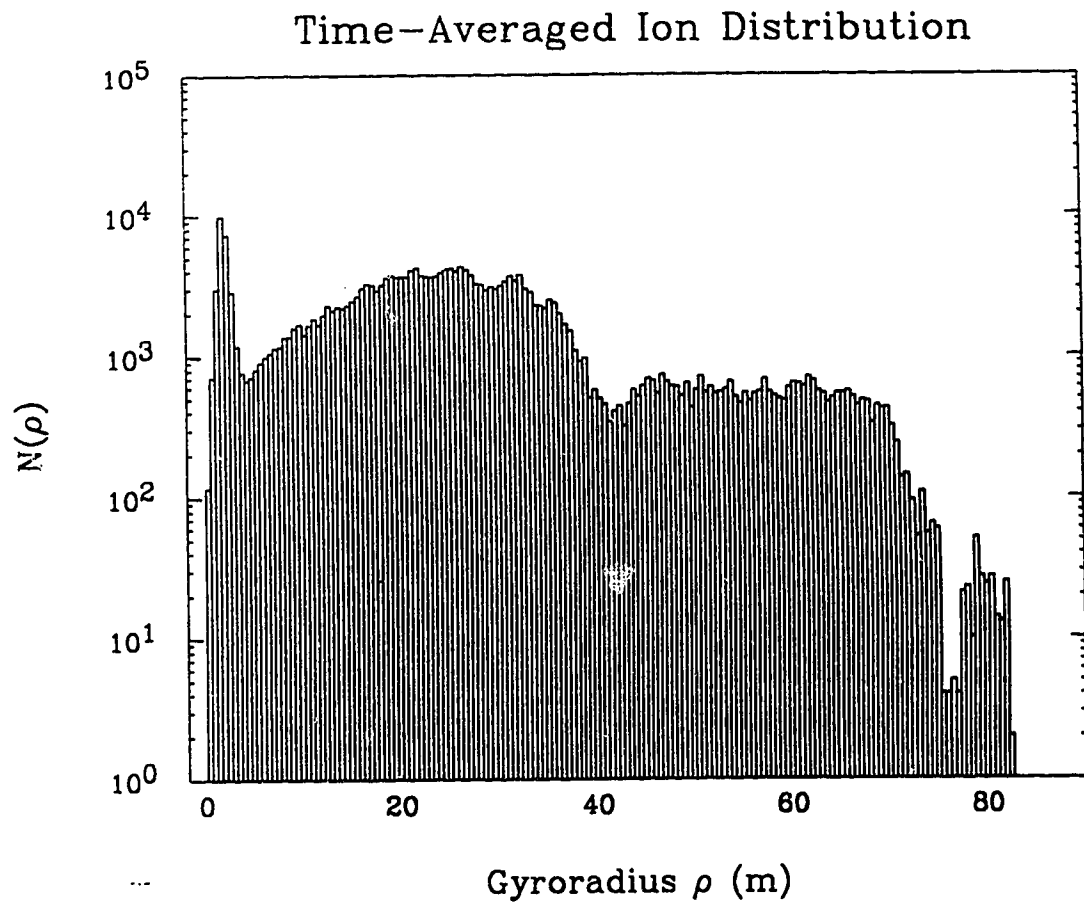


Figure H.8: Same as Figure H.4, except $[\epsilon_{min}, \epsilon_{max}] = [2, 2.5]$ m.

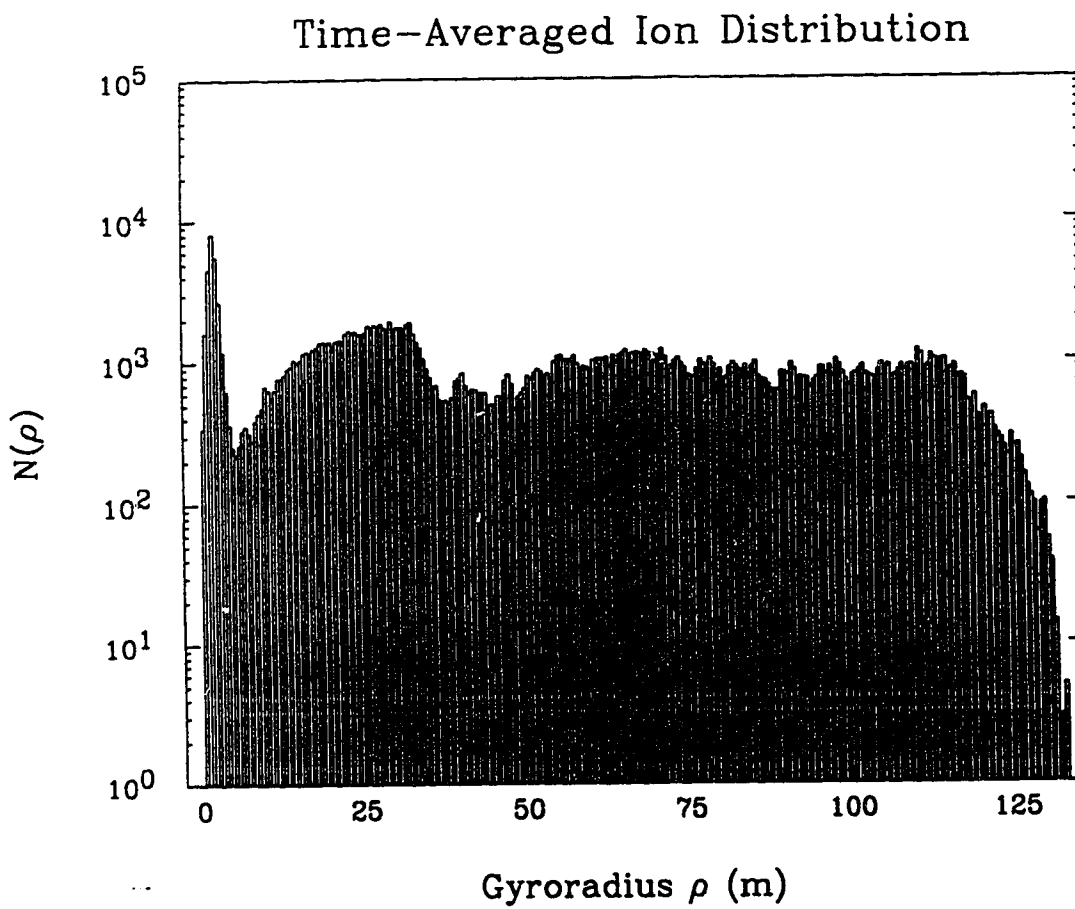


Figure H.9: Same as Figure H.4, except $[\epsilon_{min}, \epsilon_{max}] = [3, 3.5]$ m.

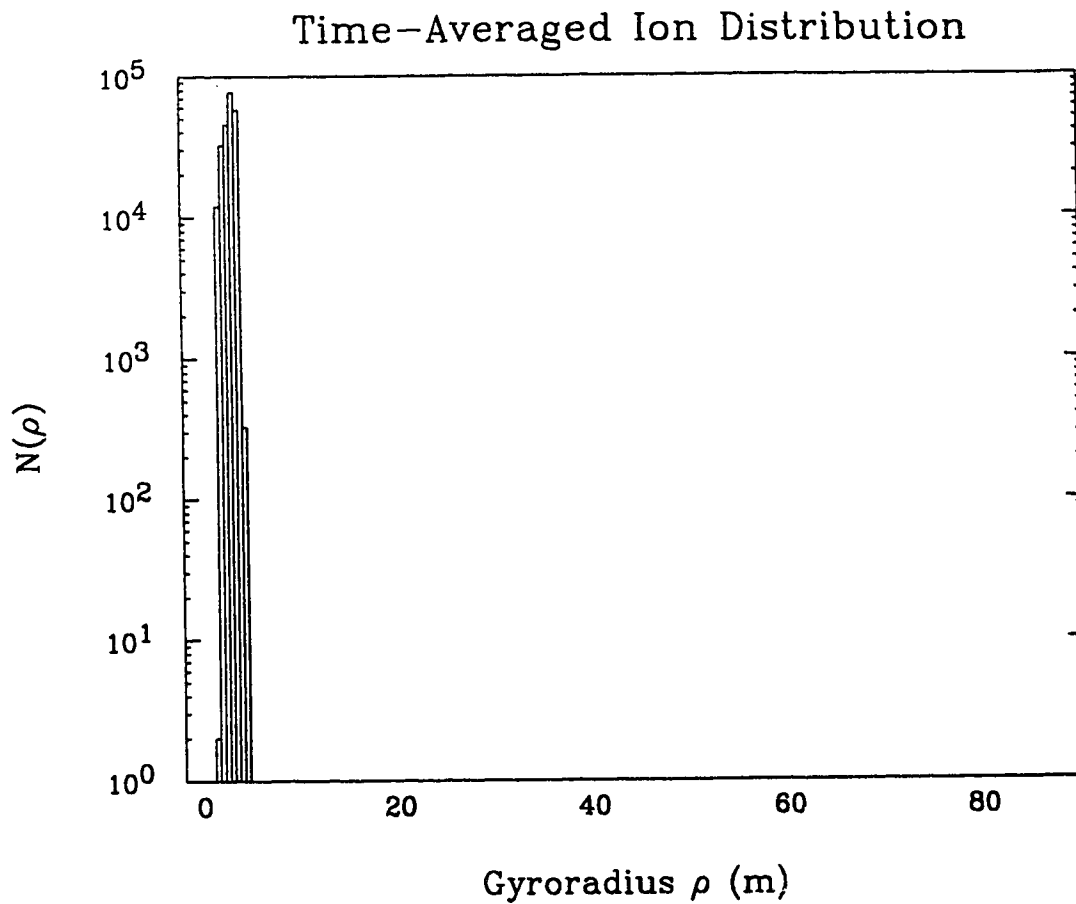


Figure H.10: Time-averaged ion distribution $N(\rho)$ versus gyroradius ρ for the Hamiltonian (3.2). Ten ions in the field of ten waves are averaged over the interval $200\pi \leq T \leq 2000\pi$. The wave parameters are chosen at random according to the prescriptions in the text (case B), with the mode amplitude range $[\epsilon_{min}, \epsilon_{max}] = [0, 1]$ m. The integration parameter j is 25.

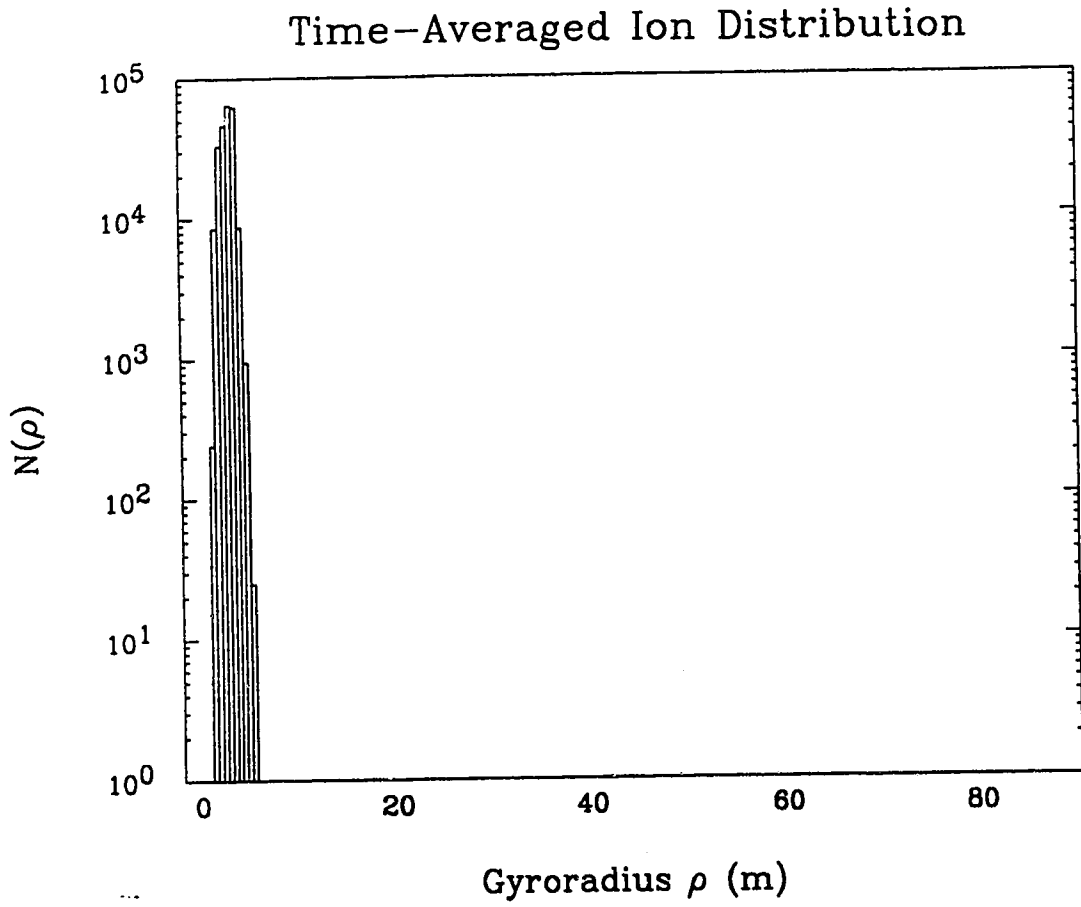


Figure H.11: Same as Figure H.10, except $[\epsilon_{min}, \epsilon_{max}] = [0.5, 1.5]$ m.

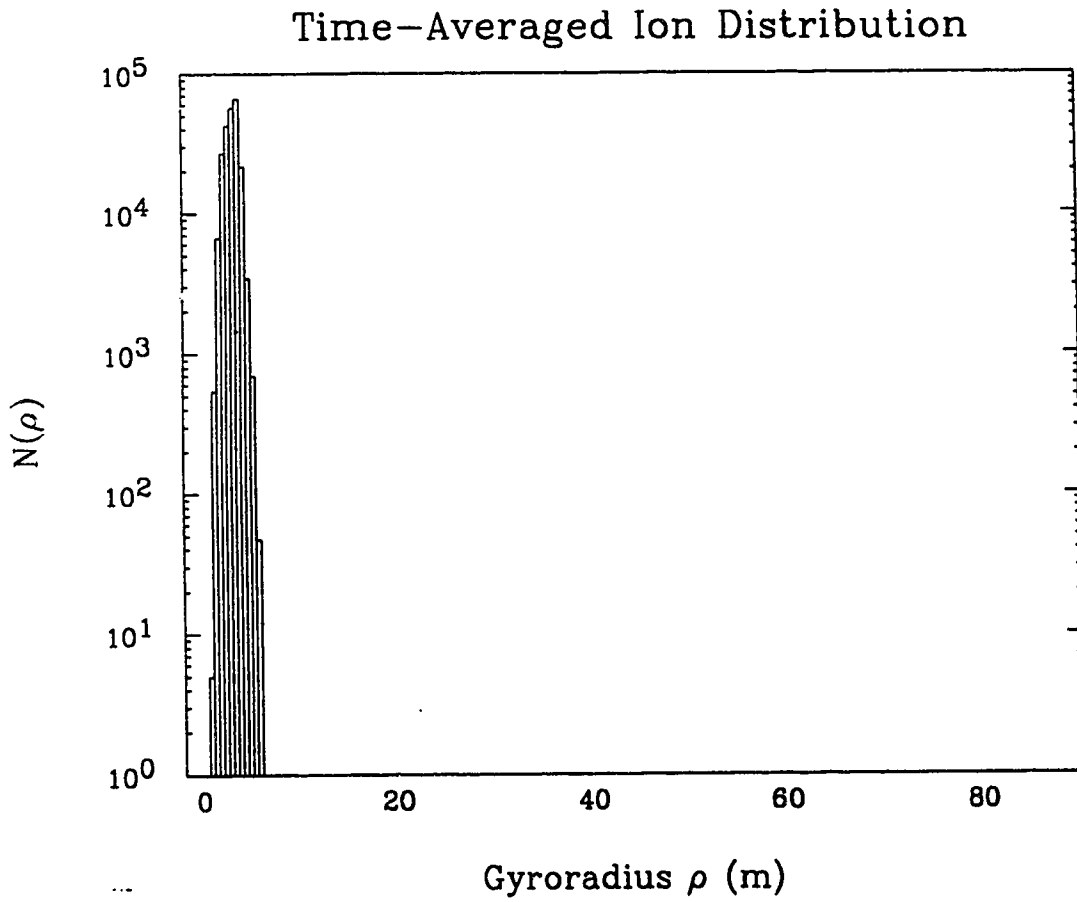


Figure H.12: Same as Figure H.10, except $[\epsilon_{min}, \epsilon_{max}] = [1, 2]$ m.

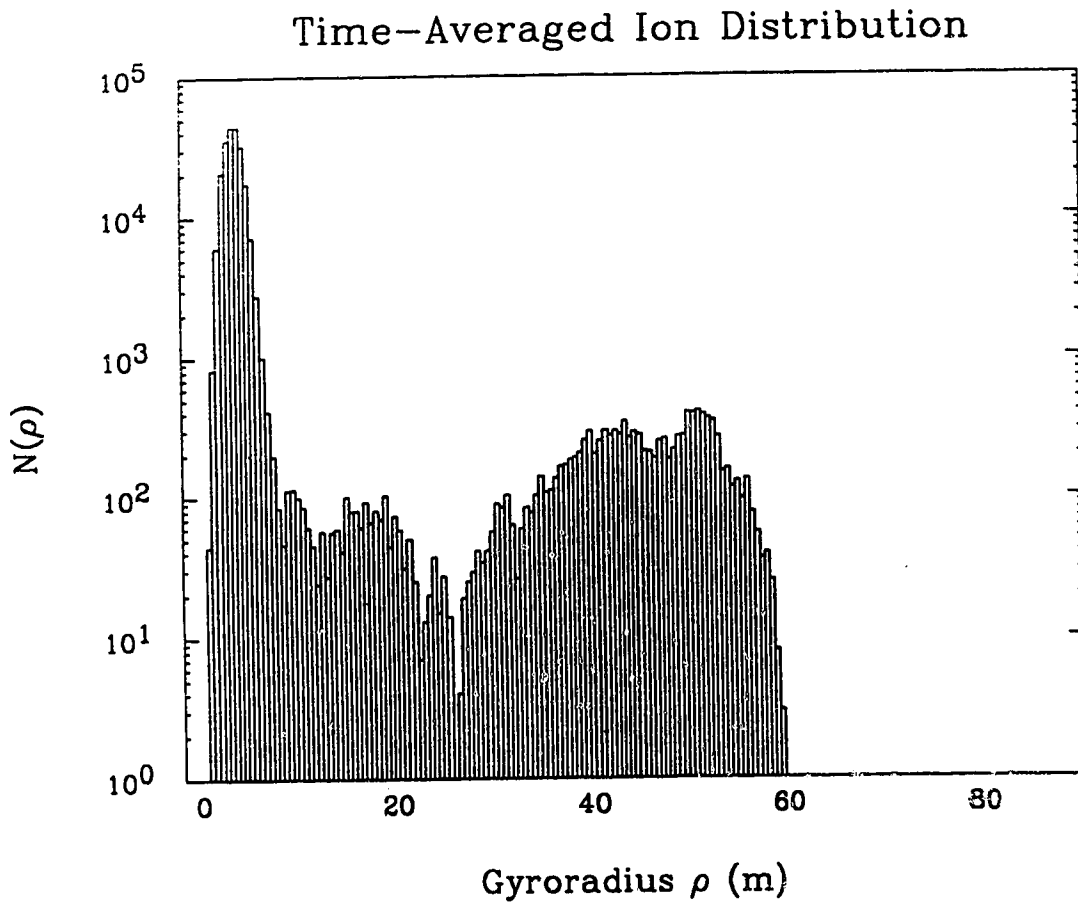


Figure H.13: Same as Figure H.10, except $[\epsilon_{min}, \epsilon_{max}] = [1.5, 2.5]$ m.

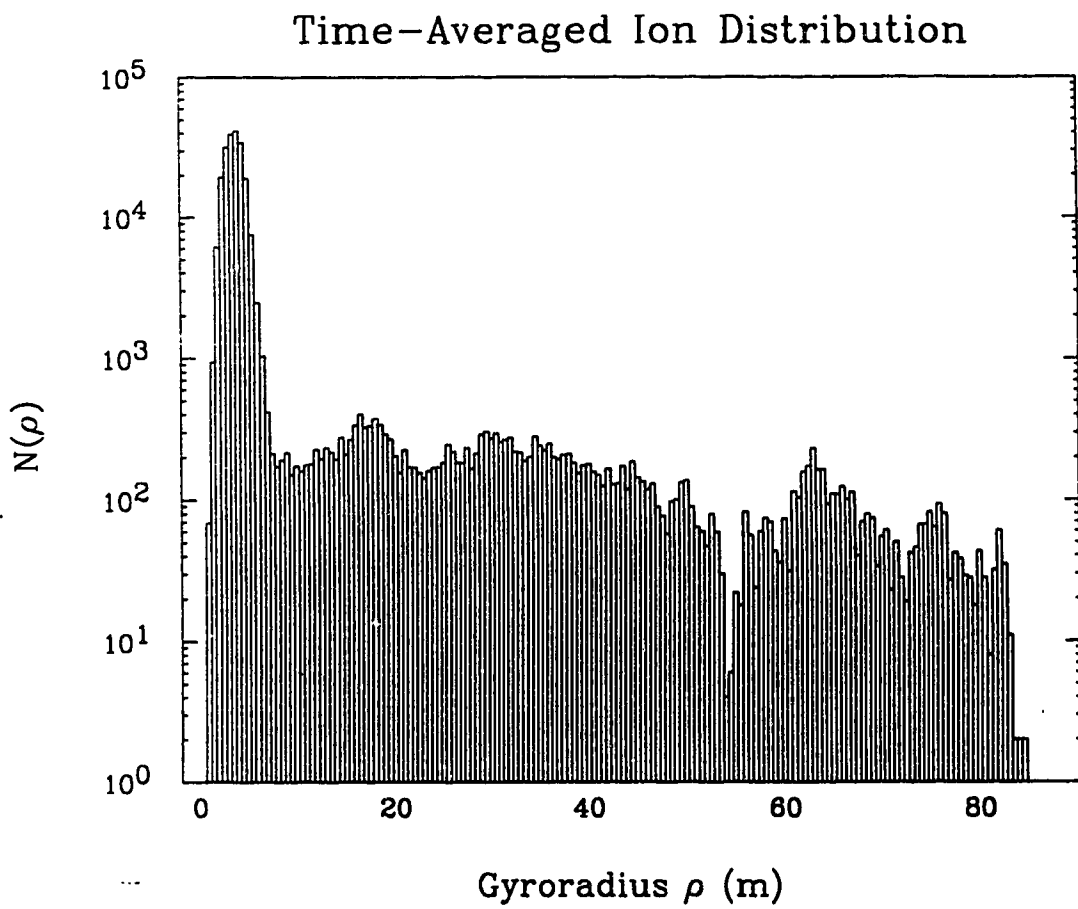


Figure H.14: Same as Figure H.10, except $\{\epsilon_{min}, \epsilon_{max}\} = [2, 2.5]$ m.

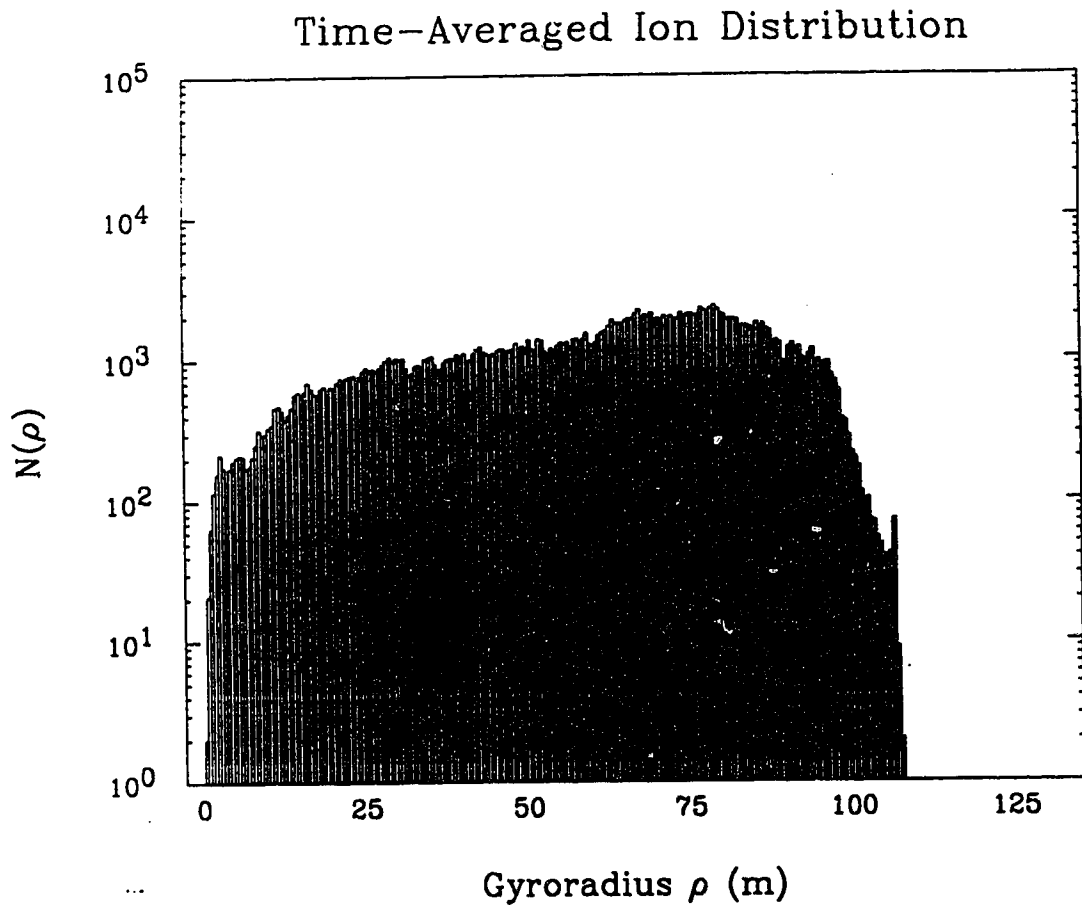


Figure H.15: Same as Figure H.10, except $[\epsilon_{min}, \epsilon_{max}] = [3, 3.5]$ m.

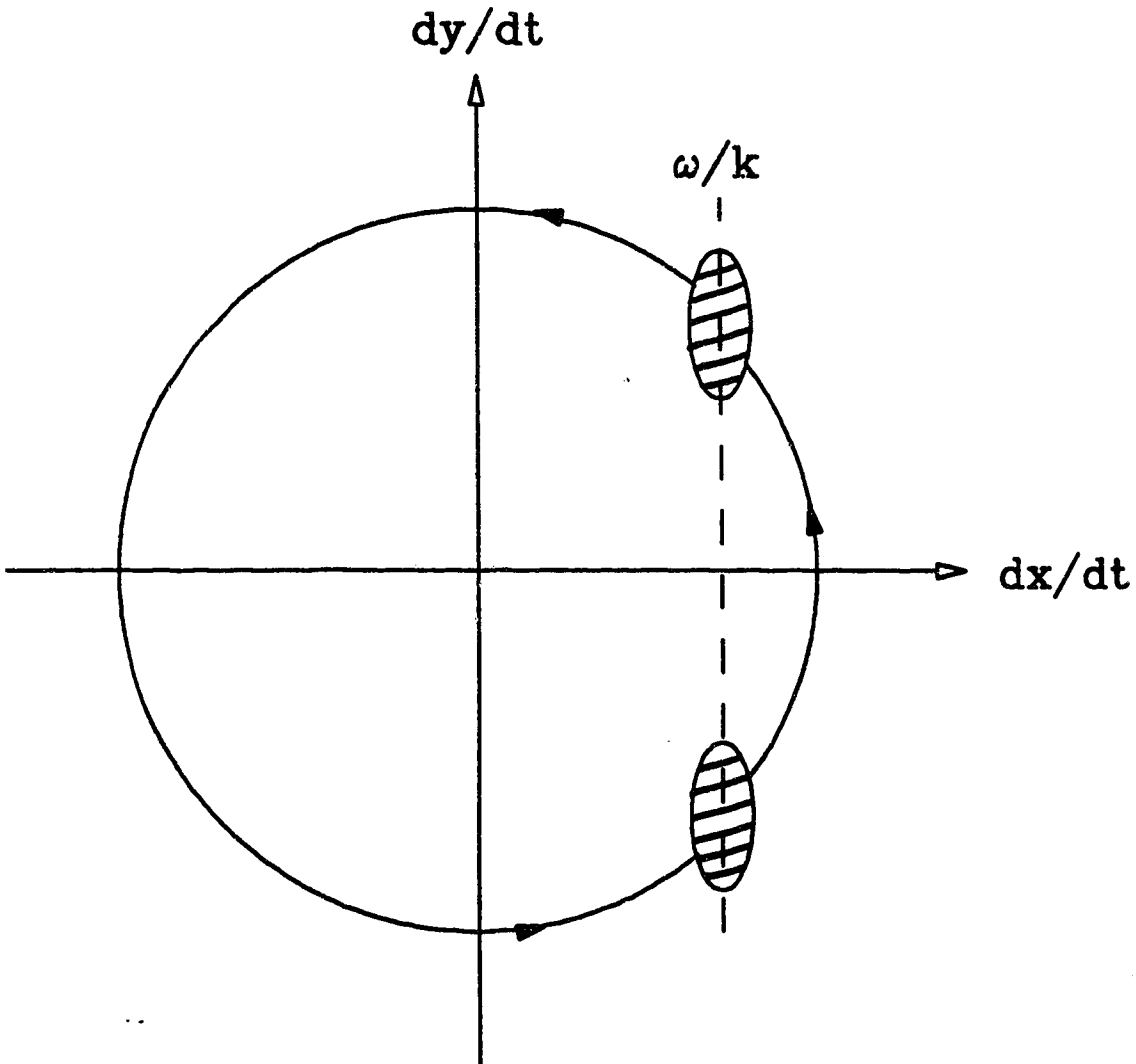


Figure H.16: Qualitative particle trajectory in the (\dot{x}, \dot{y}) phase plane for the Hamiltonian (1.2). In the oval regions, a resonant interaction occurs which may lead to a substantial phase change and thus to stochastic particle dynamics. This effect weakens as the gyroradius of a particular trajectory increases.

Summary of Turbulent Spectrum Heating Simulations.

Run	Wave Parameters	$\epsilon_{min} - \epsilon_{max}$ (m)	ρ_{max} (m)	T_{max} (eV)
1A	$\{\nu_i^{(A)}, k_i^{(A)}, \varphi_i^{(A)}\}_{i=1}^{10}$	0 - 1	14	1.5×10^1
2A		0.5 - 1.5	29	6.4×10^1
3A		1 - 2	51	2.0×10^2
4A		1.5 - 2.5	80	4.9×10^2
5A		2 - 2.5	83	5.3×10^2
6A		3 - 3.5	133	1.4×10^3
1B	$\{\nu_i^{(B)}, k_i^{(B)}, \varphi_i^{(B)}\}_{i=1}^{10}$	0 - 1	4	1.2×10^0
2B		0.5 - 1.5	5	1.9×10^0
3B		1 - 2	6	2.8×10^0
4B		1.5 - 2.5	60	2.8×10^2
5B		2 - 2.5	84	5.4×10^2
6B		3 - 3.5	108	8.9×10^2

APPENDIX I
TABLES AND FIGURES (CONT'D)

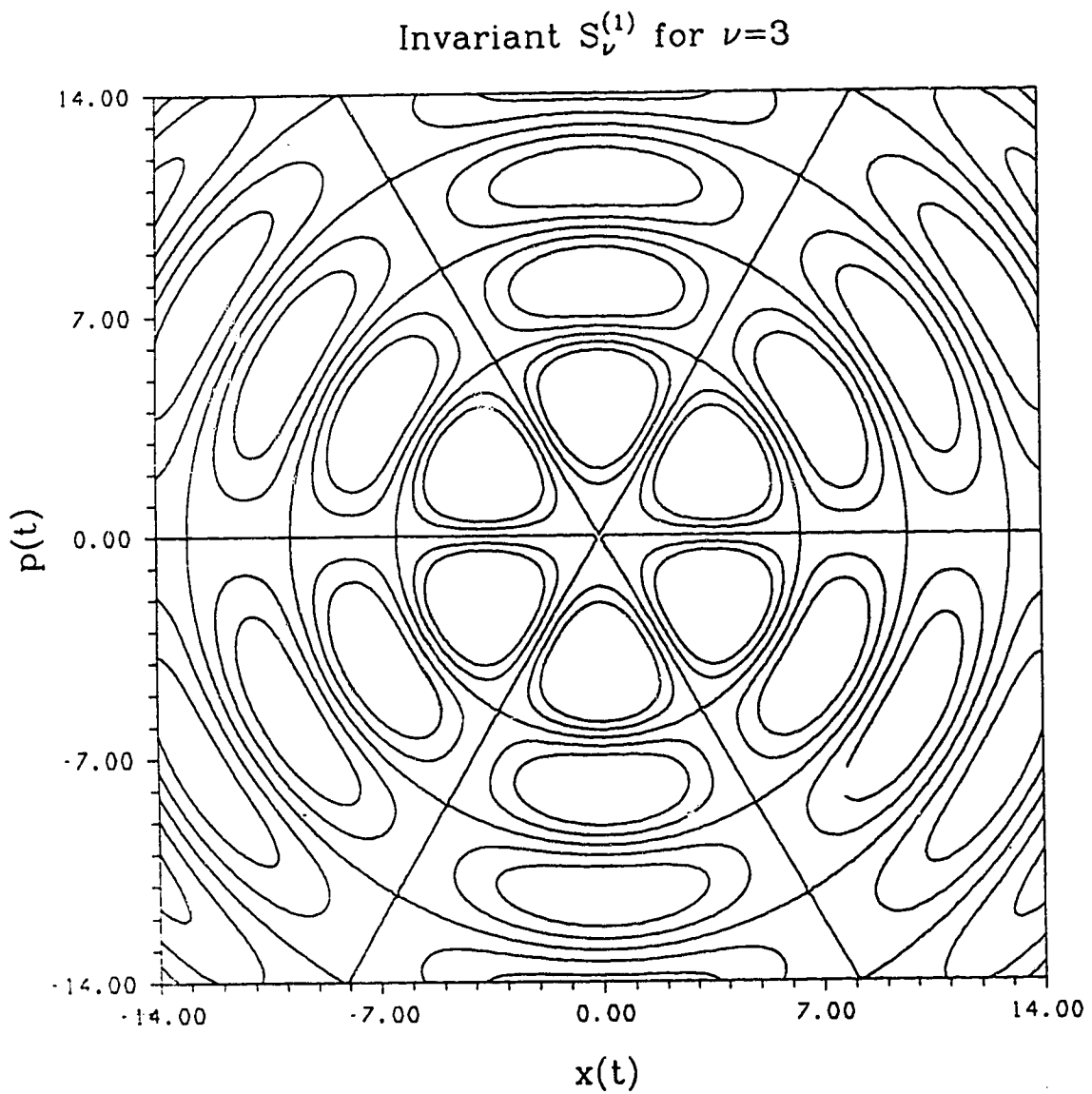


Figure I.1: Contour map of the invariant function $S_\nu^{(1)}$ for $\nu = 3$. The zeroes of this function correspond to the separatrix of the Hamiltonian (4.19).

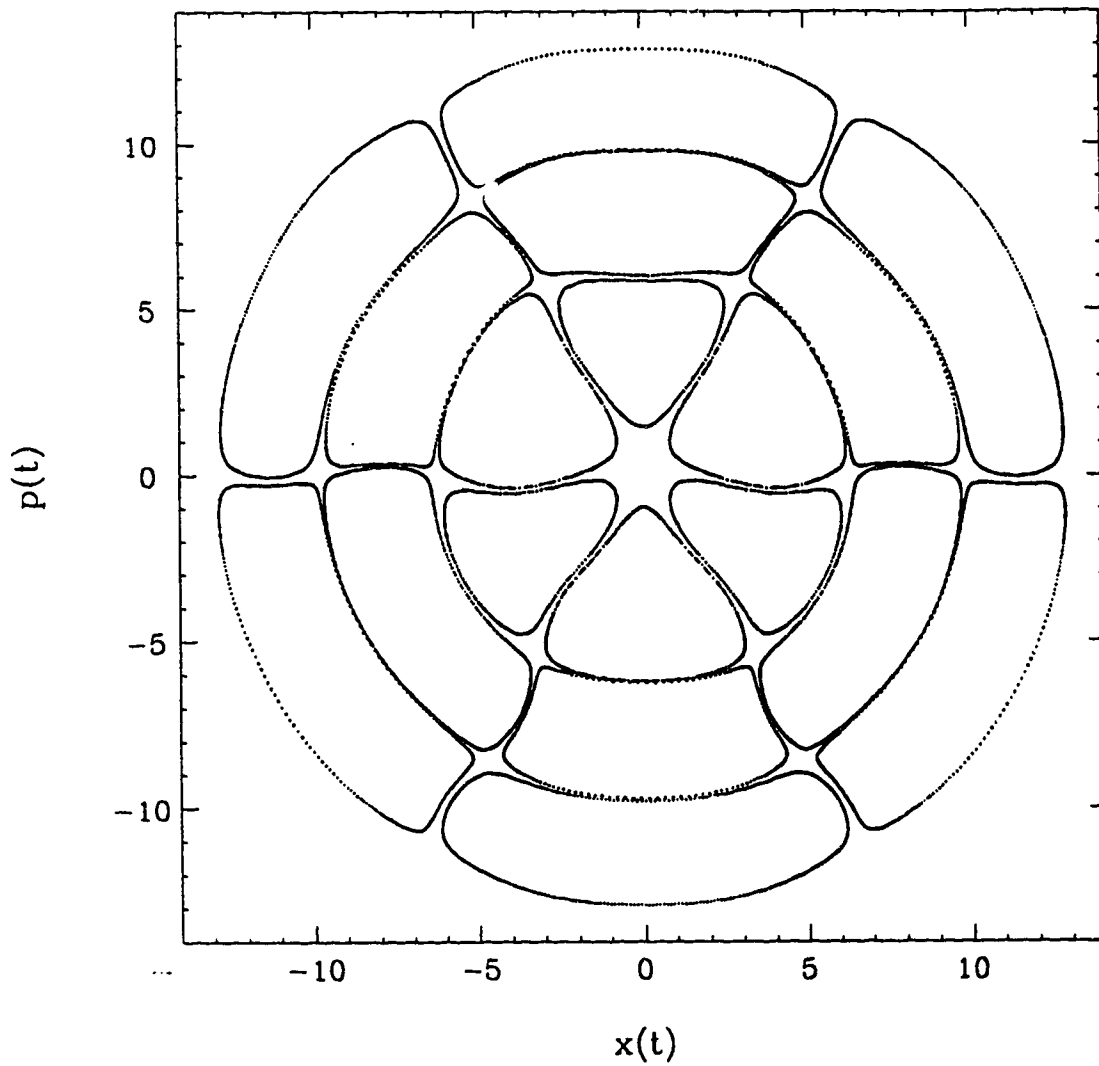
Surface of Section ($\nu=3, \epsilon=0.6$)

Figure I.2: Surface of section plot of the Hamiltonian (4.1) for 6 different initial conditions. The wave frequency is $\nu = 3$ and the perturbation strength is $\epsilon = 0.6$.

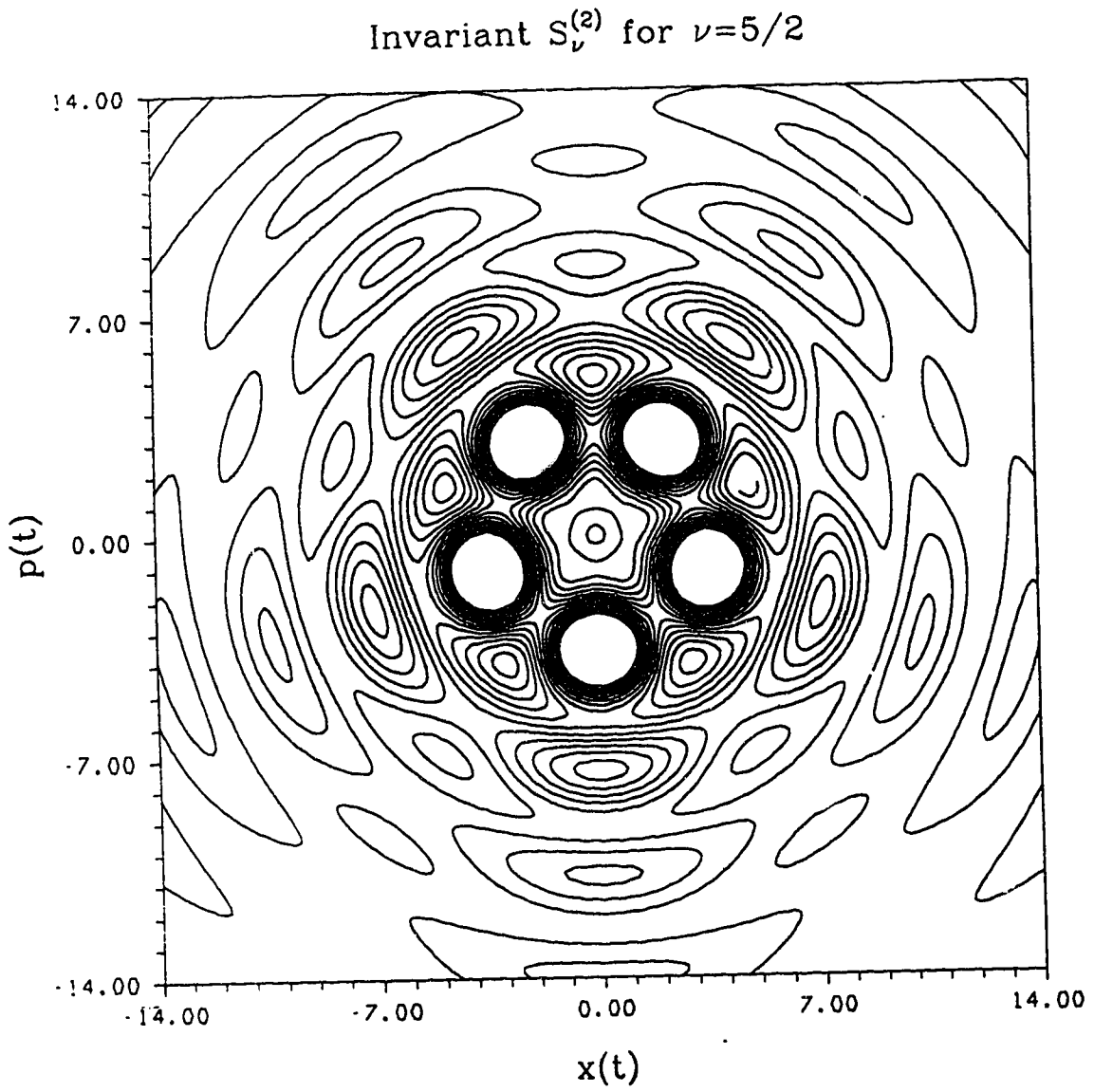


Figure I.3: Contour map of the invariant function $S_\nu^{(2)}$ for $\nu = 5/2$.

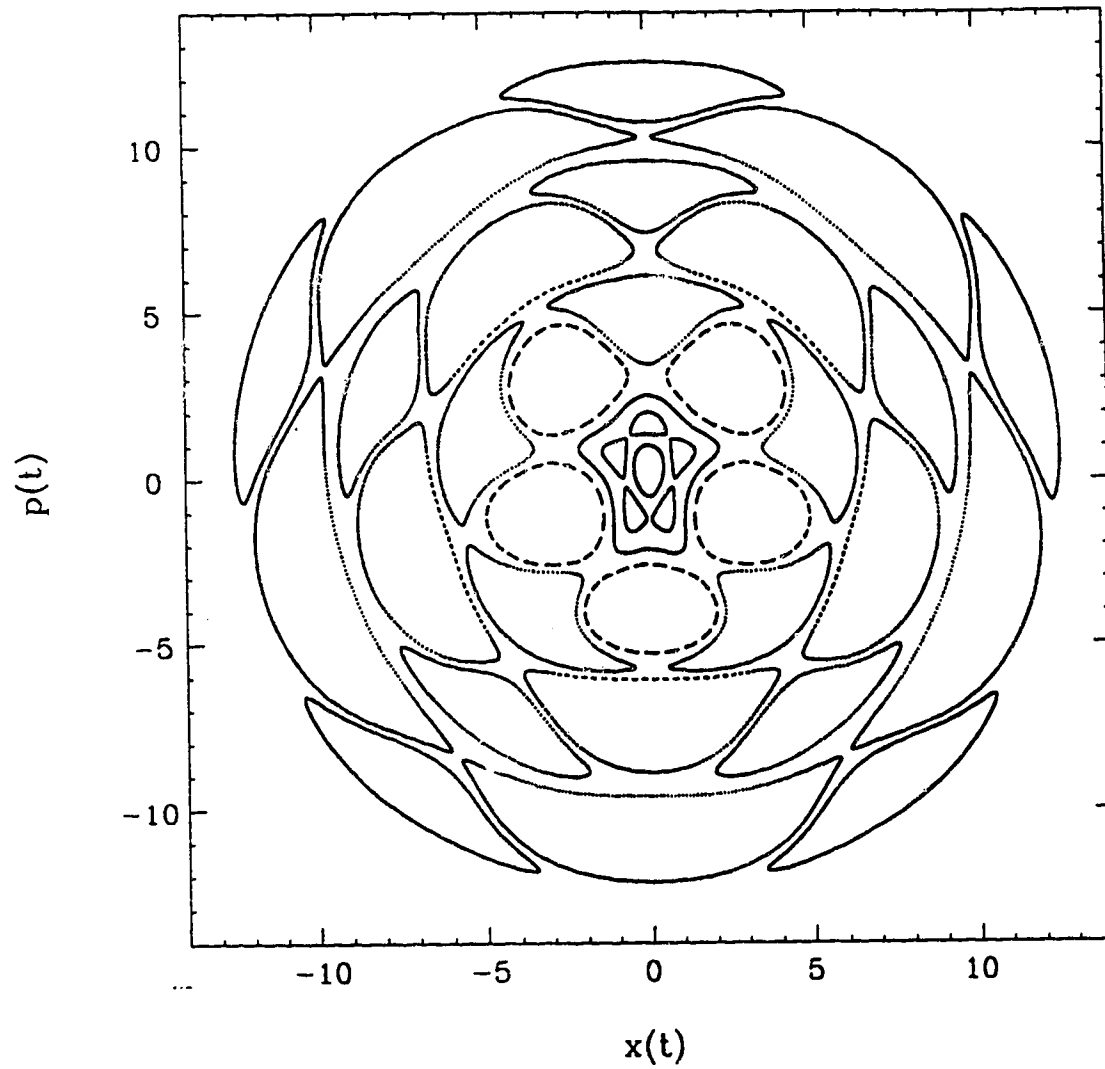
Surface of Section ($\nu=5/2$, $\epsilon=0.6$)

Figure I.4: Surface of section plot of the Hamiltonian (4.1) for 9 different initial conditions. The wave frequency is $\nu = 5/2$ and the perturbation strength is $\epsilon = 0.6$.

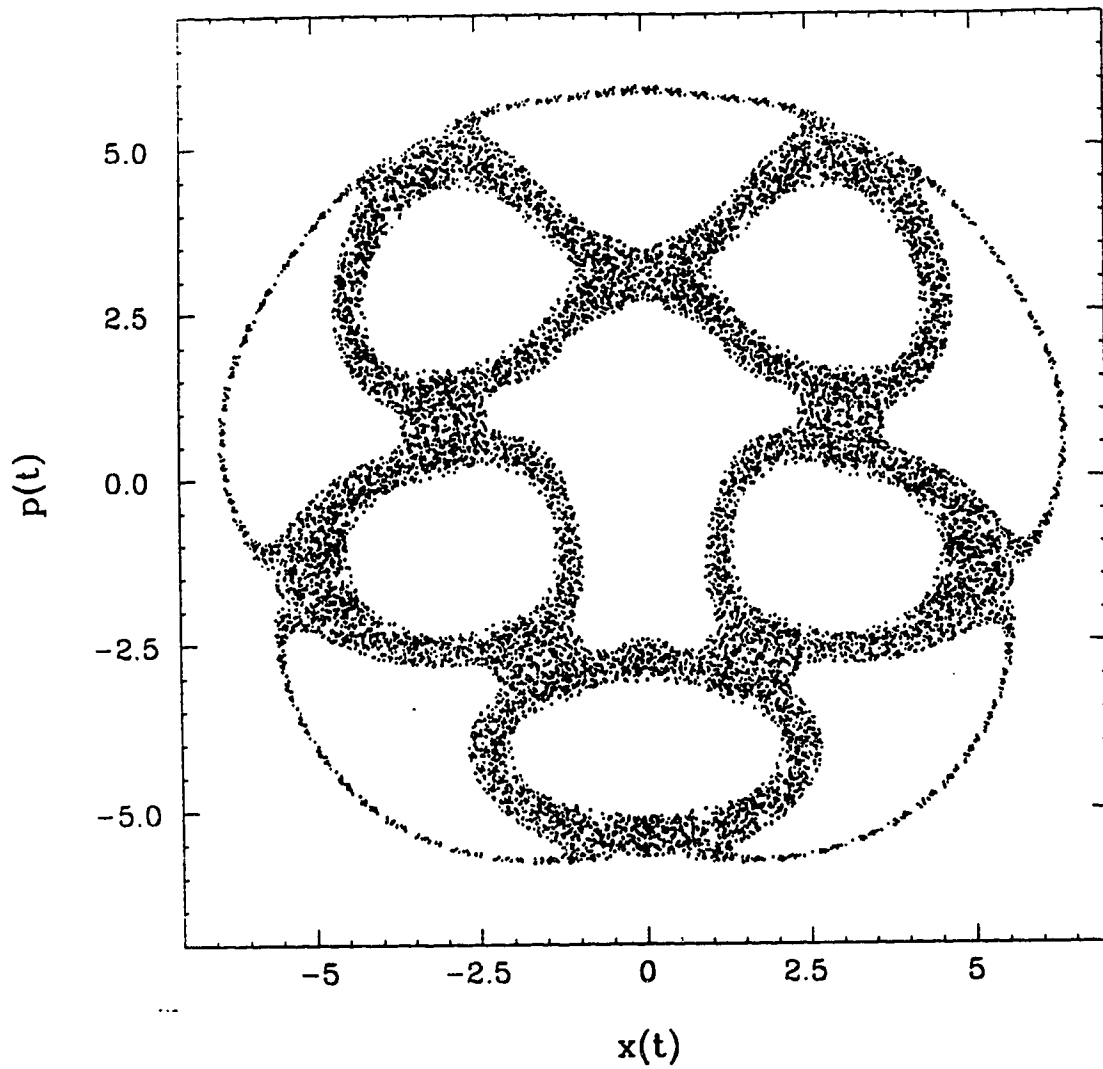
Surface of Section ($\nu=5/2$, $\epsilon=0.9$)

Figure I.5: Surface of section plot of the Hamiltonian (4.1) for 1 initial condition. The wave frequency is $\nu = 5/2$ and the perturbation strength is $\epsilon = 0.9$. Note the smaller plot dimensions as compared with Figure

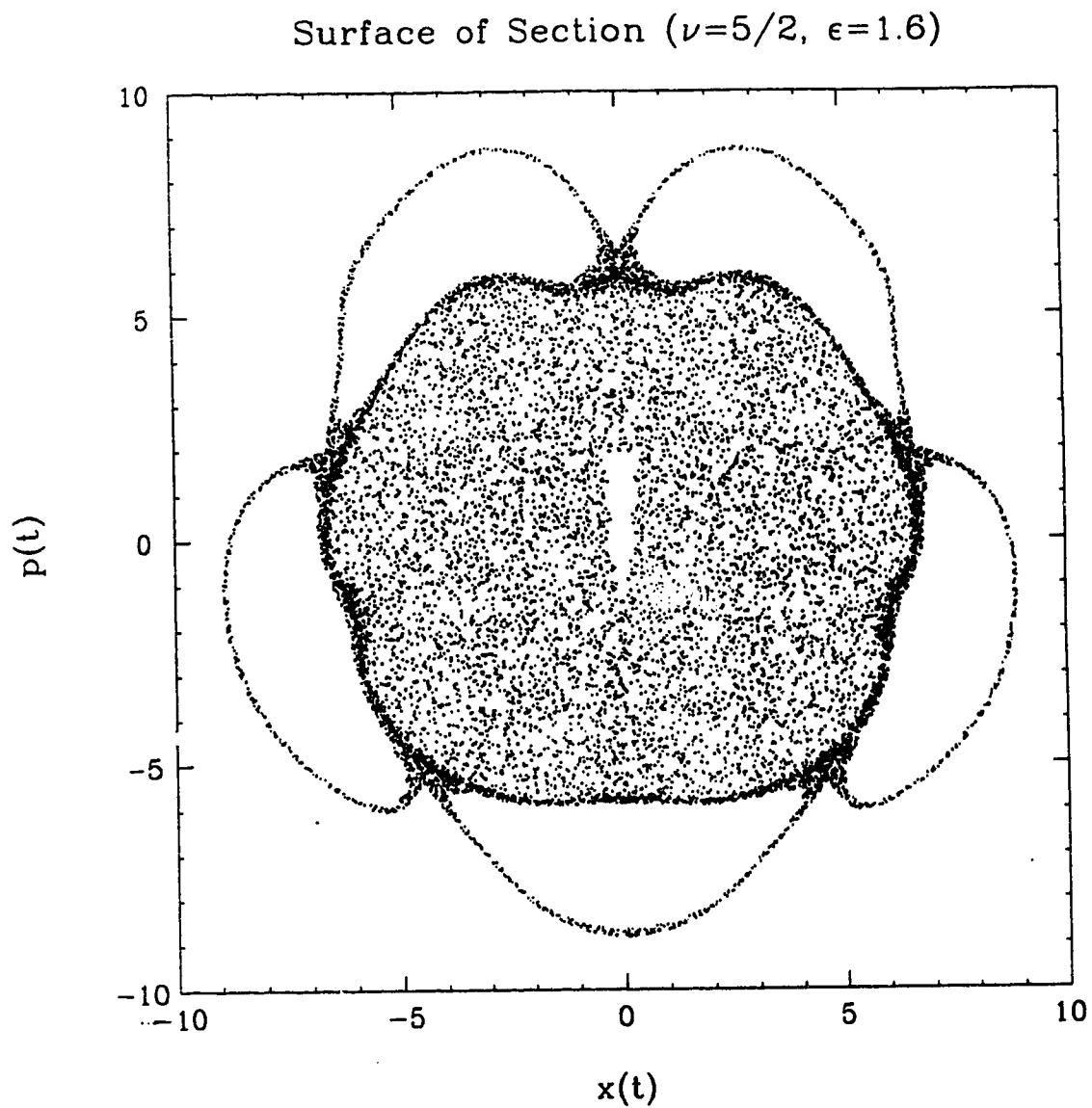


Figure I.6: Same as Figure I.5, except $\epsilon = 1.6$.

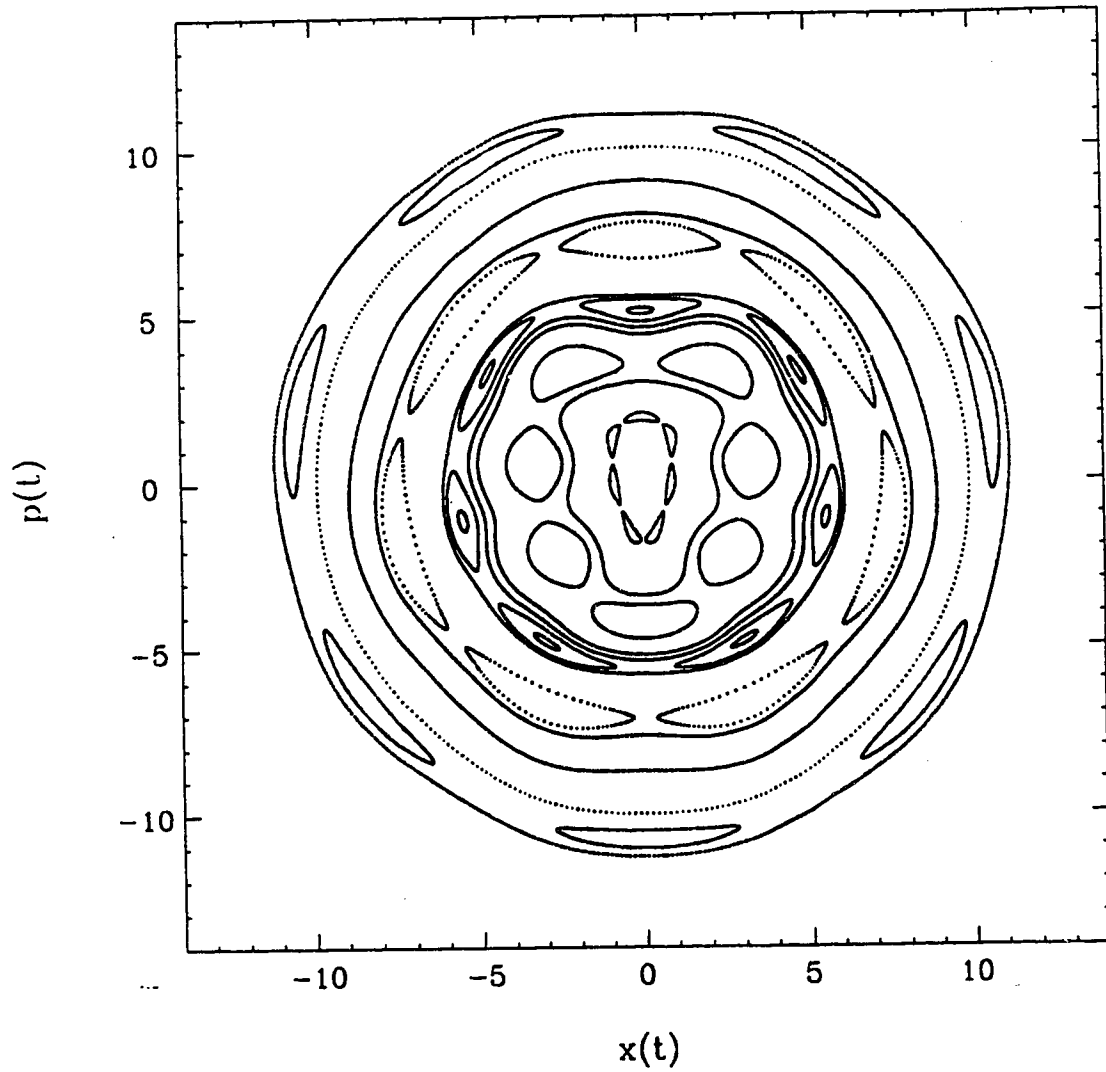
Surface of Section ($\nu=7/3$, $\epsilon=0.6$)

Figure I.7: Surface of section plot of the Hamiltonian (4.1) for 14 different initial conditions. The wave frequency is $\nu = 7/3$ and the perturbation strength is $\epsilon = 0.6$.

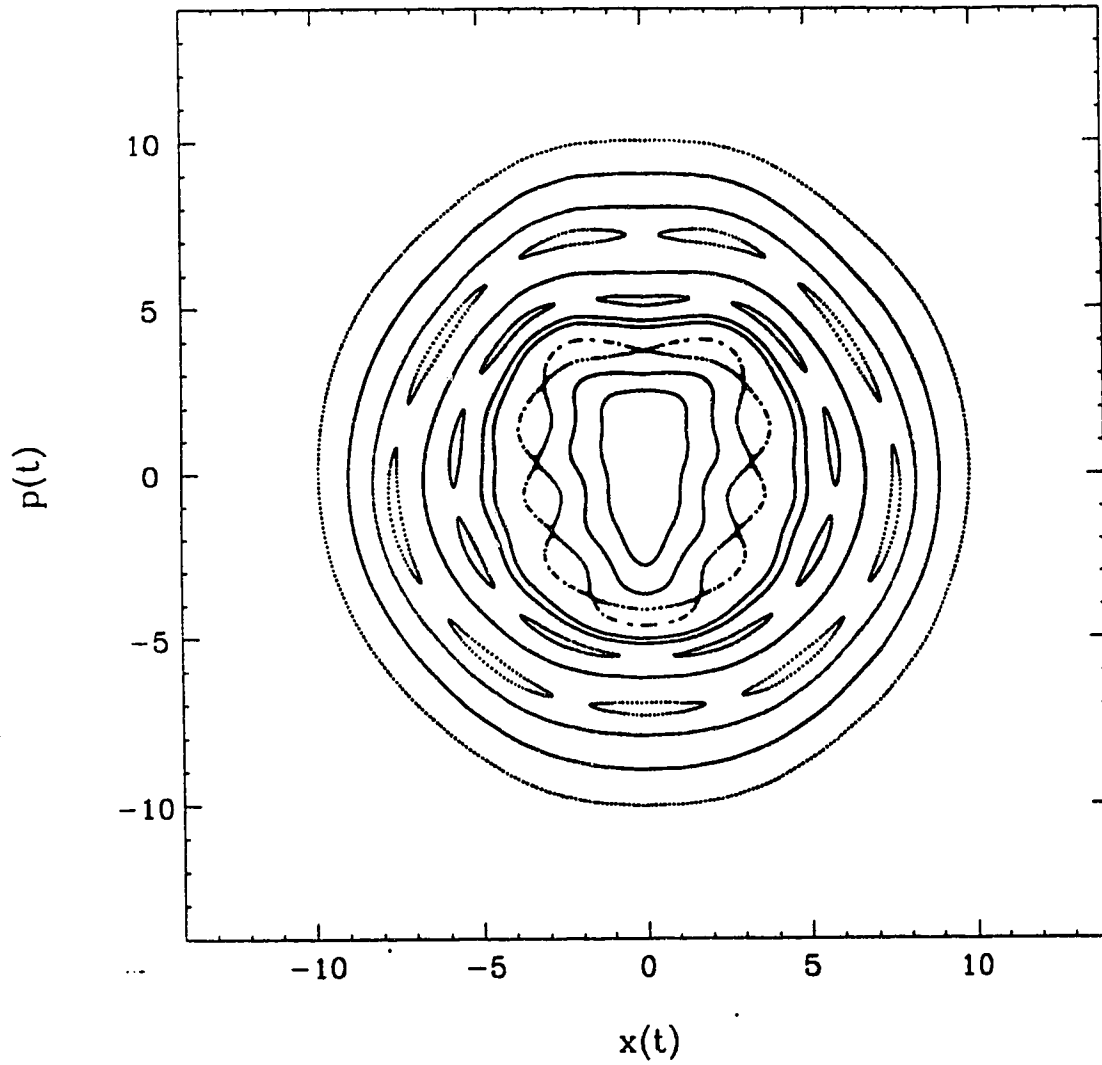
Surface of Section ($\nu=9/4$, $\epsilon=0.6$)

Figure I.8: Surface of section plot of the Hamiltonian (4.1) for 11 different initial conditions. The wave frequency is $\nu = 9/4$ and the perturbation strength is $\epsilon = 0.6$.